Doctor of Philosophy

액체로 처리된 고체 스폰지 및 금속 접점 에서 직접 전하 이동을 기반으로 하는 자체 전원 마찰 전기 센서

SELF-POWERED TRIBOELECTRIC SENSOR BASED ON DIRECT CHARGE TRANSFER BETWEEN LIQUID-TREATED SOLID FOAM AND METAL CONTACTS

QUANG TAN NGUYEN

The Graduate School

of the University of Ulsan

Department of Mechanical and Automotive Engineering

SELF-POWERED TRIBOELECTRIC SENSOR BASED ON DIRECT CHARGE TRANSFER BETWEEN LIQUID-TREATED SOLID FOAM AND METAL CONTACTS

Supervisor: Professor KYOUNG KWAN AHN

A Dissertation

Submitted to

the Graduate School of the University of Ulsan

In Partial Fulfillment of the Requirements

for the Degree of

Doctor of Philosophy

by

QUANG TAN NGUYEN

Department of Mechanical and Automotive Engineering

University of Ulsan, Korea

December 2023

액체로 처리된 고체 스폰지 및 금속 접점 에서 직접

전하 이동을 기반으로 하는 자체 전원 마찰 전기 센서
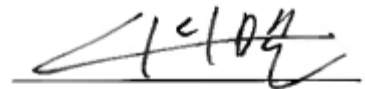
지고교수   **안경관**

이논문을 공학박사 학위 논문으로 제출함

2023 년 12 월

울산대학교 대학원

기계공학부

SELF-POWERED TRIBOELECTRIC SENSOR BASED ON DIRECT CHARGE TRANSFER BETWEEN LIQUID-TREATED SOLID FOAM AND METAL CONTACTS

This certifies that the dissertation

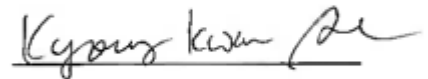**of QUANG TAN NGUYEN is approved by**

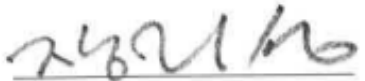Committee Chairman: Prof. DOO MAN CHUN
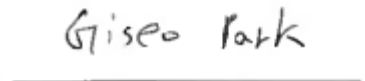
Committee Member: Prof. BYUNG RYONG LEE

Committee Member: Prof. KYOUNG KWAN AHN

Committee Member: Prof. JI SUNG JANG

Committee Member: Assistant Prof. GI SEO PARK

The Graduate School of the University of Ulsan

Department of Mechanical and Automotive Engineering

December 2023

Abstract

In recent years, there has been a growing demand for self-powered sensors that can work independently, without external power sources, particularly in situations where conventional power options like batteries aren't feasible. Since 2012, the triboelectric nanogenerator (TENG) has shown promise in harvesting mechanical energy and sensing. However, traditional TENGs produce alternating current, so a conversion to direct current (DC) is necessary for powering electronic devices that need DC power. This thesis introduces a new method for straightforward converting mechanical energy into DC power. It involves a simple setup with two metal contacts that gather DC power created when a liquid-treated solid foam made of water and cellulose (referred to as the "active layer") is slid. The energy conversion relies on the combination of the triboelectric effect and direct charge transfer between the metal contacts, which is different from traditional TENGs. The active layer plays an important role in effectively separating and transferring the charge generated by friction energy through an internal conductive path formed by a hydrogen-bonded network of water molecules. C-TEG generates a current density of $0.75\ A/m^2$ and a voltage of around 0.5 V with DC characteristics. It also exhibits high accuracy in measuring the ion concentration in aqueous solutions. This technology has led to the development of the cellulose-based triboelectric self-powered multifunctional sensor (C-TSMS), which combines energy harvesting and sensing capabilities into a unified device. C-TSMS shows excellent linearity and precision in responding to various stimuli like pressures, sliding velocities, water absorption, and ion concentrations ($R^2 > 0.99$). For self-powered operation, the voltage output can be further boosted by connecting multiple C-TSMSs and then successfully used to directly power functional electronics. Furthermore, a new structural design improves C-TEG's performance by changing the electrode configuration, shifting from a freestanding mode to a lateral sliding mode. This modification results in a remarkable current density of $3.57\ A/m^2$ and effective electric power harvesting (up to $0.174\ W/m^2$). In summary, these findings highlight the potential of this approach for capturing low-frequency mechanical energy from the environment across a range of applications, especially in the realm of self-powered sensors.

Keywords: *triboelectric nanogenerator, mechanical-to-electrical energy conversion, self-powered sensor, triboelectric effect, direct charge transfer, material work function, cellulose-treated foam, hydrogen-bonded network*

Acknowledgments

Contents

List of Figures

vii

List of Tables

List of Abbreviations

TENG	Triboelectric nanogenerator
FluTENG	Fluid-based triboelectric nanogenerator
TEG	Triboelectri generator
C-TEG	Cellulose-based triboelectric generator
C-TSMS	Cellulose-based triboelectric self-powered multifunctional sensor
LS-TENG	Liquid-solid triboelectric nanogenerator
LL-TENG	Liquid-liquid triboelectric nanogenerator
SS-TENG	Solid-solid triboelectric nanogenerator
EC	Electrochemical cell
CE	Contact electrification
AC	Alternating current
DC	Direct current
TECD	Triboelectric charge density
EDL	Electric double layer
EDAEC	Edge approximation-based equivalent capacitance
PVDF	Polyvinylidene fluoride
PDMS	Polydimethylsiloxane
PTFE	Polytetrafluoroethylene
ITO	Indium tin oxide
NaOH	Sodium hydroxide
NaCl	Sodium chloride
CNT	Carbon nanotube

WTCF	Water-treated cellulose foam
SLITF	Solid-liquid interface-treated foam
FE-SEM	Field emission scanning electron microscope
AFM	Atomic force microscopy
FT-IR	Fourier transform infrared
XRD	X-ray diffractometer
LED	Light-emitting diode
IDE	Interdigital electrode
CA	Contact angle
P	Power
Ws	Stored energy in a capacitor
a	Contact area
Isc	Short-circuit current
Jsc	Current density
Voc	Open-circuit voltage
Vbi	Built-in voltage
Ebi	Built-in electric field
ϕ	Material work function
e	Unit charge
μ	Material mobility
EF	Fermi level
Qsc	Transferred charge
$Qtri$	Triboelectric charge
RL (or R)	Load resistance

ΔR	Change in the internal resistance
$R0$	Internal resistance measured at the reference point
Ri (or Rw)	Internal resistance
CL	Load capacitance
$Cmax$	Maximum capacitance
σ	Dielectric surface
w	Width of the dielectric layer
L	Length of the dielectric layer
vt	Velocity with time
h	Height
θ	Angle
g	Gravity
ρ	Density of mass
D	Diameter
d	Distance
R^2	Coefficient of determination
S	Sensitivity
Ff	Friction force
Cf	Coefficient of friction
FA	Applied force

INTRODUCTION

A. Motivation

With the rapidly increasing consumption of traditional fossil energy, the development of alternative renewable energies and related energy harvesting technologies has become one of the most important topics for human attention. Modern energy sources are characterized by their eco-friendliness, safety, reliability, and cost-effectiveness. Among these sources, mechanical energies harnessed from wind, water flow, and ocean waves stand out as versatile options for power generation, significantly bolstering the global energy demand.

Moreover, the advent of the Internet of Things has ushered in a new area of electronics that prioritizes compactness, portability, and functionality. Simultaneously, these devices require portable, uninterrupted, and stable power sources for charging. Given their minimal power requirements, typically ranging from microwatts to milliwatts, energy harvesting techniques become a feasible solution [1-3]. Even small mechanical energy sources, such as human motions, low-frequency vibration, and raindrops, hold the potential for converting into electrical power, although they have often been overlooked due to their seemly limited input energy [4].

Concurrently, as the Earth's surface is predominantly covered 70% by ocean water, ambient humidity is omnipresent in the atmosphere, presenting an opportunity for sustained energy harvesting. Water-based energy harvesting technologies have garnered significant research interest, primarily due to their environmental friendliness and the widespread availability of water [5-7]. Therefore, the development of devices capable of converting mechanical energy into electricity in high-humidity environments has become a focus of scientific inquiry.

In the realm of energy harvesting technologies, the triboelectric nanogenerator (TENG), initially proposed by Zhong Lin Wang and colleagues [8-10], has emerged as a highly efficient strategy, opening doors to harness a multitude of small energy sources. TENG operates on the principle of the triboelectric effect, which occurs when two different materials come into physical contact, leading to the transfer of electrons from one material to the other.

Up to now, several research groups have successfully devised TENGs for energy harvesting, with applications spanning vibration and fluid flow [11-17]. Numerous designs of fluid-based

triboelectric nanogenerators (FluTENG) have been developed based on different contact electrification mechanisms, including solid-solid [18-47], liquid-solid [11, 13, 48-79], and liquid-liquid [80] interactions. Many research groups have integrated TENG devices into energy harvesting applications [22, 23, 36, 81-85] and self-powered devices [26, 86-88].

A specific subfield of TENG worth noting is the water-based TENG (W-TENG), which gained significant traction for energy harvesting and powering self-sustained sensors, as shown in **Figure 1** [86, 89-93]. W-TENG has demonstrated its efficacy in capturing energy from tidal and oceanic waves, rainfall, and water streams, thereby promising substantial potential. Notably, W-TENG-based gadgets have been successfully employed in the development of self-powered sensors due to their ability to convert mechanical energy into electric output without the need for external power sources. A range of self-powered sensors based on W-TENG, including active pressure/touch sensors,[92] chemical sensors [94], biological sensors [95], and gas sensors [96, 97], are developed as robust applications for TENG devices.
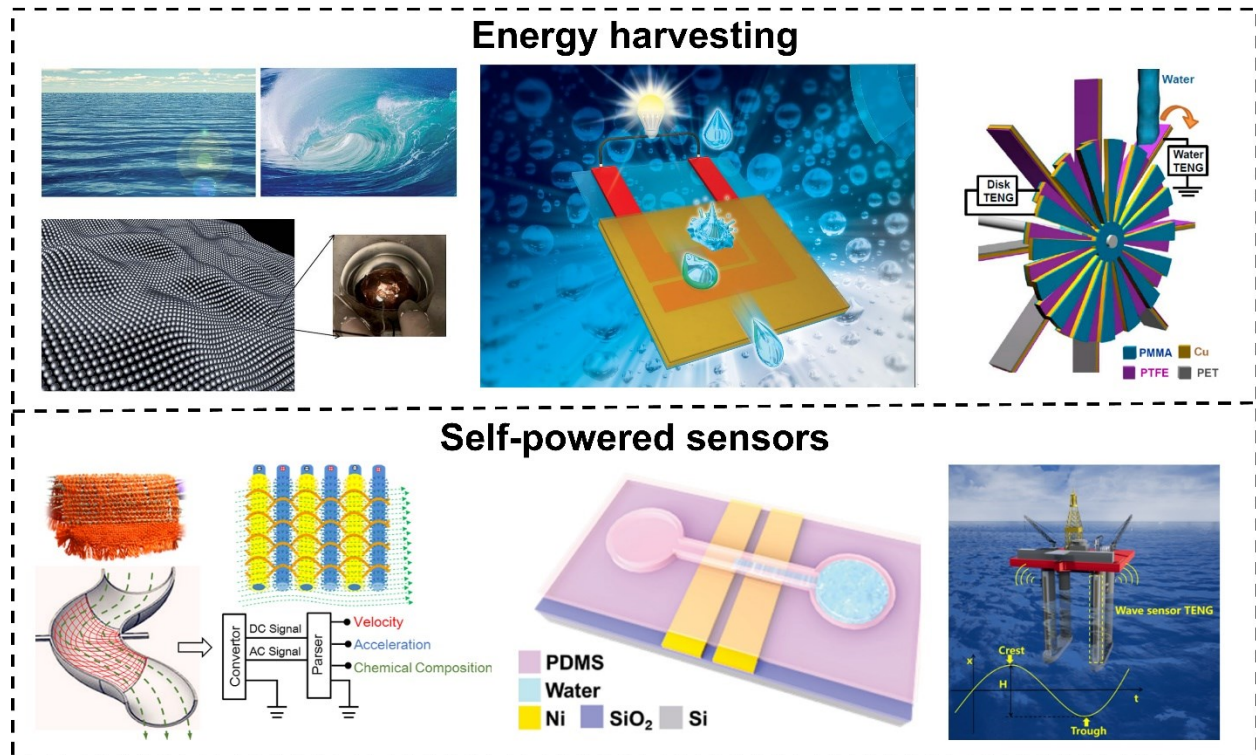
Figure 1: Application of water-based TENG in energy harvesting and self-powered sensors.

Traditional FluTENGs operate by harnessing the effects of triboelectrification and electrostatic induction. When two materials make contact or slide against each other, they accumulate charges with opposing signs on their respective contact surfaces. Consequently, most existing TENGs yield alternating current (AC) output characteristics due to these processes. However, this poses challenges when directly powering electronic devices that require direct-current (DC) power. To address this issue, the rectification method is mandatory to convert the output to DC power, as shown in **Figure 2**.

To overcome these limitations, innovative strategies and technologies have emerged, offering the promise of converting mechanical energy directly into DC electric energy. This advancement presents an effective solution to the challenges mentioned [98-109]. Furthermore, meeting the power requirements for various practical applications is crucial. Therefore, enhancing the output power density, particularly the output current, has garnered considerable attention in the investigation of DC energy harvesters.
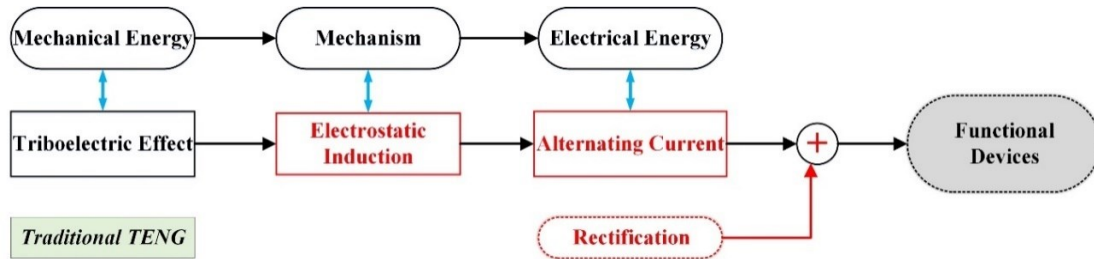
Figure 2: Schematic flowchart of the methodology of the traditional TENGs

In spite of the progress in sensor technology, conventional sensors are constrained by their single-sensing capabilities. Addressing this limitation necessitates the fusion of diverse sensing mechanisms and the use of complex structures and manufacturing methods to attain multifunctional sensing capacities [110]. Hence, there's a pressing need to develop a sustainable multifunctional sensor capable of detecting and differentiating between multiple parameters while maintaining simplicity in manufacturing.

Beyond the imperative of multifunctionality, the power supply emerges as another critical consideration. Conventional sensors rely on batteries, which imposes limitations on their flexibility [1]. This underscores the requirement for sensor systems based on energy harvesting, enabling operation without external power sources. In such energy harvesting-based sensor systems, the

energy necessary for processing is supplied by the energy harvesting unit, while the sensor module collects the sensing signal, as shown in **Figure 3**.

From this analysis, it'e evident that there is a demand for innovative energy harvesting techniques capable of converting mechanical energy into DC power, as well as effective sensing technologies exhibiting high sensitivity and accuracy.
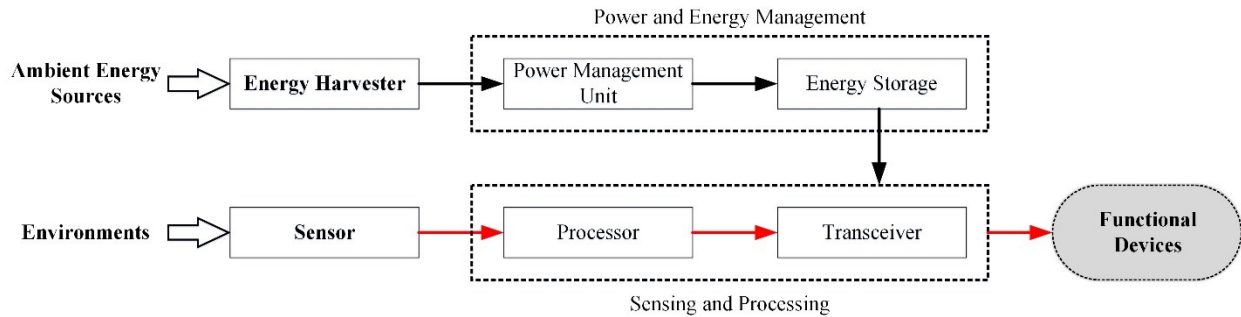
Figure 3: Schematic flowchart of the methodology of the traditional energy harvesting-based sensor

B. Aims of this research

The objective of this research is to create a direct-current triboelectric generator (DC-TEG), using a liquid-treated solid foam and two metal contacts as active materials. **Figure 4** outlines the process for harvesting mechanical energy in an innovative manner, which combines the triboelectric effect with direct charge transfer between two metal contacts having different work functions. This approach distinguishes itself from traditional electrostatic induction employed in conventional TENGs.

To elaborate, the mechanical energy is initially transformed into electrostatic energy through the triboelectric effect, leading to the generation of triboelectric charges from friction energy. These charges are subsequently separated due to the built-in electric field between the metal contacts, which also serve as the system's electrodes. Consequently, these generated charges move between the two electrodes via a conductive path formed by a hydrogen-bonded network of water molecules within the cellulose foam in a specific direction. This results in a unidirectional flow of electrons through the external circuit, ultimately producing DC power. Unlike the indirect charge transfer of the electrostatic induction process, in this method, the charge generated by the

4

triboelectric effect is directly transferred between electrodes throughout the entire circuit, yielding DC output instead of AC output as in traditional TENGs.

This study primarily focuses on advancing energy harvesting technology, with the core objective of directly converting mechanical energy into DC power. In addition, the research aims to experimentally evaluate the key parameters to optimize the power generation performance and then demonstrate its potential for powering functional electronic devices. Furthermore, the research endeavors to address various challenges of TENGs, including low current density in traditional TENGs, high energy loss due to rectification, complexity in material fabrication and system manufacturing, limited cost-efficiency, and restrictions in tailoring design for specific applications. Notably, a novel structural design has been developed to enhance output performance and improve the environmental suitability of this proposed methodology in the field of energy harvesting and self-powered sensing systems.
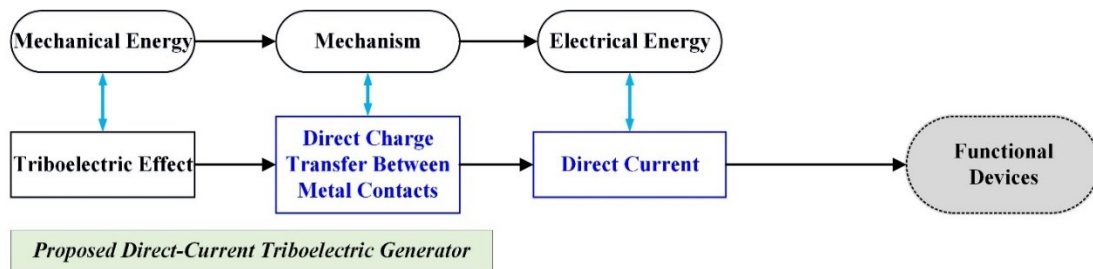
Figure 4: Schematic flowchart of the methodology of the proposed direct-current triboelectric generator

Importantly, in response to the challenges within sensing technology, this research also strives to explore and illustrate the concept of self-powered sensing technology, a viable solution that has garnered notable interest from the scientific community. A self-powered sensing system consists of two key components: an active sensor and an energy-harvesting unit, as illustrated in **Figure 5**. The system relies on the electrical signals it generates as input information for its sensing and processing functions.

By monitoring the output signals, a wealth of information related to various environmental factors, including physical, chemical, and biological stimuli, can be effectively tracked. Simultaneously, the energy harvester not only supplies the necessary energy for the sensing and

processing functions but also serves as the source of information for detecting environmental stimuli. This approach is particularly well-suited for small electronic devices that from the environment is used to power the sensor, so it doesn't need external power. Thereby, the energy harvester not only provides energy to run the sensing and processing steps but also information as the sensing signal for detecting environmental stimuli. This approach is well-suited for small electronics that operate at low power levels, typically ranging from microwatts to milliwatts, and exhibits substantial potential for the development of multifunctional sensing systems.
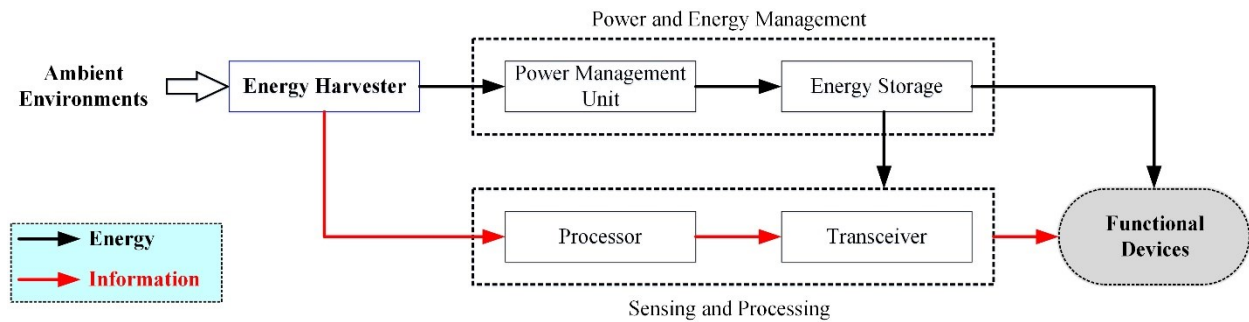
Figure 5: Schematic flowchart of the methodology of the self-powered sensing system

C. Thesis overview

This thesis is structured into several sections, each addressing specific aspects of the research as follows:

Chapter I: This section delves into the contemporary developments of fluid-based TENG devices. These devices, tapping into the power of water and wind, have sparked significant interest among global researchers as promising power sources. The chapter examines ongoing efforts to optimize these devices, with a particular emphasis on harnessing mechanical energy through the triboelectric effect at the contact interface. It presents an analysis of various optimization techniques, discussing their advantages and limitations. Furthermore, the chapter explores the factors affecting FluTENG efficiency and details mechanisms employed in FluTENG, considering practical applications. It also provides a comprehensive review of self-powered sensors that leverage FluTENG technology, providing insight into the current progress of physical, chemical, and environmental sensors utilizing FluTENG technology, along with an exploration of existing limitations and potential solutions to overcome challenges.

Chapter II: This section introduces a novel methodology to convert mechanical energy into DC power. This innovative technique combines the principles of the triboelectric effect and the direct charge transfer occurring between two metals with different work functions. This approach departs from the traditional electrostatic induction used in conventional TENGs. By changing the charge separation and flow processes, this technology directly generates DC power. The chapter further discusses the testing platform created to examine the charge transfer mechanism between materials and effectively harness the generated energy. Experiments are conducted to assess the impact of various factors influencing the charge generation process, such as the selection of triboelectric materials and their respective work functions.

Chapter III: This section explores the potential applications of this innovative technology in self-powered multifunctional sensing systems. Beyond its DC power generation capabilities, this method can monitor various physical and chemical stimuli with exceptional sensitivity and accuracy, which influence material mobility and friction energy. The chapter highlights the potential for developing self-powered multifunctional sensing systems rooted in this technology.

Chapter IV: This section presents an advanced design focused on enhancing output performance. Departing from the freestanding mode mentioned in earlier chapters, this innovative device adopts a lateral sliding approach. Notably, it achieves a remarkable maximum current density, surpassing amperes per meter squared. This demonstrates substantial potential for supplying ample energy for a broad range of electronic applications.

Chapter V: This concluding section offers a summary of the research conducted and outlines potential avenues for future research and improvement.

CHAPTER I – FLUID-BASED TRIBOELECTRIC NANOGENERATORS: LITERATURE REVIEW

In recent decades, various mechanical energy sources, such as electromagnetic and piezoelectric methods, have been employed for electricity generation. Fluid flow energy, derived from water and air, stands out as a significant renewable energy source found in rain, streams, ocean waves, and wind. The triboelectric nanogenerator (TENG), introduced in 2012 by Zhong Lin Wang's research group, has emerged as a crucial innovation for energy harvesting. This chapter presents a literature review of fluid-based TENG (Flu-TENG), encompassing water-based and air-based systems. It explores fundamental principles, operational modes, current designs, applications, diverse structures, potential for power generation, and self-powered sensing systems. Flu-TENG shows promise for large-scale applications and hybrid use with other energy harvesting technologies. The chapter discusses challenges, suggests efficiency enhancements, and provides insights into future trends in FluTENG development.

1. Introduction

Nowadays, excessive fossil fuel consumption leads to a rapid depletion of their reserves has a significant adverse impact on the environment, and becomes one of the biggest challenges the world faces [111]. Therefore, searching for clean and renewable energy is necessary for sustainable development. As one of the most important renewable energy sources, ambient mechanical energy from the environment, including vibrations, walking, human motions, raindrops, flowing water, ocean waves, and wind [112], can be used to produce electricity via energy harvesting technologies such as piezoelectricity [113, 114], electromagnetic [115, 116]. The electrostatic charge that is generated when two materials are contacted or rubbed and then separated is a well-known physical process that has been studied for over 2000 years and has attracted many research groups [117]. Since 2012, Z. L. Wang et al. have invented a new energy harvesting technology based on the coupling effects of contact electrification and electrostatic induction between two materials, namely a triboelectric nanogenerator (TENG) [118]. Many research groups have developed their TENG devices based on energy harvesting applications [22, 23, 36, 81-85] and self-powered devices [26, 86-88]. TENGs have been shown as sustainable technology in green energy harvesting.

On another hand, almost Earth's surface is covered by fluid, which is defined as water and air, and the energy from its movement can be harnessed as primary energy to produce electricity, which is one of the most important and widely used renewable energy sources [119]. This chapter focuses on fluid-based TENGs (Flu-TENG), which leverage the movement of water and air for energy production. Various Flu-TENG designs have been developed based on different contact electrification mechanisms, including solid-solid [18-47], liquid-solid [11, 13, 48-79], and liquid-liquid [80] interactions. The chapter provides an overview of fundamental theories, principles, and applications of Flu-TENGs, showcasing their ability to harvest energy from raindrops, streams, waves, and wind. Flu-TENG emerges as a promising candidate for large-scale energy harvesting and hybrid applications with other technologies. According to the recent development of TENG devices, Flu-TENG is a promising candidate for harvesting energy from large-scale applications and has a high potential to hybrid with other energy harvesting technologies, such as solar, electromagnetic, and piezoelectric technologies [11, 23, 26, 29, 36, 40, 55, 60, 114, 120].

Furthermore, Flu-TENGs have been successfully employed in self-powered sensors, transforming mechanical energy into electricity without an external power source. The chapter delves into recent developments in self-powered sensors based on Flu-TENG, covering applications such as pressure/force sensors [58, 74, 87], motion sensors [86, 87], velocity sensors [20, 25, 26, 35, 59, 121-123], temperature/humidity sensors [27, 76, 124], and chemical sensors [49, 53, 94, 125, 126], biological sensors [90], gases sensing [91, 92], and so on will be summarized as strong applications for FluTENG devices. The discussion includes strategies to enhance electricity generation and sensitivity, focusing on selection of materials [13, 26, 35, 78, 83, 84], the surface modification, particularly for hydrophobicity or liquid properties [13, 46, 50, 57, 61, 62, 79, 85, 86, 127], and the design structure [128-132]. The chapter concludes by offering insights into the future development and applications of Flu-TENG, emphasizing its potential for advancing sustainable energy solutions and sensing technologies.

2. Fundamental theories

2.1. Origin of contact-electrification

The triboelectric nanogenerator is a new energy-harvesting technology based on the coupling effects of contact electrification and electrostatic induction between two materials. To make a clear understanding of contact electrification, a study on the fundamentals of contact electrification

should be considered based on the different cases of contact surfaces, particularly for the interface between solids and liquids. The process is illustrated in **Figure 1.1a-(i)**, the contact electrification can be explained by using the surface state model [133, 134]. Two dielectric materials, A and B, with different electric structures, undergo contact electrification when physically pressed together. This results in the transfer of electrons from the surface of material A to material B. Upon separation, the transferred electrons remain, leading to a net positive charge on material A and a net negative charge on material B.

Besides, not only for solid-solid interfaces but contact-electrification occurs also at liquid-solid and liquid-liquid interfaces. However, the electric structure model could not represent the materials that do not have a well-characterized molecule's structure, such as wood, and hair. Therefore, a general model for understanding contact-electrification in different cases of materials' properties is needed. Z. L. Wang and A. C. Wang [134] proposed their general model that operates on atomic and molecule levels, as shown in **Figure 1.1a-(ii)**. Between two atoms, an equilibrium distance (a) can be established if a bond is formed. When an external force is applied, the interatomic distance x could be shorter or larger than the equilibrium distance a, resulting in generating a local repulsive force with the increased overlap of electron clouds or an attractive force with the reduced overlap of electron clouds, respectively. Based on the repulsive force between two atoms, electrons can transfer from one surface to the other, resulting in contact electrification. On the contrary, the bond between the two atoms could be broken. By using the general model at the atomic/molecule level, contact electrification between two liquids can be explained. If two liquids are immiscible, the molecules of one liquid come into contact with the surface of another liquid, the electrons will transfer from molecules to the other surface, and the liquid-liquid interfaces could be charged.

The contact-electrification between liquid and solid relates to the formation of the electric double layer (EDL) at the liquid-solid interfaces as the two-step process, as presented in **Figure 1.1b**. In the first step, electron cloud overlap occurs, leading to electron transfer and atom charging on the solid surface. External force from liquid flow can break the formed bond, leaving ions on the solid surface and free molecules/atoms in the liquid. In the second step, electrostatic interactions cause negative ions in the liquid to attract to the solid surface, forming the EDL. Contact electrification due to electron transfer in the first step is essential for EDL formation.
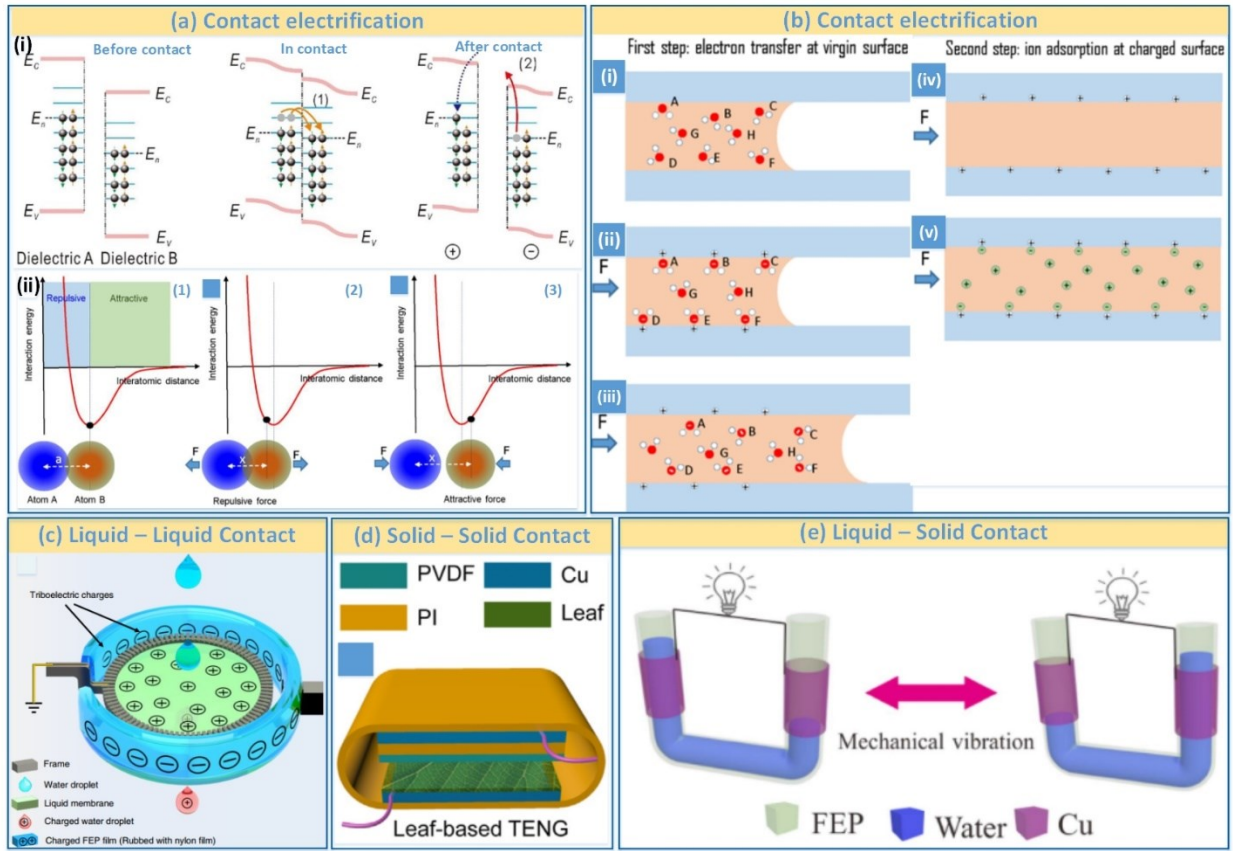
Figure 1.1: Schematic illustration of (a) Charge transfer before contact, in contact, and after contact between two different dielectric materials for a case that En of the former is higher than that of the latter and the band structure model holds (i); Interatomic interaction potential between two atoms and the force between the two when they are at the equilibrium position (1), with strong electron cloud/ wave-function overlap in the repulsive region (2), and with little electron cloud/wave-function overlap in the attractive region (3) (ii) [134]; (b) A proposed two-step model on the procedures for forming an electric double layer at a liquid-solid interface [134]; (c) liquid-liquid interfaces [80]. (d) solid-solid interfaces [32]; (e) liquid-solid interfaces contact electrification for fluid-based TENG [74].

For fluid-based triboelectric nanogenerators (TENGs), this contact-electrification theory has been applied in designs for harvesting energy from water and airflow. Air-based TENGs rely on solid-solid contact-electrification, while water-based TENGs utilize solid-solid, liquid-solid, and contact-electrification. Contact electrification at the liquid-liquid (L-L) interface in TENGs is an undeveloped area, except for a proposed L-L TENG by J. Nie et al., harnessing energy from raindrops (**Figure 1.1c**) [80]. In this design, a dynamic contact-separation process between a water droplet and a liquid membrane induces conduction current and generates electricity. On another hand, based on wind energy harvesting, a solid-solid TENG was reported by Y. Feng et al., as

illustrated in **Figure 1.1d** [32]. Friction between the leaf and PVDF layer generates charges, and electrostatic induction produces a potential difference, leading to electric current flow during continuous contact-separation. X. Zhang et al. proposed a design based on liquid-solid contact electrification, as presented in **Figure 1.1e** [74], involving water flow inside an FEP tube. Interaction between charged water and the tube generates an electric current through electrostatic induction on surrounding Cu electrodes.

2.2. Basic modes of operation

Since its invention in 2012, many TENG designs have been developed for harvesting various types of mechanical energy. According to the different moving manners of the triboelectric layer, and the different configurations of the electrodes, four basic modes of operations of TENG have been realized by many research groups, including contact-separation mode, lateral-sliding mode, freestanding mode, single-electrode mode, as shown in **Figure 1.2**. Based on these four modes of operation, the fluid-based triboelectric nanogenerators have been designed for harvesting energy from water flow and airflow.
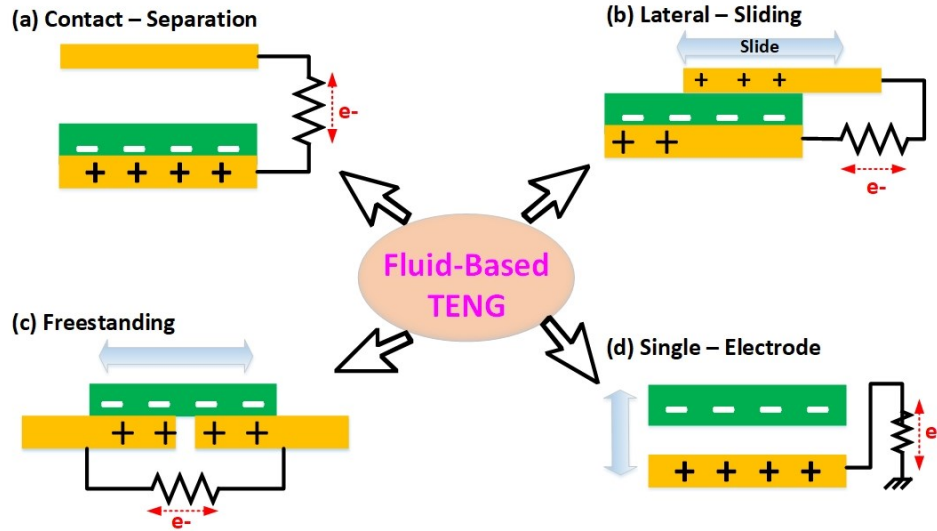
Figure 1.2: Basic modes of operation of fluid-based triboelectric nanogenerator: (a) contact-separation mode, (b) lateral-sliding mode, (c) freestanding mode, and (d) single-electrode mode.

2.2.1. Contact-separation mode

The configuration of the contact-separation mode TENG (CS-TENG) consists of two electrodes and is related to triboelectric layers. In this mode, electrical energy is produced through

electrical induction when a solid surface oscillates vertically, contacting and then separating from water [62, 73, 127, 135]. The external force causes two triboelectric layers to acquire opposite charges at their interfaces. Upon force release, separation creates a potential drop across electrodes, driving electron flow through a load. This process results in AC-type current as potential changes during contact and separation. As can be seen in **Figure 1.3a**, Lin et al. [135] reported a water-TENG based on this principle. They achieved a voltage of 52 V, and current and power densities of about 2.45 mA/m^2 and 0.13 W/m^2, respectively. Before contact, the polydimethylsiloxane (PDMS) surface remains uncharged. When external pressure causes the PDMS surface to contact water, CE occurs, establishing potential differences. Upon separation, transferred charges on PDMS break electrical neutrality, inducing positive and negative charges on electrodes, and generating current. The cycle repeats, providing continuous AC output.
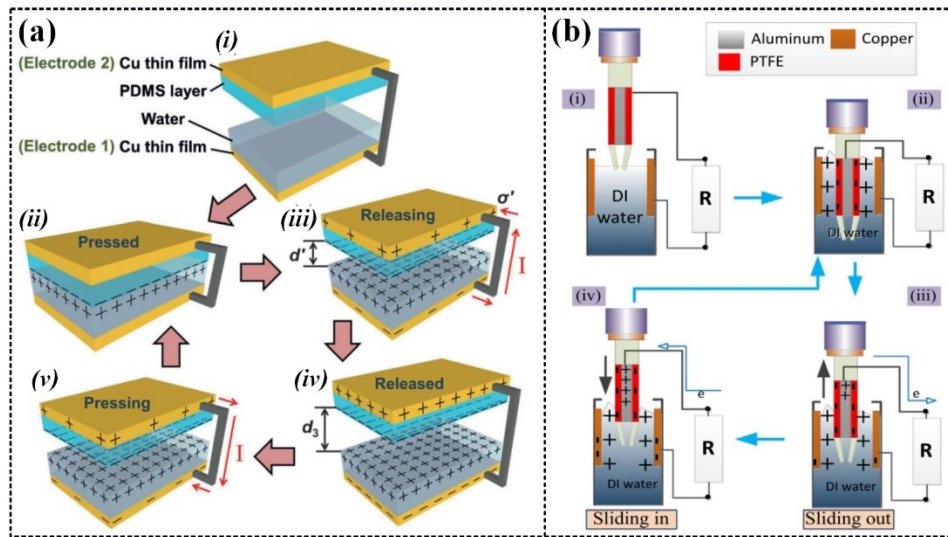
Figure 1.3: Schematic diagram and working mechanism of (a) contact-separation mode [135] and (b) Lateral-sliding mode [136].

2.2.2. Lateral-sliding mode

Lateral sliding mode is another power generation mode that utilizes the same structure as the contact separation mode but with a different manner of movement. Instead of relying on contact separation, it produces power through lateral movement between two contact surfaces, where relative friction plays a crucial role [52, 61, 136]. The working mechanism of a lateral sliding mode is illustrated in **Figure 1.3b**. Nahian et al. [136] proposed a lateral sliding-style fluid-based

triboelectric nanogenerator (L-S FluTENG), which consists of an aluminum tape covered by a PTFE layer and located on the outer surface of a tube, and a cylindrical reservoir with a Cu located on the inside surface. At first, both PTFE and water surfaces are neutral (i). Upon immersing PTFE slides in water, contact electrification (CE) happens, resulting in positive and negative charges on water and PTFE surfaces, respectively (ii). As PTFE emerges, unbalanced charges attract electrons to flow from aluminum to copper electrodes, generating a current in the external circuit until fully separated from water (iii). When PTFE re-enters water, positive water forms an electric double layer (EDL) with PTFE, causing reverse electron flow to neutralize charges on the electrodes (iv). The LS-FluTENG demonstrates AC characteristics with a peak voltage of 6 V and a peak current of 300 nA.

2.2.3. Freestanding mode

A typical free-standing mode of TENG involves a free-moving triboelectric object and two electrodes [11, 13, 50, 64, 65, 67, 72, 74, 75, 137-143]. Once the free-moving object changes its position, the potential distribution is changed, resulting in the moving of the electrons between the electrodes. For instance, Zhang et al. [74] designed a U-shaped TENG with an FEP tube, Cu electrodes on its outer surface, and partially filled water (**Figure 1.4a**). The flowing water generates electrostatic charges, leading to energy generation through electrostatic induction on the electrodes, producing a peak voltage of 20 V and a peak current of 400 nA.. Similarly, D. Choi et al. [50] reported a water-based free-standing TENG (FS-TENG) where a water droplet moves freely on a lotus leaf with two conductive Au strips. As the droplet slides, changes in contact area generate negative and positive charges on the lotus leaf and the droplet, respectively. Electrons transfer between electrodes, creating an alternating electric current during the water droplet's sequential contact and detachment.. Furthermore, J. Wang et al. [25] presented an FS-TENG utilizing wind energy to accelerate the rotary motion. It features a freely moving FEP film between two stationary electrodes.
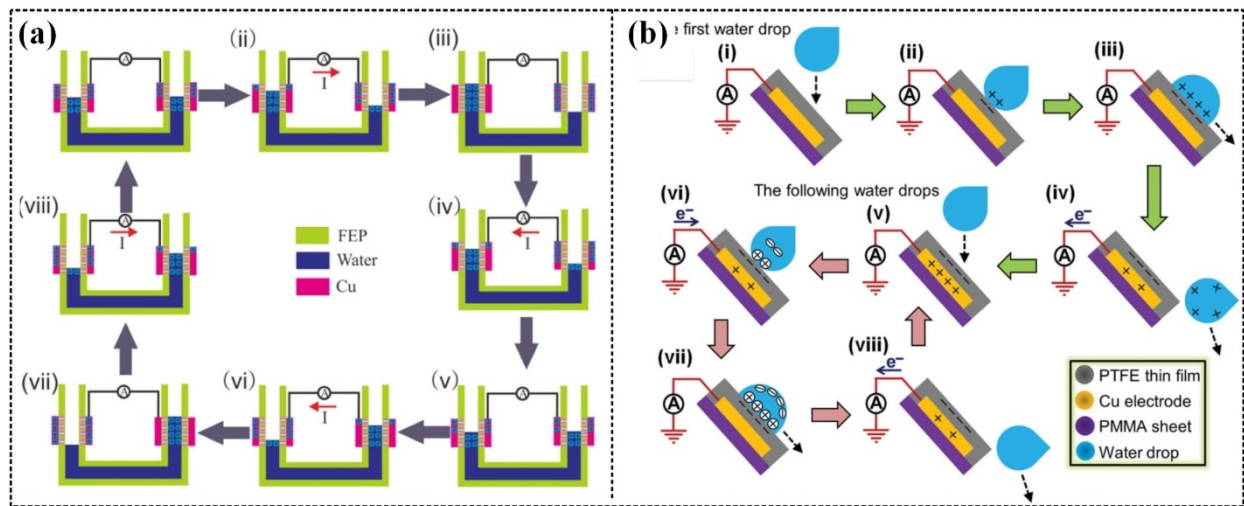
Figure 1.4: Working mechanism and the comparison of the measured results of open-circuit voltage and short-circuit current of (a) the freestanding [74] and (b) single-electrode modes [68].

2.2.4. Single-electrode mode

In the single-electrode mode of operation, electricity is generated by a lone electrode connected to the ground. When the free-moving object contacts the electrode, charges accumulate on the interfaces. As the object moves, the potential distribution changes, causing electrons to flow between the ground and the electrode, generating an electric current. This mode offers advantages over other modes like contact separation, lateral sliding, and free-standing modes [68, 69, 71, 79, 86, 144-150].

Lin et al. demonstrated a water-TENG with a superhydrophobic PTFE surface, working in a single-electrode mode, that can convert the energy from flowing water and falling droplets (**Figure 1.4b**) [68]. The device achieves a maximum voltage and current of 9.3 V and 17 µA, respectively, from a 30-µL water droplet. Upon droplet contact, a negatively charged PTFE surface and a positive electrical double layer (EDL) are formed, establishing electrical equilibrium. When the droplet leaves the PTFE, the equilibrium is disrupted, creating a potential difference across the Cu electrode and the ground, driving current flow. Periodic droplet falls result in continuous AC output due to this process.

2.2.5. Quantitative analysis

To provide a quantitative analysis of all modes of TENG, a universal edge approximation-based equivalent capacitance (EDAEC) method is developed by Li et al. [151] to demonstrate

15

charge distribution and the electric field in TENGs, as shown in **Figure 1.5.** The method involves creating analytical models and establishing a *Q-V-x* relationship for different TENGs. Equivalent capacitance models are used to depict charge distributions on electrodes. Due to contact electrification, static triboelectric charges disperse on the dielectric surface after contacting metal electrodes. The dielectric's triboelectric charge density, denoted as -σ, results in total charges of -σwL (with the dielectric layer's length and width as *L* and *w*). The metal electrodes carry equal and opposite-sign charges in total. Denoting the charges on electrodes 1 and 2 as *Q1* and *Q2*, the relationship is given by:

$$Q1 + Q2 = \sigma wL \tag{1.1}$$

Under short-circuit conditions, both electrodes share the same potential. Defining the electrodes and dielectric surfaces as nodes 1 and 2 and surface a, respectively, the equation becomes:

$$V1 = \frac{Q1}{C_{a1,total}} = V2 = \frac{Q2}{C_{a2,total}} \tag{1.2}$$

Thus, the short-circuit equilibrium charge Q1 and Q2 on electrodes 1 and 2, respectively, are given as:

$$\begin{cases} Q1 = \frac{1}{1+\frac{C_{a2,total}}{C_{a1,total}}} \sigma wL \\ Q2 = \frac{1}{1+\frac{C_{a1,total}}{C_{a2,total}}} \sigma wL \end{cases} \tag{1.3}$$

From the equations above, the working mechanism of TENGs can be easily illustrated. When the distance between surface a and electrode 2 is zero the capacitance across them would be much larger than that across electrode 1 ($C_{a2,total} \gg C_{a1,total}$). Most of the positive tribo-charges would be attracted to electrode 2. *Q2* is close to σwL and *Q1* is approximately zero. On the other hand, when the distance is quite large, the capacitance across surfaces *a* and electrode 2 would be much smaller than that across electrode 1 ($C_{a1,total} \gg C_{a2,total}$). So Q1 is close to σwL and Q2 is approximately zero.
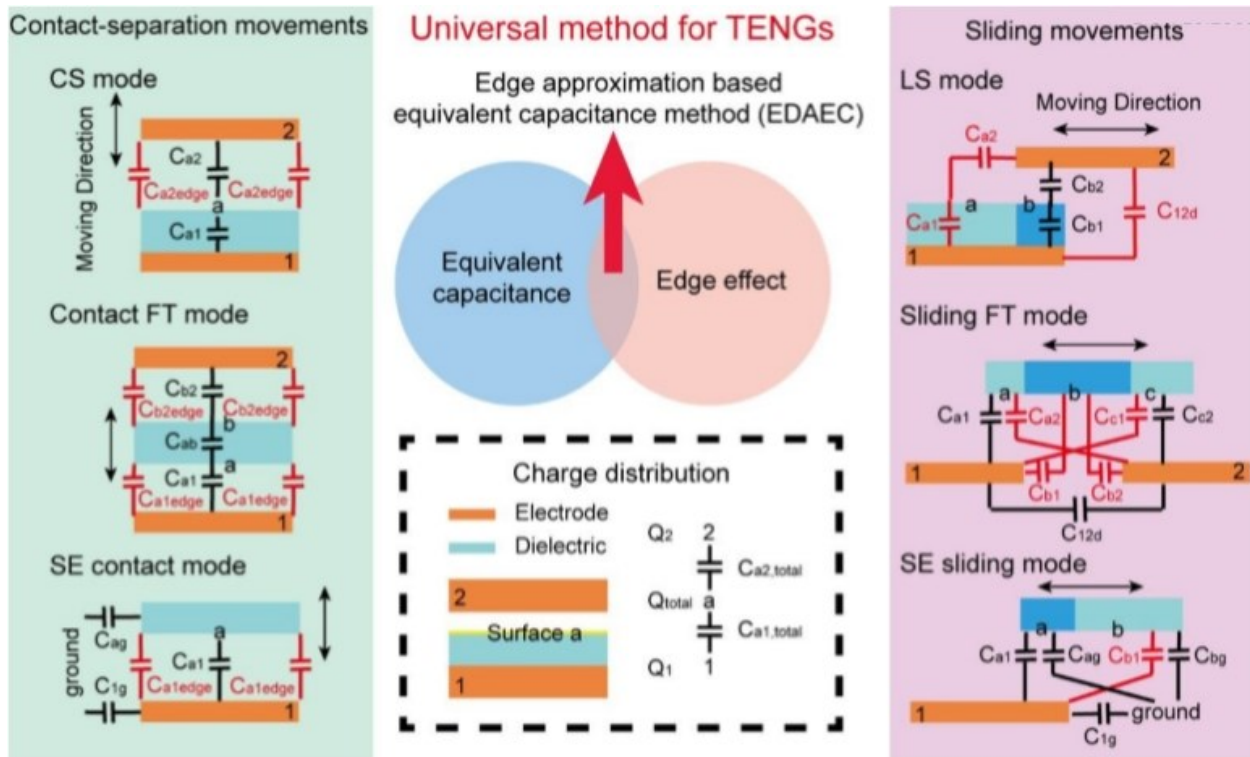
Figure 1.5: Schematic demonstration of the universal method for different kinds of TENGs. The capacitance caused by the side effect is in red. Reproduced with Permission from Reference [151], Royal Society of Chemistry 2019.

2.3. Affecting parameters

Aside from the extraordinarily rapid development of solid-solid TENGs [152-154], liquid-solid TENGs (L-S TENG) have also been becoming a potential trend due to their stable output and durability [13, 55, 74, 155-157]. Despite the complexity of studying the influencing parameters, ongoing research is actively addressing this challenge by focusing on factors impacting the output performance and durability of FluTENG devices. These factors can be categorized into liquid and solid phases. Liquid phase parameters, such as the type of liquid, viscosity, and surface tension, influence FluTENG performance. Solid phase properties, including the type of solid material, surface morphology, and structure shape, also affect device output. Understanding and optimizing these parameters are crucial for the widespread adoption of FluTENGs. Despite challenges, the potential benefits of this technology make it a promising field of research. By comprehending the influencing parameters, researchers can strive to develop more efficient and durable devices applicable in a broad range of applications.

The solid phase consists of two essential components: the contact layer and the electrode layer. The electrode layer's material selection is crucial for device performance, as materials with high electrical conductivity enhance electronic transfer from the contact layer, improving output efficiency. Conductivity and flexibility are essential considerations for TENG devices with diverse models. Commonly used materials like aluminum, silver, gold, and copper offer high conductivity, flexibility, commercial availability, and well-researched properties, making them ideal for TENG fabrication. Careful selection of electrode material is pivotal for TENG design and performance, enabling researchers to enhance output efficiency and durability and explore broader applications [158-161]. Moreover, a lot of other conductive material has been proposed due to their common flexible, stretchable properties and high chemical stability including carbon nanotubes (CNTs) [162, 163], graphene [164], nanowire-based materials [165], organic or polymer-based materials [166].

The contact or hydrophobic layer is crucial for enhancing TENG output, with materials ranked by triboelectric charge density (TECD) (**Figure 1.6**) [167]. Common materials like PVC, PTFE, PDMS, Kapton, and PVDF have TECD values of -117.5, -113.1, -102.2, -92.9, and -87.4 mC.m-2, respectively [167]. Besides that, Corona discharging can increase TECD more than 5 times [168]. The hydrophobic surface has also been researched a lot in improving output performance. Several ways have been used to fabricate high hydrophobic surfaces such as nanostructures or hierarchical structures [79], artificial lotus leaf structures [50], and plasma treatment [169]. Surface morphology, characterized by contact and sliding angles, impacts liquid velocity and bouncing motion, affecting output in the droplet single-electrode contact mode [127].

When considering the liquid phase properties, two main types are used: metal liquids (e.g., mercury, Galinstan) and water. Metal liquids are chosen for their liquid state, fluidity, and conductivity, often replacing solid metals as electrode layers [54, 170, 171]. On the other hand, water properties, including forms (droplet, waves, flow), ion type, and concentration, are carefully studied. Water form significantly impacts contact frequency and area, influencing output power. Droplet water studies investigate volume, falling height, and tilting angle effects on TENG output performance [172].
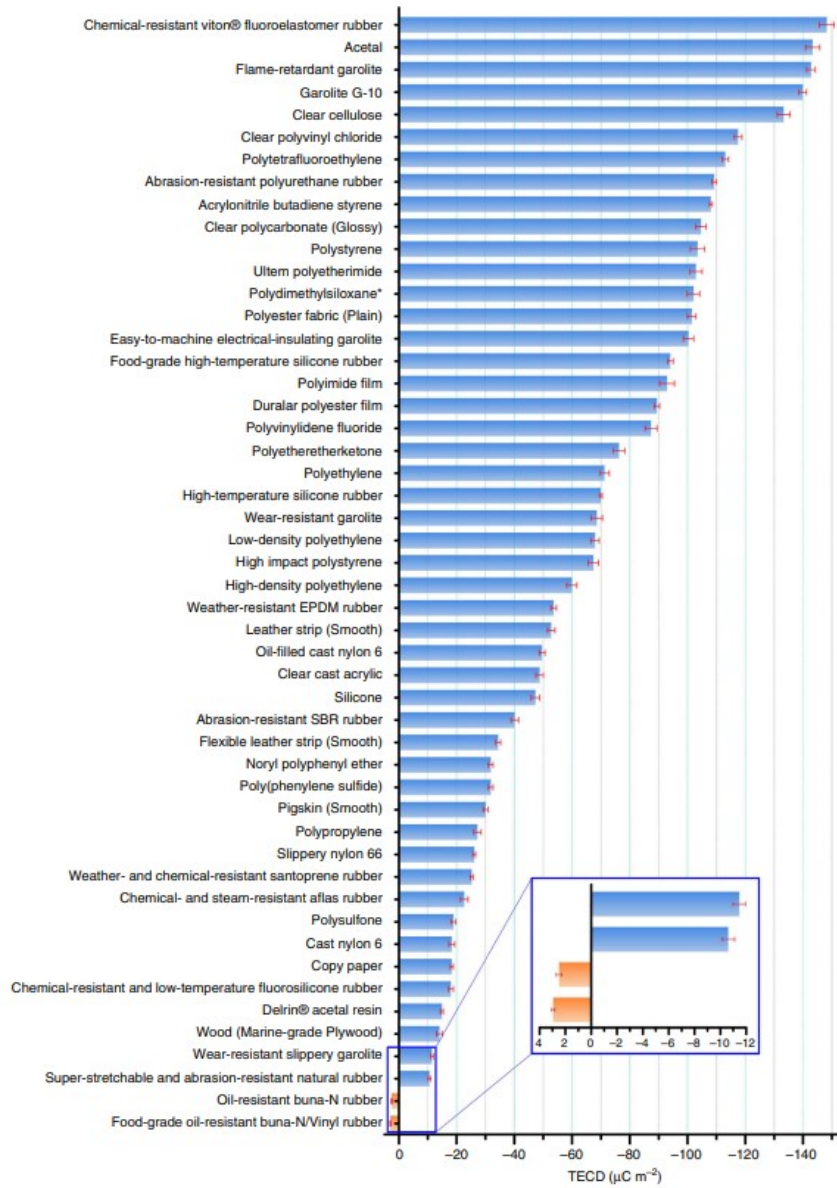
Figure 1.6: The triboelectric charge density (TECD) of different triboelectric materials [167].

It can be seen that a droplet's volume is proportional to the velocity of the droplet. Therefore, the inertial force is affected by the droplet volume and can be expressed as

$$\rho v^2 / D \qquad (1.4)$$

where ρ is density, v is velocity and D is the diameter of the droplet. However, the inertial force when the droplet moves down on the solid surface is still affected by the velocity of the

droplet increases with time (ϑ_t) due to the falling height (h) and tilting angle (θ). This relationship is expressed by the Equation 4:

$$\vartheta_t = \sqrt{2gh}\,sin\theta \qquad (1.5)$$

Due to the increment of the kinetic energy, ϑ_t increases, when falling height (h) increases, leading to an increase in the current output. Likewise, higher θ attributed to the increase of ϑ_t in Equation 1. However, the current output reaches saturation when the angle exceeds 45o and then drops down when the inclination angle is over 75°.

To optimize energy harvesting, researchers choose materials with a high negative charge, such as FEP, PTFE, and PVDF[78, 173, 174]. However, the F- F-bonding of the hydrophobic layer when in contact with liquid will absorb the ion with low electronegativity, which decreases the TENG performance [13, 93]. The high electrical conductivity ions are the reason for the low triboelectric charger on the hydrophobic layer. Besides, the adsorbed ions on the electrode layer will gradually reduce the transfer electron charge between the liquid and solid surface [175]. As shown in **Figure 1.7a,c**, the output voltage decreases when the ions concentration increases. With different types of ions (**Figure 1.7b,d**) the voltage also has different values.
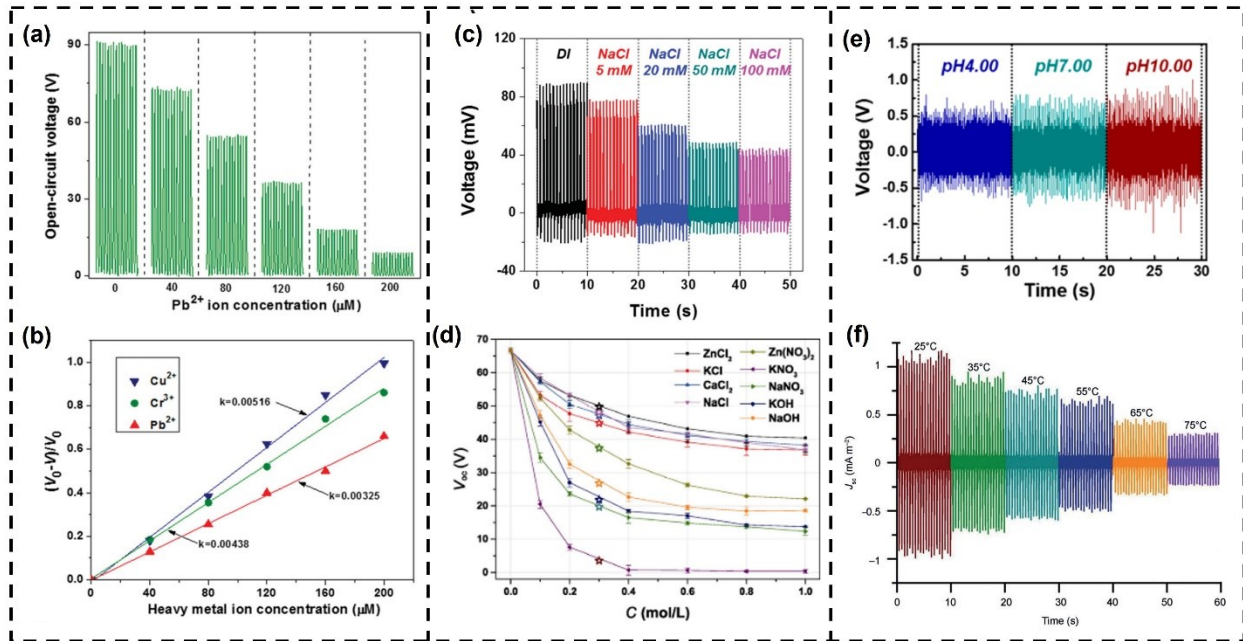
Figure 1.7: Performance characterization of FluTENG in different environments.

This suggests FluTENG's potential for ions or chemical detection. The pH value and temperature are additional affecting parameters. An increase in positive hydrogen ions (H+) leads to a decrease in output voltage (**Figure 1.7e**) [176]. Anions causing an imbalance in liquid molecule charges hinder interaction with the solid surface, harming TENG output performance. **Figure 1.7f** shows a decrease in short-circuit current density (Jsc) with increasing water temperature due to changes in water's dielectric constant and polarity [135].

Furthermore, to boost output power, researchers optimize surface properties, particularly hydrophobicity and charge density of solid surfaces [50]. High hydrophobicity provides stability, robustness, and high-output performance [46, 61, 86, 127]. Increased hydrophobicity expands effective contact areas with the liquid, resulting in higher current density. For example, modified PTFE with a rhombic pattern achieved a power density of 9.62 W/m² and an energy conversion efficiency of 63.2%, outperforming pristine PTFE with a power density of 0.5 mW/m² and energy conversion efficiency of 12.6% [62]. X. Li et al. demonstrated that with higher hydrophobicity, TENG devices can generate more output current [57]. To enhance surface hydrophobicity and charge density, M. Xu et al. proposed etching a PTFE film through inductively coupled plasma (ICP) reactive ion etching for 300 s, using reaction gases like 15.0 sccm Ar, 10.0 sccm O2, and 30.0 sccm CF4 in the ICP process [86].

On another hand, the designed structure of the TENG devices is also an important factor that can improve output performance [128, 129]. B. K. Yun et al. [67] developed cylinder-shaped interdigital electrode (IDE) based TENGs, which demonstrated 3.6- and 2.4-fold higher output compared to one- and two-electrodes-based TENG, respectively. As a water-based TENG, the properties of the water which relate to the ion type and concentration are also a factor that affects the output performance of the TENG [13]. X. Yang et al. [62] developed a TENG and reported that their maximum short-circuits current density of 0.28 mA/m^2, 7.82 mA/m^2, and 1061.86 mA/m^2 using DI water, tap water, and 0.6 M NaCl, respectively.

3. Energy harvesting technology

3.1. Water-based energy harvesting

Water is one of the most energy sources that exist in nature in the form of raindrops, river water, tides, and ocean waves. Water-based energy sources have an enormous amount that can be

utilized as renewable energy sources to produce electricity. In comparison with other energy harvesting technologies, the generated electricity from the water-based is continuous and stable, because of its advantages in environmental conditions, such as low influence from daytime, compared with solar devices which cannot work at night [177]. **Table 1.1** presents a summary of the achievement of water-based TENG devices. The water-based TENG can harvest energy from water droplets [64, 70, 80, 120, 178-180], water streams [181, 182], or water waves [22, 23, 38, 40-42], with variable output power densities.

Table 1.1: Summary of the achievements made in the water-based triboelectric nanogenerator devices

No.	Authors	Contact Mode	Power sources	Output power/power density	Materials	Application	Ref.
1	D. Joo et al.	Freestanding	Raindrops	1 mW/m^2	Water – MM-glass	Energy harvesting	[64]
2	Q. Liang et al.	Single-electrode	Raindrops	27.86 mW/m^2	Water – PTFE	Energy harvesting	[178]
3	S. B. Jeon et al.	Single-electrode	Raindrops	0.27 mW/m^2	Water – PDMS	Energy harvesting	[179]
4	L. Zheng et al.	Single-electrode	Raindrops	4.2 mA/m^2	Water – PTFE	Energy harvesting	[180]
5	Z. Liu et al.	Single-electrode	Raindrops	1.74 mW/m^2	Water – PDMS	Energy harvesting	[120]
6	S. S. Kwak	Freestanding	Single Droplet	1.9μW	Water – Graphen/PTFE	Energy harvesting	[70]
7	R. K. Cheedrala et al.	Single-electrode	Stream	12.53 mW/m^2	Water – PVDF	Energy harvesting	[181]
8	G. Cheng et al.	Single-electrode	Stream	0.59 mW/m^2	Water – PTFE	Energy harvesting	[182]

9	N. Wang et al.	Single-electrode	Wave	25 μW/cm^2	FEP – Cu	Energy harvesting	[22]
10	W. Liu et al.	Freestanding	Wave	0.21 W/m^2	FEP – Nylon	Energy harvesting	[23]
11	L. M. Zhang et al.	Contact-Separation	Wave	128 kW/km^3	FEP – Cu	Energy harvesting	[38]
12	S. L. Zhang et al.	Freestanding	Wave	3 W/m^3	PTFE – Nylon	Energy harvesting	[40]
13	D. Zhang et al.	Freestanding	Wave	4.2 mW/m^2	Kapton – Cu	Energy harvesting	[41]
14	Y. Bai et al.	Freestanding	Wave	7.3 W/m^3	PTFE – Cu	Energy harvesting	[42]

Energy from raindrops

An important water-based energy source is raindrops, which can harvest raindrop energy with a power output density of a few milliwatts per square meter level, as shown in **Table 1.1**. The devices operate in single-electrode [120, 178-180], contact-separation [80], or freestanding modes [64]. J. Nie et al. introduced a power generation from the interaction of a liquid droplet and a liquid membrane to harvest raindrop energy, as shown in **Figure 1.8** [80]. This liquid-liquid (L–L) TENG for raindrop energy harvesting, achieving open-circuit voltage (Voc) of 33 mV and short-circuit current (Isc) of 0.85 nA when a 40 µL droplet falls onto a liquid membrane from 3 meters. When a pre-charged liquid membrane is used, Voc and Isc reach 4 V and 60 nA, respectively. Water-based TENGs can also generate power when a droplet moves onto graphene, yielding 1.9 µW output, as reported by S. S. Kwak et al. [70].

Various mechanisms involve falling droplets interacting with charge-generating layers, inducing charges on electrodes and producing current.. The charge-generating layer could be an insulator [50, 64, 67, 68, 71, 79, 127, 139, 142, 144, 146-149, 183-188], semiconductor [143, 156, 189-192], or conductor [193] materials. Lee et al. [127] developed a water droplet-driven TENG (WdTENG) in contact-separation mode, generating peak voltage and current of 6.8 V and 6 µA,

respectively. Lu et al. [143] presented an LS-TENG with a semiconducting water droplet, producing 0.3 V and 0.64 µA with DC characteristics.

Recently, a new methodology of electricity generation has emerged based on a new electrode structure design. In this design, the charge from contact electrification directly transfers to the electrode upon droplet contact, offering unique electrical responses[147-149, 183, 185, 187, 188]. This leads to a different electrical response compared to traditional droplet-based TENGs. Xu et al. [188] demonstrated a PTFE device with an aluminum electrode, reaching high instantaneous voltage (143.5 V) and current (270.0 µA). These innovations suggest promising approaches for efficient raindrop energy harvesting.
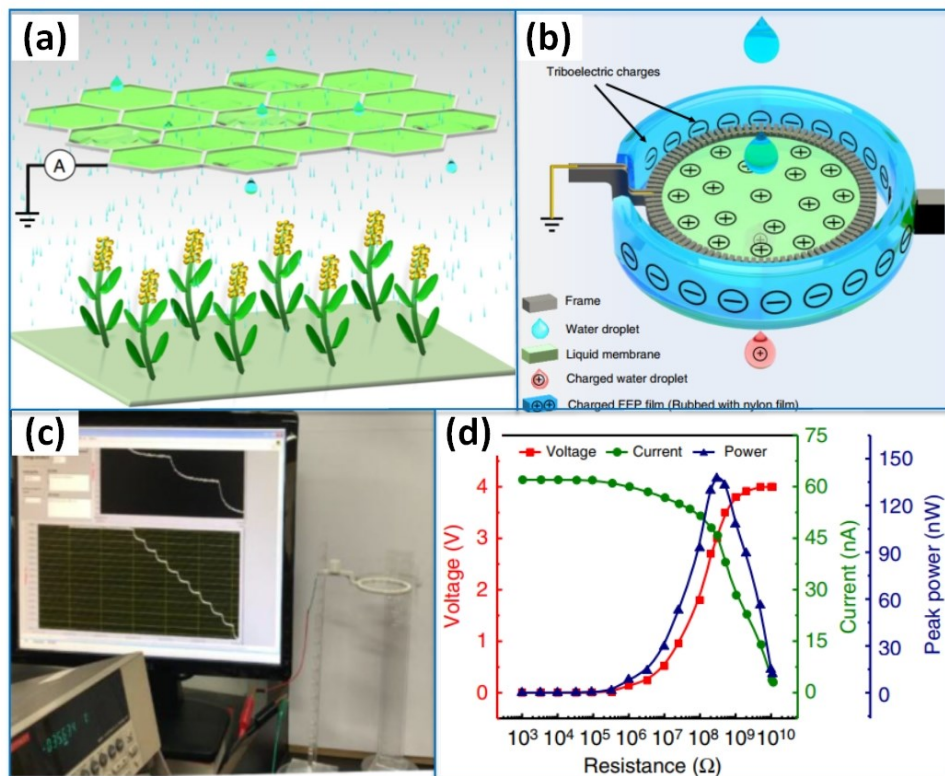
Figure 1.8: Concept of the liquid membrane for harvesting ambient electrostatic energy. (a) A schematic diagram of L–L TENG collects energy from raindrops in an irrigation system, while the motion behavior of raindrops is unaffected. (b) Falling droplets come into contact with the pre-charged liquid membrane. Schematic diagram of energy generation by using a charged liquid membrane. The liquid membrane is charged by the electrostatic field on an FEP film. (c) Screenshot of the real-time output signals of the water droplets passing through the charged liquid membrane. (d) Dependence of the ISC and power on the resistance [80].

Energy from water streams

Another important water-based energy source is the harvesting of energy from water streams, as proposed by R. K. Cheedarala et al. and G. Cheng et al. [181, 182]. A pulsatile Flow-TENG was developed to capture energy from unsteady peristaltic flow in a pipe, as shown in **Figure 1.9** [181]. In this research, The system captures energy from unsteady peristaltic flow in a pipe through contact electrification between a PVDF layer on the inner wall of a silicon pipe and flowing water.
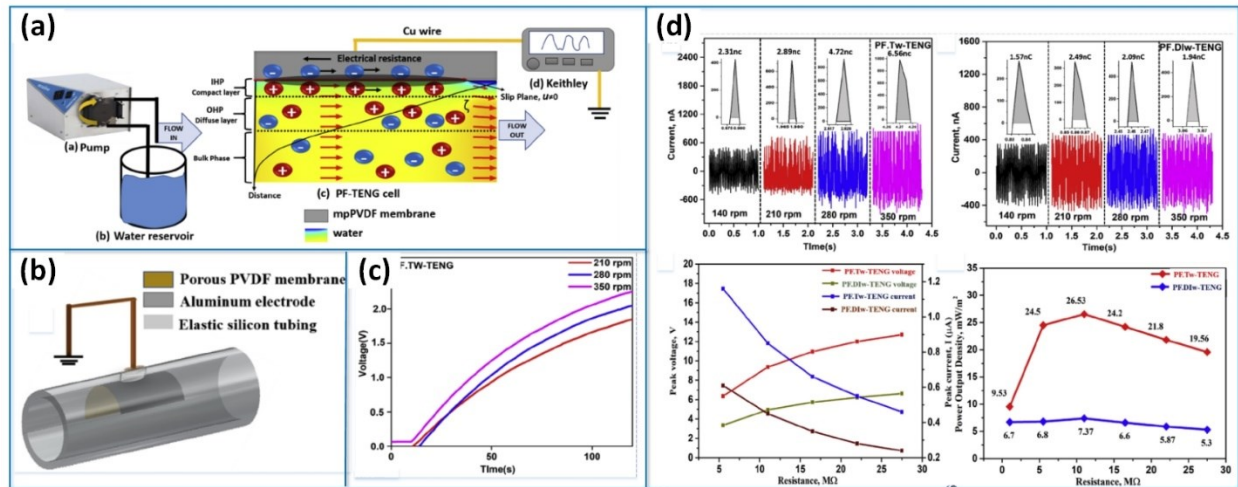
Figure 1.9: (a) Schematic diagram of the experimental setup showing peristaltic pump, water reservoir, TENG cell, and electrometer. (b) Schematic of the elastomeric tubing with TENG cell attached. (c) Rectified output of the PF.Tw-TENG at different pump speeds to charge a commercial capacitor of 4.7 μF. (d) Performance characteristics of the dependence on power output [181].

Moreover, this interaction mode enables the conversion of mechanical energy from water flow into electrostatic energy, subsequently transformed into electricity via electrostatic induction[13, 74, 75, 141, 150] or the breakdown effect [194]. Choi et al. [75] developed the SWING stick, exemplifying this process by converting mechanical energy from shaking into electricity. The stick generates electricity through CE between the water and Teflon, resulting in positive charges inside the water and negative charges on the Teflon surface. When the charged water contacts the bare Al tube, the generated charges inside the water are neutralized, generating a current through the external circuit. Other instances include the U-tube TENG developed by Zhang et al. [74] and Pan et al. [13], which can generate stable peak output voltage and current of about 20 V – 400 nA, and 350 V – 1.75 μA, respectively [74]. These devices can also function as multifunctional sensors, such as displacement and pressure sensors, with high sensitivity. Another example is the PTFE-copper (PCTENG) tube developed by Munirathinam et al. [150], harvesting energy from flowing

water and achieving peak voltage, current, and power of 36 V, 0.8 μA, and 45 μW, respectively, through CE between flowing water and the PTFE tube.

Energy from water waves

With over 70% of the Earth's surface covered by water, it holds vast energy potential. Blue energy, particularly water wave energy, is a crucial and promising source for sustainable societal development. Water-wave-based TENG devices operate in single-electrode mode [22], freestanding mode [23, 40-42], and contact-separation mode [38]. These devices exhibit output density ranging from a few milliwatts per square meter or a few watts per cubic meter of water, as shown in **Table 1.1**.

A practical bionic-jellyfish triboelectric nanogenerator (bjTENG) achieved sustainable output performance of 143V, 11.8 mA/m^2, and 22.1 μC/m^2 at a low frequency of 0.75 Hz and a water depth of 60cm (**Figure 1.10a**) [39]. It can directly power numerous green LEDs or a temperature sensor. N. Wang et al. developed a bio-inspired triboelectric nanogenerator (BITENG) capable of producing an output current of about 10μA and a voltage of 260V per unit. This is sufficient to drive at least 60 LEDs with a power density of 25μW·cm-2 under specific conditions (**Figure 1.10b**) [22].. Additionally, a high-performance tandem disk triboelectric nanogenerator (TD-TENG) (**Figure 1.10c**) [42] demonstrated excellent responsivity to low-frequency water waves, achieving a maximum peak power of 45.0mW and a maximum average power of 7.5mW in wave tank tests, with an average power density of 7.3 W/m3 under optimized design.
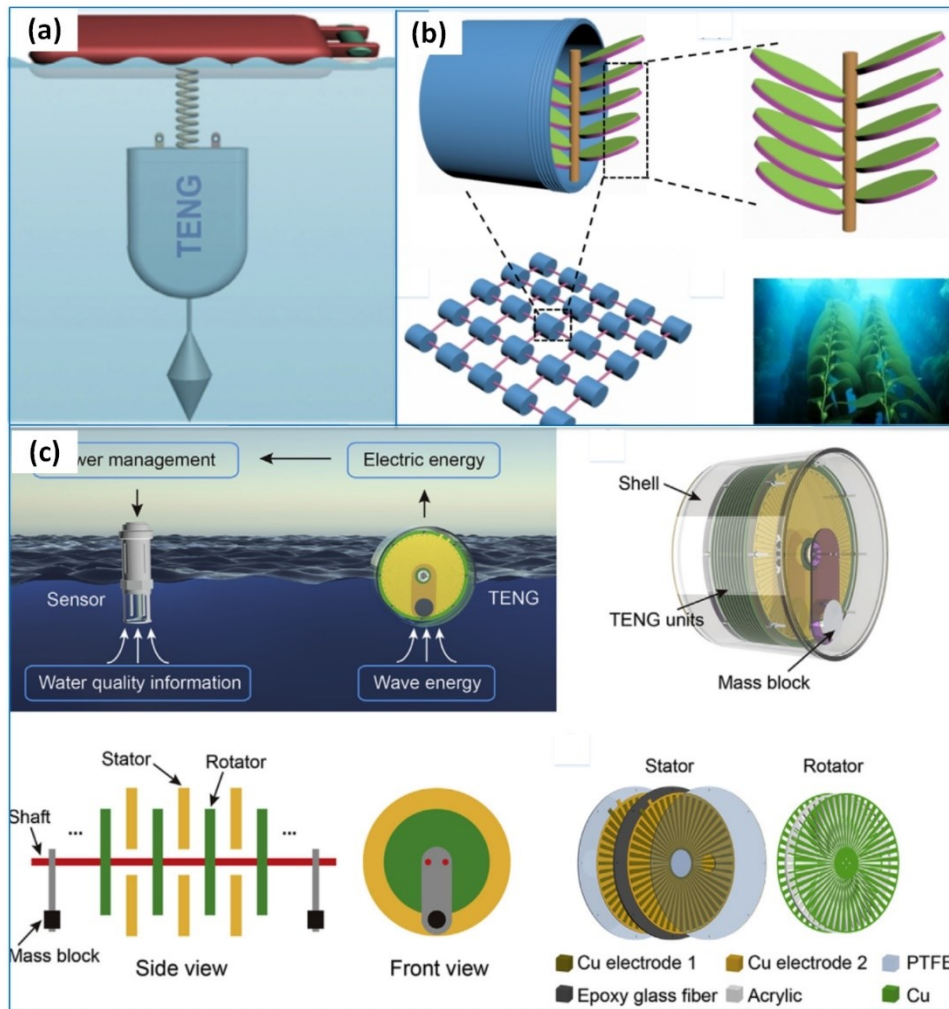
Figure 1.10: Schematic diagram of the experimental setup of (a) a practical bionic-jellyfish triboelectric nanogenerator (bjTENG) [39]. (b) A bio-inspired triboelectric nanogenerator (BITENG) [22]. (c) High-performance tandem disk triboelectric nanogenerator [42].

In another study, Zhu et al. [138] developed an LSEG using FEP thin film with an array of electrodes underneath. The LSEG generates AC electricity through triboelectrification and electrostatic induction during traveling water waves, offering an effective energy harvesting solution for onshore, offshore, and rainy areas. Li et al. designed a buoy LS-TENG, that can output a high current and voltage of 290 µA and 300 V by synchronizing the outputs of a network of 18 LS-TENGs [145]. The produced energy is suitable to power a wireless SOS system for ocean emergencies. Importantly, wave-based LS-TENG also demonstrated its potential to be used in self-powered sensor systems. Xu et al. developed an L-S TENG that can serve as a wave height sensor for smart marine equipment [86].

3.2. Air-based energy harvesting

The air-based TENG for energy harvesting will be reported in this section and the achievement made by air-based TENG is also summarized in **Table 1.2**. Almost of air-based have been developed based on the contact-separation, single-electrode, and lateral-sliding modes with two different designs, including flutter-based and rotary-based. An air-based TENG can generate a few microwatts to a few milliwatts, measured at megaohms level resistance of the external circuit.

Table 1.2: Summary of the achievements made in the air-based triboelectric nanogenerator devices

No.	Authors	Materials	Contact Mode	Design	Output power	Wind speed	Ref.
1	H. Phan et al.	PVC fiber – Al	Contact-Separation	Flutter	0.33 µW at 7 MΩ	4 m/s	[195]
2	H. Lin et al.	FEP – Ag NP – Al	Single-electrode	Flutter	0.82 µW at 4 MΩ	25 m/s	[33]
3	A. N. Ravichandran et al.	PC – Cu	Contact-Separation	Flutter	4.5 mW at 198 MΩ	5 m/s	[34]
4	X. Liu et al.	FEP – Cu	Contact-Separation	Flutter	67 mW at 18 MΩ	14 m/s	[30]
5	H. Kim et al.	PDMS – Al	Contact-Separation	Flutter	7.3 mW at 40 MΩ	9.1 m/s	[36]
6	Z. Zhao	Kapton – Ni	Contact-Separation	Flutter	135 mW/kg at 6.5 MΩ	22 m/s	[124]
7	Y. Feng et al.	PTFE/nature leaf - Cu	Single-electrode	Flutter	17.9 mW at 11 MΩ	7 m/s	[32]
8	X. Fan et al.	Silicon rubber – Al	Contact-Separation	Rotary	0.36 mW at 50 MΩ	9 m/s	[19]
9	Y. Xie et al.	PTFE – Al	Contact-Separation & Lateral-Sliding	Rotary	12 mW at 1 MΩ	15 m/s	[196]
10	M. T. Rahman et al.	PTFE – Al	Contact-Separation Lateral-Sliding	Rotary	1.67 mW at 10 MΩ	6 m/s	[31]

Flutter-based mechanism

An air-based TENG uses air-flow-driven vibration of a flexible nanostructured PTFE thin film in an acrylic tube, generating an average peak output of 2.4V and 1.7µA at 120L/min airflow, is reported in **Figure 1.11a** [88]. The maximum output power of the TENG device reaches 1.3mW at a load resistance of 15.1MΩ. An aerodynamic and aeroelastic flutter-driven TENG is presented in **Figure 1.11b** [195], which produces up to 0.33µW under mild airflow conditions at a load resistance of 7MΩ, a frequency of 206.4 ± 31.7 Hz for an airspeed of 13m/s (**Table 1.2**).

Z. Zhao et al. introduced a freestanding woven triboelectric nanogenerator flag (WTENG-flag) that can harvest high-altitude wind energy from arbitrary directions, with max Voc ~40V, Isc ~30µA, and peak power density of 135mW/kg at 22 m/s wind speed and 6.5MΩ resistance, as illustrated in **Figure 1.11c** [124].
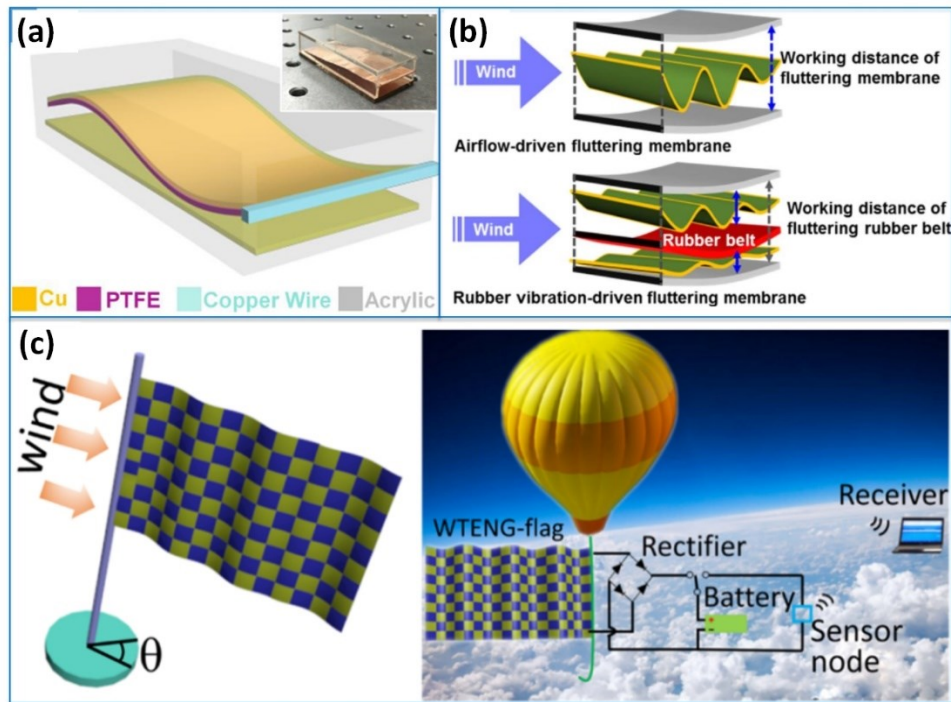
Figure 1.11: Flutter-based mechanism (a) Air-flow-driven TENG [88]. (b) Aerodynamic and aeroelastic flutters driven TENG [195]. (c) Freestanding Flag-Type TENG [124].

Rotary-based mechanism

A coaxial rotary freestanding triboelectric nanogenerator (CRFLU-TENG) wind energy harvester (**Figure 1.12a)** [197] generates 56 µA current and maintains a stable 650 V output voltage

at 1000 r/min. Output power increases from 2.5 mW to 9.7 mW as the rotating rate goes from 300 r/min to 900 r/min. With a wind velocity of 10 m/s, it charges a 100μF capacitor to 3 V in 15 s. J. Wang et al. [25] developed an anemometer TENG (a-TENG) for wind speed detection and a wind vane TENG (v-TENG) for wind direction monitoring (**Figure 1.12b**). The optimized a-TENG achieves an open-circuit voltage of 88 V and a maximum short-circuit current of 6.3μA, with a maximum power output of 0.47 mW at 6 m/s wind speed. In **Figure 1.12c**, an atmospheric pressure difference-driven energy harvesting methodology for harvesting low-frequency ocean wave energy is presented [21]. Flutter-driven TENG (FD-TENG) and disc-shaped TENG (DS-TENG) structures are demonstrated. FD-TENG achieves a peak power of 0.13 W/m^2 at 8 m/s, while DS-TENG reaches 0.7W/m^2 at 10m/s. The accumulated charge by FD-TENG increases from 5 μC at 2 m/s to 15μC at 8.0m/s in 12 s. DS-TENG achieves a Voc of 360V and σtr of 47μC/m^2 at 7 m/s airflow speed.
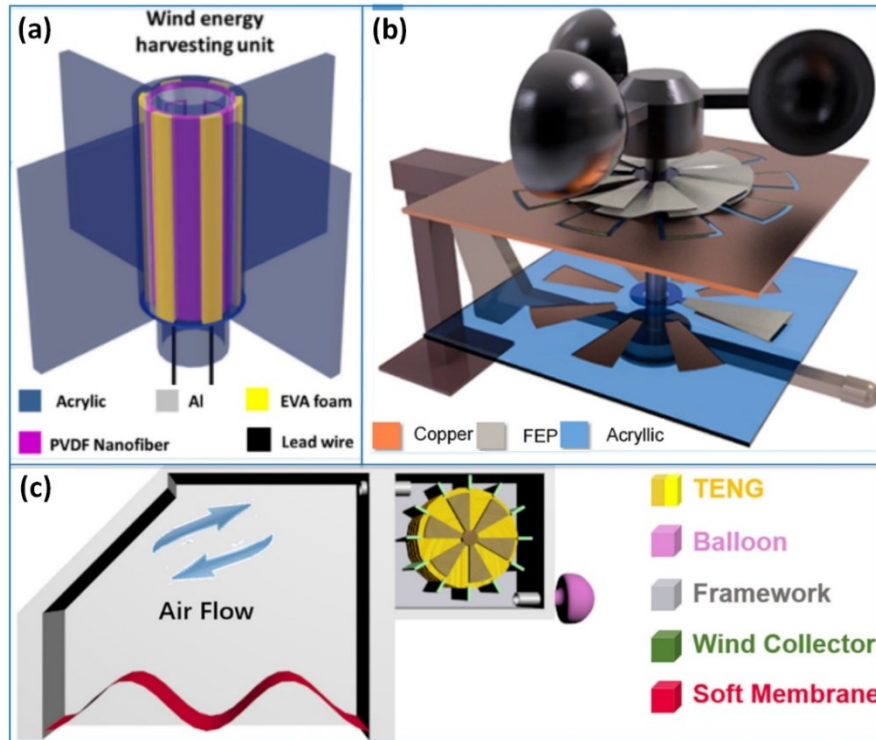
Figure 1.12: Rotary-based mechanism of (a) a coaxial rotatory freestanding triboelectric nanogenerator (CRFLU-TENG) wind energy harvester [197], (b) an anemometer TENG and a wind vane TENG [25], and (c) atmospheric pressure difference driven TENG [21].

3.3. Hybrid and large-scale applications

Hybrid systems

To harvest the wind energy and water flow energy, many research groups study the hybrid structure based on TENG technology, including electromagnetic (EMG) [19, 31, 55, 116], piezoelectric [31, 114], and solar [64, 120] technologies. M. L. Seol et al. proposed a ferrofluid-based triboelectric-electromagnetic hybrid generator, as shown in **Figure 1.13a** [55]. The TENG component exhibits a peak-to-peak open-circuit voltage (VOC) of 0.23 V and a peak-to-peak short-circuit current (ISC) of 2.7 nA. Similarly, the EMG component shows values of 1.8 mV and 2.5 µA, respectively. TENG achieves optimal output power in the mega-ohms to giga-ohms range, while EMG performs best in the ohms to kilo-ohms range.

On another hand, Y. Liu et al. combined a solar panel with a water-based TENG to create a hybrid silicon solar cell with a TENG for harnessing energy from sunlight and raindrops (**Figure 1.13b)** [120]. The water-drop TENG achieves a Voc of 3.27 V and an Isc of 0.49 µA in simulated rainy weather, resulting in a maximum average power density of 1.74 mW/m^2. This hybrid TENG/solar device showcases the capability to harvest both solar and raindrop energy.

In **Figure 1.13c**, a hybrid piezo-triboelectric nanogenerator (PENG) for wind energy harvesting was proposed by C. Zhao et al. [114]. The TENG achieved a high output voltage of 190 V at 10 MΩ, while the PENG had a higher output current of 375 µA at 1 MΩ. The hybrid H-P/TENG combined the advantages of both, with an estimated average output power of 10.88 mW at ~1MΩ, corresponding to an output power density of 6.04 mW/cm^2.
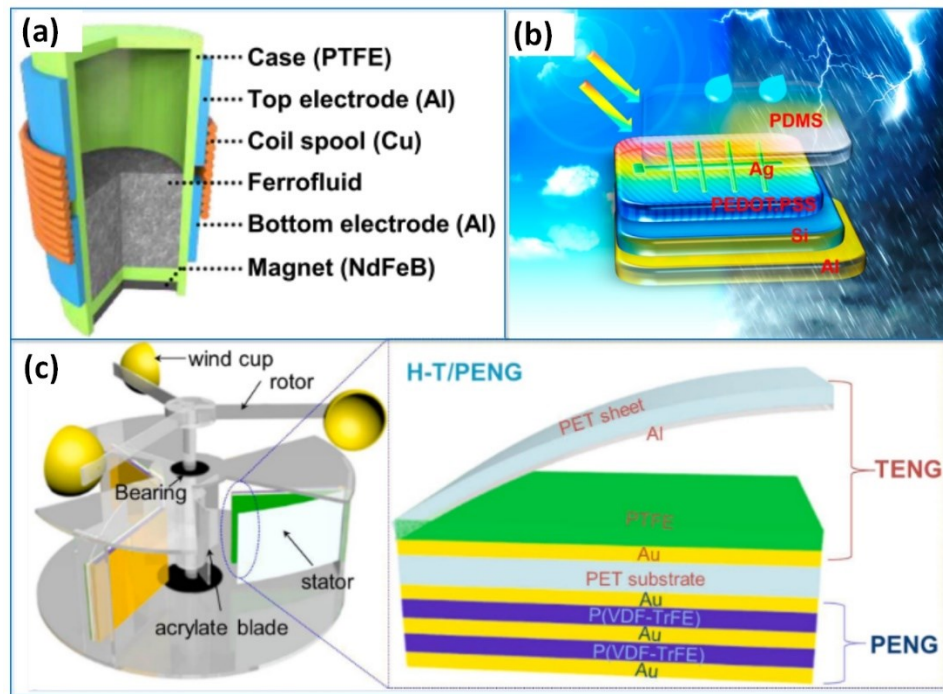
Figure 1.13: Hybrid energy harvesting system. (a) Electromagnetic-triboelectric hybrid generator [55]. (b) Solar-triboelectric hybrid generator [120]. (c) Piezo-triboelectric nanogenerator [114].

Large-scale applications

Due to TENGs' advantages such as lightweight, scalability, and ease of fabrication, TENG is a promising candidate for large-scale energy plants for sustainable energy harvesting. Ahmed et al. proposed a wind energy harvesting farm with TENGs, generating 1.11 MW in a 2 km² area (**Figure 1.14a)** [29] . As shown in **Figure 1.14b**, a flow-induced snap-through TENG can be realized as a large-scale system to harvest wind energy [36], achieving amaximum output power of 7.3 mW at a wind speed of 9.1 m/s, capable of powering 250 LEDs.

For water wave energy, a torus-structured triboelectric nanogenerator array [23] and rationally designed sea snake structure-based TENG [40] were proposed (**Figures 1.14c** and **d**), generating power densities of 0.21 W/m² and 3 W/m³, respectively. These low-cost, lightweight TENG networks hold great potential for ocean wave energy harvesting [14, 198]. However, in considering the marine environment, several TENGs have to be packaged to protect the TENG's electrodes from the seawater. The package materials should be considered based on their anticorrosive, heat resistant, radiation stable, and chemically inert.
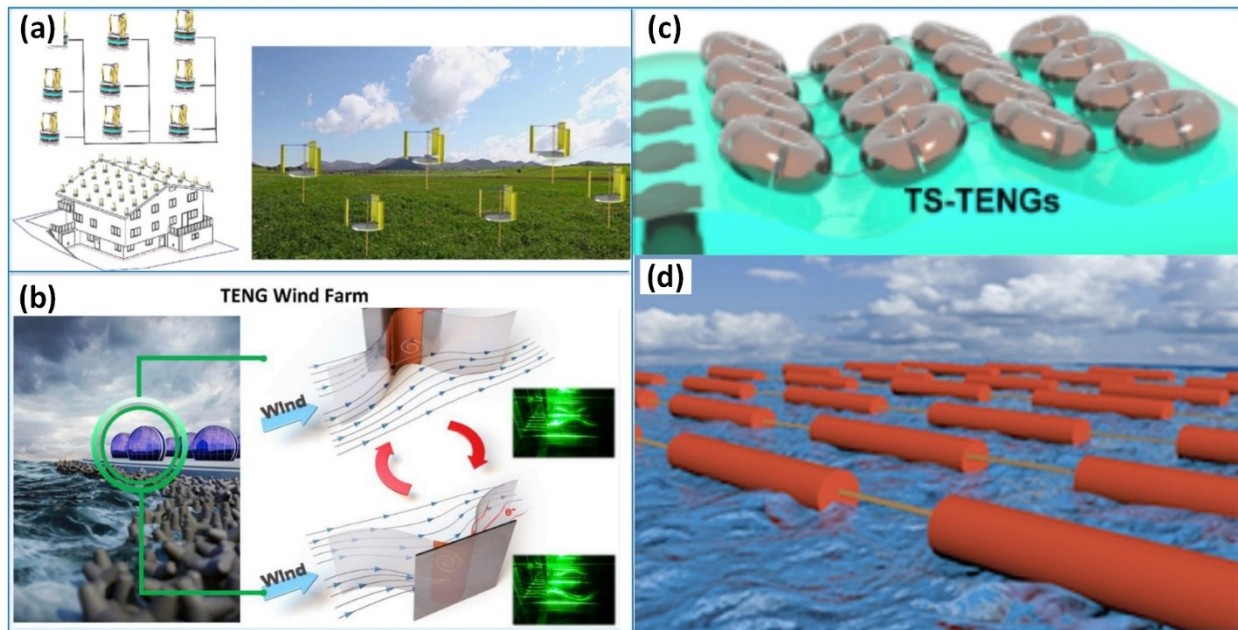
Figure 1.14: Large-scale applications. (a) Farms of triboelectric nanogenerators for harvesting wind energy [29]. (b) Flow-induced snap-through triboelectric nanogenerator [36]. (c) Torus-structured triboelectric nanogenerator array for water wave energy harvesting [23]. (d) Rationally designed sea snake structure-based TENG for water wave energy harvesting [40].

4. Self-powered sensing technology

4.1. Active physical sensors

The trend of development of the world electronic technology follows a general trend of miniaturization, portability, and functionality, then developing a range of sensors including but not limited to navigation, motion, chemical, biological, and gas sensors [9]. Since first introduced in 2012 by Wang's research group, TENGs for self-powered sensing applications have received significant attention as a high impact in smart systems and IoT networks, because of their advantages, such as simple structure configuration, and multifunctional power generation from multiple sustainable sources [199]. TENG devices show that they can become a promising candidate to achieve the development trend and can provide an alternative and self-powered approach to monitor various characteristics. Therefore, TENGs, including fluid-based TENG, have been designed with a large potential for application in a wide range of sensing devices, such as pressure/force sensors [58, 74, 87], velocity sensors [20, 25, 26, 35, 59, 121-123], temperature sensors [27, 76, 124], humidity sensors [124], and chemical monitors [49, 53, 94, 125, 126].

33
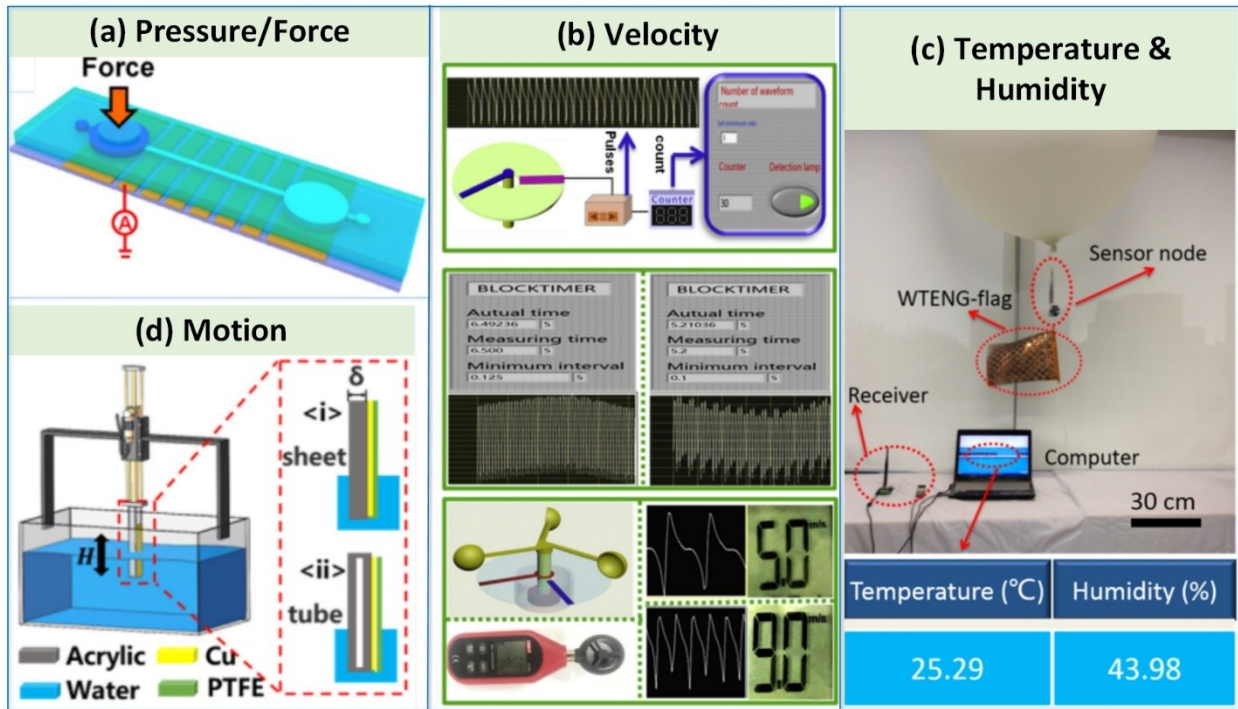
Figure 1.15: Fluid-based TENG for self-powered sensing applications: (a) Liquid triboelectric microfluidic sensor for pressure sensing [87]. (b) Velocity sensor [20]. (c) Temperature and humidity sensors [124]. (d) Motion sensor [86].

Pressure/force sensors are important functional components as the interface between mechanical motion and an electric signal in monitoring systems. As illustrated in **Figure 1.15a**, Q. Shi et al. [87] developed a self-powered liquid triboelectric microfluidic sensor for pressure/force sensing, where external force activates water flow in the channel, generating an electric current. With a force sensitivity of 0.0323 nA/N, the short-circuit current increased from 1.19 nA to 1.62 nA as the force varied from 0.4 N to 11.6 N. Besides, X. Zhang et al. [74] introduced a smart U-tube for dynamic pressure sensingWhen pressure is applied to the U-tube, the largest height difference between the two column fluid levels is ΔH. The acceleration (a), with respect to a constant vibration frequency, is completely dictated by the vibration amplitudes (x), and the transferred charge can be calculated by equation 2:

$$Q_{SC} = 2\pi\sigma r\Delta H \tag{1.6}$$

Where σ is the surface tribo-charges density, r is the diameter of the tube. From this equation, the short-circuit current at t is the time given by:

$$I_{SC} = 2\pi\sigma r \frac{d\Delta H}{dt} = 2\pi\sigma r V(t) \qquad (1.7)$$

Where V(t) is the water flow rate. As can be seen, short-circuit current (ISC) is proportional to V(t) and ΔH. Here, the applied pressure (P) into the U-tube can be represented by the height difference in liquid level, so the measured output performance is proportional to the pressure. The device shows a high sensitivity of 4.41 V/kPa and 72.94 nA/kPa for a range of [0.16; 0.5] kPa, as indicated in **Table 1.3**.

Similarly to pressure sensors, velocity sensors are also one of the most important types of sensing devices in many fields. A self-powered counter/timer-based TENG for wind speed detecting was realized by T. Zhao et al., as shown in **Figure 1.15b** [20], generating 3.5 to 7.5 V over a rotation speed range of 100 to 500 rpm.M. Xu et al. [35] introduced an aeroelastic flutter TENG (AFLU-TENG) serving as a wind speed sensor with a speed sensitivity of about 0.13 (m/s)/Hz or 7.7 Hz/(m/s).

For harvesting fluid-flow energy, including wind energy and blue energy, environmental effects must be considered seriously, especially the temperature and humidity, which have a significant effect on the output performance of the energy harvesting system. An innovative freestanding woven triboelectric nanogenerator flag (WTENG-flag) as a self-powered high-altitude platform with temperature/humidity sensing/telecommunicating capability was developed by Z. Zhao et al. [124], as shown in **Figure 1.15c** and **Table 1.3**. Also, a water-based temperature sensor was realized by J. Xiong et al. to measure the temperature of water in the range from 25 ± 5 °C to 95 °C with a sensitivity of 0.11 V °C−1 and 0.2 V °C−1 at impacting time of 5 s and 10 s, respectively [76].

On another hand, motion detection is important in various application fields, such as automatic control, robotics, surveillance, and smart marine equipment. M. Xu et al [86] developed a liquid-solid TENG (WS-TENG) for wave motion monitoring around marine equipment, demonstrating sensitivity to wave height in the millimeter range (**Figure 1.15d**). The fitting relationship of obtained Voc of WS-TENG shows the sensitivity of 14.1, 23.5, and 42.5 mV/mm, and a correlation coefficient of 0.9797, 0.9816, and 0.9981, for the electrode width of 5, 10 and 20 mm, respectively.

Table 1.3: Fluid-based TENG for self-powered sensors

No	Authors	Application	Material	Contact Mode	Sensitivity	Range	Ref.
1	Q. Shi et al.	Force	PDMS, water	Single-electrode	0.0323 nA/N	0.4-11.6 N	[87]
2	X. Zhang	Pressure	FEP, water	Single-electrode	4.41 V/kPa 72.94 nA/kPa	0.16-0.5 kPa	[74]
3	T. Zhao et al.	Velocity	PTFE, Al	Single-electrode	3.5-7.5 V	100-500 rpm	[20]
4	Z. Zhao et al.	Temperature	Kapton, Nickel,	Contact-Separation	16-11 µA	298-213 K	[124]
		Humidity			22-8 µA	10-96%	
5	J. Xiong et al.	Temperature	MSs mat, water	Single-electrode	0.2 V/°C	25±5– 95 °C	[76]
6	M. Xu et al.	Motion	PTFE, water	Single-electrode	42.5 mV/mm	10-80mm	[86]

4.2. Active chemical/environment sensors

Chemical detection and environmental sensing are crucial for maintaining the quality of water or wastewater. L-S TENG have been explored as self-powered sensors [13] responding to changes in liquid properties ion concentration [176, 200], organic concentration [159, 201], chemical detection [51], and biological response [95, 135].

For instance, in **Figure 1.16a**, the average output voltage of L-S TENG is shown with varying NaCl solution concentrations from 0 to 0.75 M [93]. The decline in voltage output with increasing NaCl concentration is observed. Similar studies indicate the impact of different ionic compounds on the TENG output [13, 69, 176, 202]. **Figure 1.16b** illustrates the sensitivity of the self-powered TENG sensor to NaCl concentrations, showing a linear relationship between output voltage ratio ($\Delta V/V$) and NaCl concentration, particularly sensitive in the range of 0.005 M to 0.1 M. **Figure 1.16c** and **d** illustrate the sensor's stated selectivity [175]. Modification agents like dithizone enable the detection of Pb2+, demonstrating higher output voltage ratios for additional heavy metal ions. The use of diphenylcarbazide yields similar outcomes for Cr3+. L-S TENG sensors exhibit

excellent selectivity and sensitivity in measuring ion concentration, making them promising for self-powered chemical sensing applications.
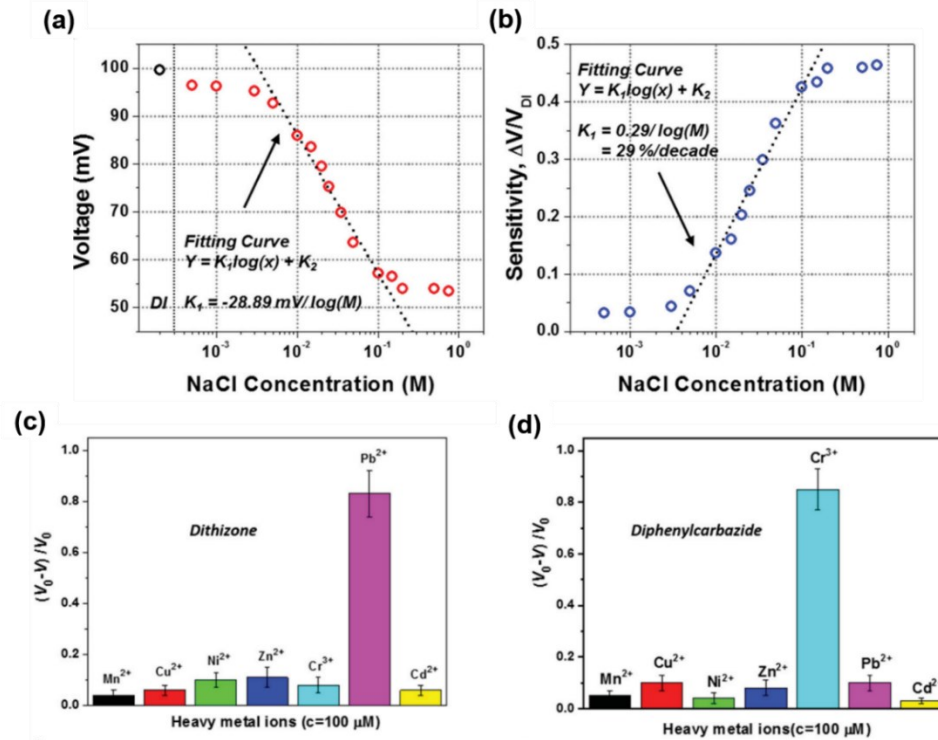
Figure 1.16: (a) Average output voltage values generated by various NaCl solution concentrations from 0 to 0.75 M and (b) the sensitivity of the sensor during its NaCl solution concentration [93]. A test of selectivity of the self-powered triboelectric sensor for (c) Pb2+ detection by using dithizone and as the surface modifying agent (d) Cr3+ detection by using diphenylcarbazide as the surface modifying agent [175].

Monitoring organic concentrations is vital in processes like fermentation and biomedicine. A self-powered sensor, using a triboelectric nanogenerator (TENG) device, has gained interest for detecting ethanol, formaldehyde, and glucose[159, 201]. **Figure 1.17** depicts a TENG sensor designed for organic concentration, employing industry-standard PTFE filtering membranes [52]. Positive charges accumulate on the PTFE surface as water is mechanically vibrated, generating an alternating current. Replacing water with an organic liquid reduces the TENG's current, providing an effective method for measuring concentrations of formaldehyde and ethanol.
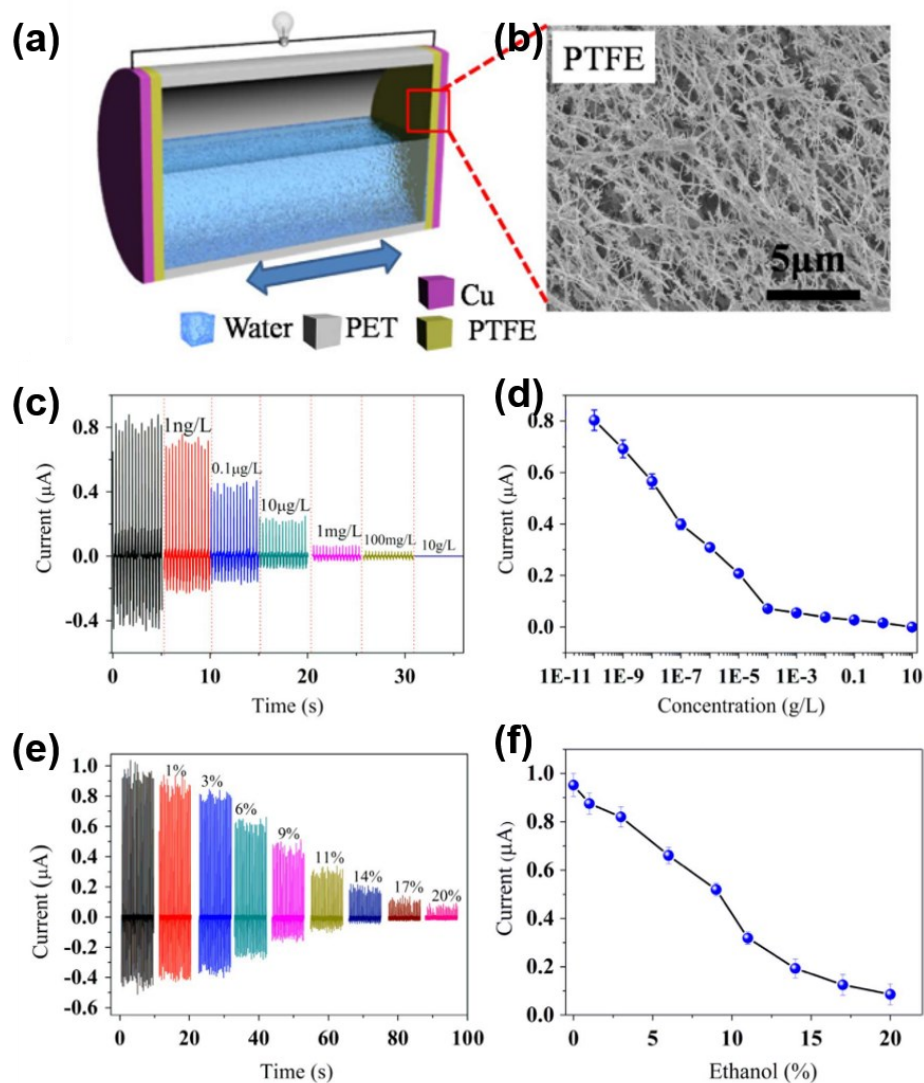
Figure 1.17: (a) Schematic illustration of the self-powered TENG sensor for organic concentration and (b) the FESEM image of PTFE membranes surface; (c, d) Short-circuit current for different formaldehyde concentrations and (e, f) Short-circuit current for different ethanol concentrations (percentage by volume) [52].

In addition to an application for self-powered sensors, chemical sensing has been developed in recent years, owing to life safety and industrial process control. **Figure 1.18a** and **c** illustrates the mechanisms of a single electrode L-S TENG (SELS-TENG) and contact-separation L-S TENG (CSLS-TENG) based sensors [49, 51]. The output signal varies with different chemicals. In **Figure 1.18b,** SLES-TENG exhibited positive peaks mainly around 100 nA for 99.7% alcohol detection, while for 99.5% acetone, it showed negative peaks around -80 nA. The current values

for sensing NaOH and NaCl also differed, around +200 nA and -250 nA, respectively. The varied ions in the liquid impact the output current, influencing the detection and classification of different liquids, as shown in **Figure 1.18d**.
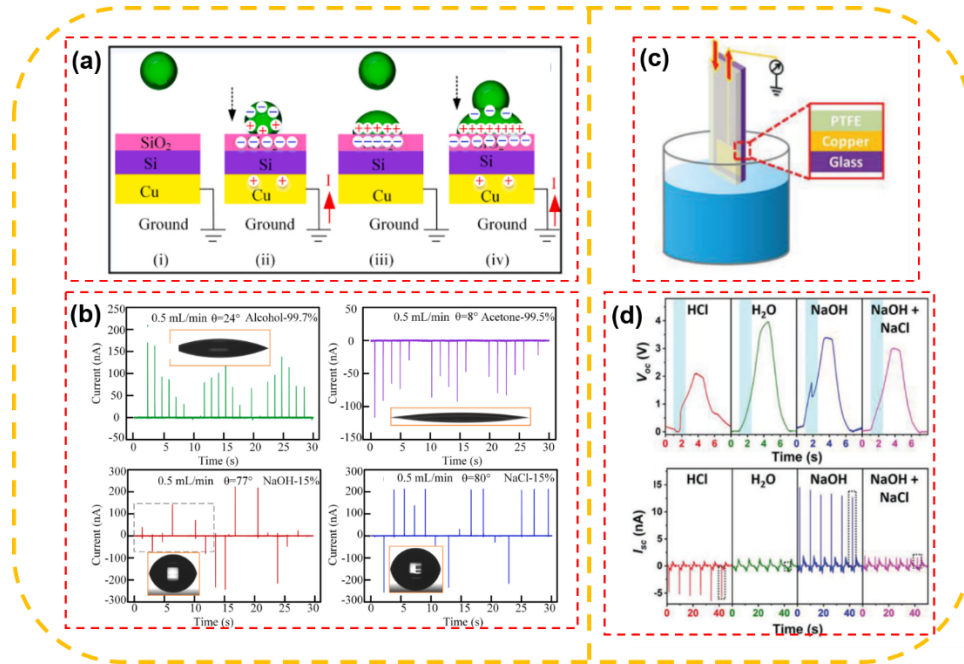
Figure 1.18: (a) The working mechanism of L-S TENG-based sensor and (b) Isc with different liquid alcohol, acetone, NaOH liquid, and NaCl liquid [51]. (c) Schematic illustration of the L-S TENG and (d) Voc and Isc in paraffin oil/water with different aqueous solutions of HCl (0.1 mol.L−1), deionized water, NaOH (0.1 mol.L−1), and mixture solution of NaOH and NaCl (0.1 mol.L−1) [49].

5. Summary and perspectives

This chapter provides an extensive overview of the fundamental principles of FluTENG technology, emphasizing its potential for harvesting energy from various fluid sources like raindrops, water streams, waves, and wind. FluTENGs offer numerous advantages, including low cost, lightweight, scalability, and versatility in harvesting different energy sources. This technology holds promise for large-scale applications and aligns with trends in miniaturization, portability, and functionality, making it valuable for smart systems and IoT networks.

Despite its promise, FluTENG is a relatively new technology, and further research is needed to enhance its performance. Improving electrical output, addressing industrialization challenges, ensuring environmental suitability, and establishing standardization are key areas of focus. Notably,

material selection and properties play a crucial role in FluTENG development, including optimizing charge-generating, charge-trapping, charge-collecting, and charge-storage layers.

For successful practical application, efforts should be directed towards converting AC-type electricity generated by TENG into DC-type, as well as developing flexible and stretchable capacitors and rectifiers for energy storage. Ensuring electrical stability between components and enhancing the durability of FluTENG in harsh environments are essential considerations.

Additionally, while FluTENG has shown potential for energy harvesting, it is essential to explore its use in self-powered sensor systems. Self-powered sensors offer significant advantages in terms of energy efficiency and longevity. Challenges in optimizing FluTENG for specific sensing applications and addressing wear and tear need to be addressed. The development of innovative energy conversion mechanisms is a priority, particularly for DC power generation, to advance the efficiency and accuracy of self-powered sensor systems. This research direction aligns with the broader goals of sustainable and smart technology development.

CHAPTER II – A NOVEL TRIBOELECTRIC GENERATOR BASED ON DIRECT CHARGE TRANSFER BETWEEN LIQUID-TREATED SOLID FOAM AND METAL CONTACTS

This study introduces a cellulose-based triboelectric generator (C-TEG) that presents a novel approach to generating power from mechanical energy using a remarkably simple structure. The device consists of two electrodes positioned on the surface of a dielectric layer, collecting direct-current output generated by the sliding motion of a liquid-treated solid foam made of water and cellulose. In this setup, mechanical energy is converted into electrostatic energy through the triboelectric effect, followed by the generation of electrical energy as a result of direct charge transfer between two electrodes with different work functions. This method differs from the traditional TENGs, which rely on the electrostatic induction process. A single C-TEG can produce a current density of 75 µA/cm2 and an induced voltage of approximately 0.48–0.90 V with direct-current characteristics. By connecting multiple C-TEG units in series or parallel, the voltage and current outputs can be further increased. Moreover, C-TEG proves exceptional accuracy in measuring the ion concentration in an aqueous solution ($R^2 = 0.996$). These findings highlight the significant potential for applying C-TEG as an efficient strategy for harvesting mechanical energy in the field of self-powered sensor development.

1. Introduction

Over the past few years, the challenges posed by climate change and energy shortages have become increasingly extreme, thereby highlighting the pressing need for clean and renewable energy [203]. Despite the vast amounts of energy contained within human footfalls, ocean waves, raindrops, and airflow, a significant portion of it is wasted due to the difficulty of harnessing it effectively [204, 205]. Therefore, it is crucial to develop suitable technology to tap into this energy source, and advancements in nanotechnology have led to the creation of various nanogenerators for harvesting mechanical energy [206-208]. Zhong Lin Wang and his team developed triboelectric nanogenerators (TENGs) which use electrostatic induction and triboelectric effects to turn mechanical energy into electricity [8-10]. In the triboelectric mechanism, the triboelectric effect occurs when two different materials are physically in contact, in which one material tends to lose electrons while the other tends to gain electrons. TENGs are capable of generating electricity from

various energy sources, including vibration, wind, wave water, and human motion, among others [209-212]. Since their inception, researchers have studied various TENG structures and functions to enhance their output performance and energy conversion efficiency [8, 68, 176, 213].

Recently, TENG has been demonstrated as an efficient energy harvesting strategy and opens opportunities to exploit a plethora of small energy sources. However, as it is well known, relative humidity is an important factor affecting triboelectrification with a negative trend. Many studies have shown that with the increase in humidity, the output performance of TENGs generally decreases due to the charge dissipation of triboelectric charges in the presence of water [214-216]. Therefore, searching for new materials with high triboelectric charges at high humidity is necessary. On another hand, most of the existing TENGs exhibit alternating current (AC) output characteristics due to CE and electrostatic induction. It would be inconvenient for directly powering electronic devices, where direct-current (DC) power is required. In this case, a rectification method is mandatory to produce DC power before use. Accordingly, the novel strategies and technologies for converting mechanical energy directly into DC electric energy are highly promising as a solution to solve the above problems [98-109]. Furthermore, it is necessary to provide sufficient power to run a device for various practical applications, hence, improving output power density, particularly output current, has become a significant interest in the DC energy harvesters investigation.

In the past few years, cellulose, one of the most abundant resources in nature, has been demonstrated as a promising functional material for the development of low-cost, eco-friendly technologies, including recent research on energy harvesting [217-219]. Cellulose contains abundant hydroxyl groups that endow cellulose with strong electron donation capacity, resulting in a great potential for triboelectric effect [220-224]. Notably, cellulose is hydrophilic and tends to strongly interact with water [225-228]. When cellulose contacts water, hydroxyl groups spontaneously form hydrogen bonds with water molecules, leading to fixing water molecules on the surface of cellulose and forming a conductive path by the hydrogen bond network of water molecules. This could be an explorable factor. Interestingly, Wang et al. [229] reported a TENG that can enhance the current output due to the participation of water molecules fixed by hydrogen bonds formed with hydroxyl groups in a polyvinyl alcohol film in triboelectrification, which increase the charge quantity and then triboelectricity. Presumably, cellulose could be used to solve

the problem of the decreasing trend of electricity performance in a high-humidity environment. On another hand, a well-known phenomenon that was thoroughly characterized by Lord Kelvin [230, 231], the charging effect between two materials with different work functions provides a promising method to generate electricity from mechanical vibration energy. When two materials with different work functions are electrically connected, electrons will be transferred naturally from the material with a lower work function to the materials with a high work function, leading to accumulating positive and negative charges on their surface, respectively. It results in developing a voltage across the materials. Varpula et al. [232] developed a work-function energy harvester (WFEH) that can generate electric energy by simply bringing two plates of electrodes with different work functions together.

In this chapter, for the first time, a cellulose-based triboelectric generator (C-TEG) is demonstrated as a new power generation methodology for harvesting mechanical energy. The device is mainly composed of two electrodes located on the surface of a dielectric substrate to collect electric output from the sliding motion of a liquid-treated solid foam made of water and cellulose. The mechanism of C-TEG is based on the triboelectric effect and direct charge transfer between two metal contacts with different work functions. The output performance of C-TEG is systematically investigated with different dielectric substrates, pairs of electrodes, properties of water, or structural design parameters such as the size of electrodes, the distance between them, and the size of the cellulose foam. This device is capable of producing a maximum current density of 75 μA/cm^2 with a transferred charge density of 23.7 μC/cm^2, a power density of 5.8 μW/cm^2, and an induced voltage of about 0.48–0.90 V. What is important is the fact that the current and voltage outputs can reach up to 2 mA and 2 V by simply connecting four unit cells in parallel and series, respectively. Remarkably, four cells of C-TEG in series can produce an output energy of 1.12 mJ within 140 s. The generated energy can be directly stored in a 1 mF capacitor without requiring any rectifier. This amount of stored energy is sufficient for powering many electronic devices. More interestingly, C-TEG proves a great accuracy and potential application for measuring the ion concentration of NaCl solution with high sensitivity and linearity ($R^2 = 0.996$). These results declare a high potential application of C-TEG in mechanical energy harvesting and self-powered ion concentration sensor systems.

2. Experimental section

2.1. Materials

For preparing the materials, aluminum and copper tapes were bought from Ducksung Hitech (Ducksung Hitech Co., LTD, Seoul, South Korea). The cellulose foam is manufactured by Hankook Tamina (Hankook Tamina Co., LTD, Hanam, South Korea). Deionized water and NaCl solution were used from our research laboratory. Tap water was obtained from a commercial source (K-water, South Korea). ITO electrode (10 Ω/sq), polytetrafluoroethylene film (PTFE, 100 µm - thick), and polyvinylidene fluoride (PVDF, 50 µm -thick) were purchased from Sigma-Aldrich (Sigma-Aldrich, St. Louis, MO, USA). Besides, the mica and nylon were purchased from a local market.

2.2. Structure design and fabrication

The components of the experimental setup are illustrated in **Figure 2.1**, which includes a rotational-to-liner motion transformer using a slider-crank mechanism to simulate the mechanical vibration, a C-TEG cell, and external measuring equipment. A typical C-TEG cell consists of a cellulose foam treated by absorbing water molecules and two dissimilar electrodes of the same size located on the surface of a dielectric substrate. To fabricate the C-TEG device, Al and Cu tapes were cut into rectangular pieces of the same size and attached to the surface of a dielectric substrate as two electrodes. A water-treated cellulose foam (WTCF), made by absorbing water into cellulose foam, will slide forward and backward on the surface of the dielectric substrate and two electrodes, resulting in the freestanding mode of operation of the C-TEG. The motion of the cellulose foam was driven by a rotational-to-liner motion transformer using a slider-crank mechanism under a fixed vibration frequency of about 0.5 Hz. To characterize the impacts of structure parameters on the output performance, Al and Cu electrodes were cut with different sizes (40 mm in length; 2, 5, 10, and 15 mm in width). Also, cellulose foams (5 mm in thickness; 40 mm in length) were prepared with different widths of 10, 15, and 30 mm. The distance between the two electrodes varied from 1 to 20 mm. Mica, nylon, PVDF, and PTFE were utilized as the materials of dielectric substrates. The concentration of NaCl solution was varied from 0 to 0.8 M (mol/L).
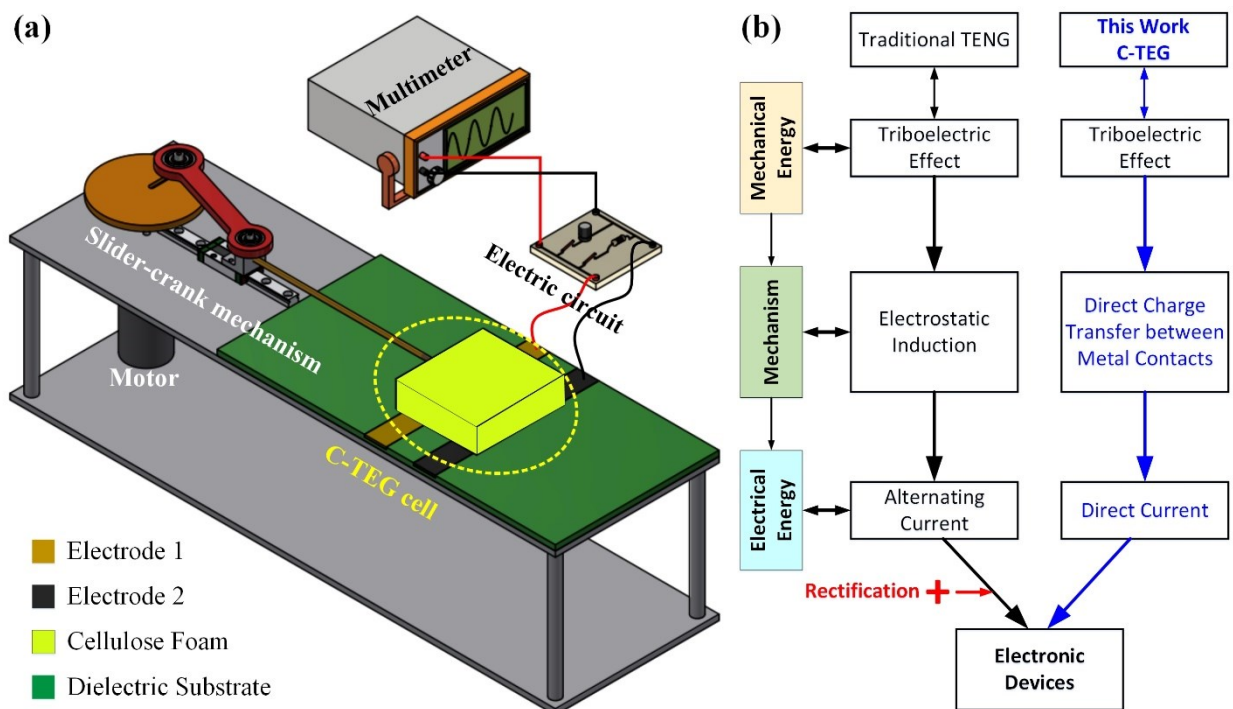
Figure 2.1: Schematic and experimental configuration of C-TEG. (a) Illustrations showing the experimental setup. (b) Schematic flow chart of the methodology of C-TEG in comparison with a traditional TENG.

2.3. Method and Measurement

Figure 2.1b displays the flow chart of the methodology of C-TEG in comparison with a traditional TENG. As can be seen, the C-TEG is based on a novel approach to mechanical-to-electrical energy conversion, in which mechanical energy is converted into electrostatic energy by the triboelectric effect. Then, electrical energy is obtained due to the direct charge transfer between two metal contacts with different work functions. This mechanism differs from electrostatic induction used in traditional TENGs. Consequently, C-TEG can produce DC outputs, while a traditional TENG exhibits AC outputs. The ability to generate DC outputs enables the C-TEG to directly charge an energy storage unit without requiring a rectifier.

For measurement of the electric outputs of C-TEG, a Digit Graphical Sampling Multimeter model DMM7510 of Keithley Instruments, Inc. (Cleveland, OH, USA) was used. This measuring instrument has an enhanced accuracy DC-current function that can measure a 1 µA sleep mode current with 1 pA resolution and with 0.375 nA tolerance, an enhanced sensitivity with 100 mV range with 10 nV resolution, and a high input impedance of more than 10 GΩ. A JEOL Field

Emission Scanning Electron Microscopes (FE-SEM) model JSM-7600F (Tokyo, Japan), was used to measure the morphology of the cellulose foam. The contact angle measurement was realized by SmartDrop (Femtofab Co. Ltd., Korea). In addition, the elemental composition and chemical states of the cellulose foam were analyzed using a Thermal Fisher model Nicolet iS5 FT-IR Spectrometer (Madison, Wisconsin, USA). The crystal structure of the cellulose foam was analyzed by an X-ray diffractometer system (D/MAX-25000V, Rigaku, Tokyo, Japan) using monochromatic CuKα radiation with the wavelength λ = 1.54178 Å.

3. Results and discussions

3.1. Characterizations

Figure 2.2a illustrates the three-dimensional representation of the C-TEG, showcasing the parallel alignment of Cu and Al electrodes, which are considered electrodes 1 and 2. This arrangement allows the effective collection of triboelectricity generated by the motion of a WTCF across the surfaces of the mica substrate and electrodes. As cellulose foam absorbs water, its hydroxyl groups interact with water molecules, leading to the creation of a hydrogen-bonded network. Subsequently, this network establishes a conductive path within the treated foam, facilitating the transfer of charges during the electricity generation process [229]. Additionally, water molecules are fixed to cellulose foam into one reactive entity and participate in triboelectrification as highly electropositive materials.

To explore the significance of the cellulose foam, a comprehensive analysis of its characterization was conducted. The cellulose foam's morphology was evaluated through FE-SEM analysis, and the results are presented in **Figures 2.2b-d**. The FE-SEM images reveal a three-dimensional porous network structure consisting of interconnected pores. These pores comprise numerous macropores (>50 µm) distributed randomly across the surface, constituting the primary structure and establishing an open channel system, (**Figure 2.2b**). This foam-like architecture creates a conduit for water absorption, enabling the foam to retain considerable water volumes [233]. Furthermore, micropores are found along the walls of the macropores, representing a secondary structure (**Figure 2.2c**), and a third-order with super-porous structures with dimensions of up to 1 micrometer (**Figure 2.2d**). This specific structure enhances the network's microporosity, resulting in an improved capacity for water absorption [234]. Highlighting the exceptional

46

hydrophilicity of the foam, as evidenced in **Figure 2.3**, a water droplet (3 µL) was rapidly absorbed upon contacting the foam's surface for 100 ms, ultimately resulting in a contact angle of zero. This impressive behavior can be attributed to the specific morphology we discussed earlier.
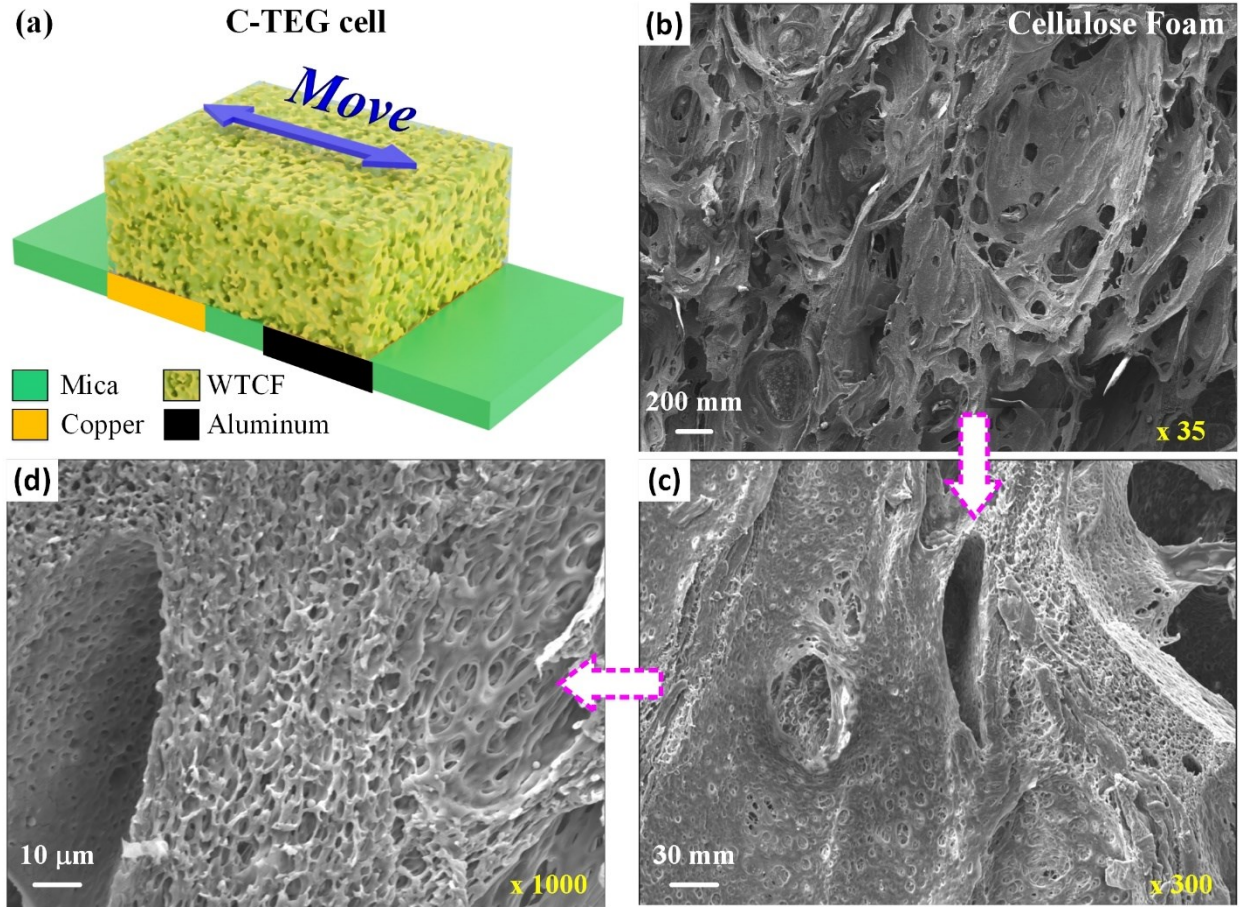
Figure 2.2: (a) Schematic diagram of the C-TEG. FE-SEM images of cellulose foam show (b) macropores, (c) micropores on the wall of macropores, and (d) nanopores on the wall of micropores.
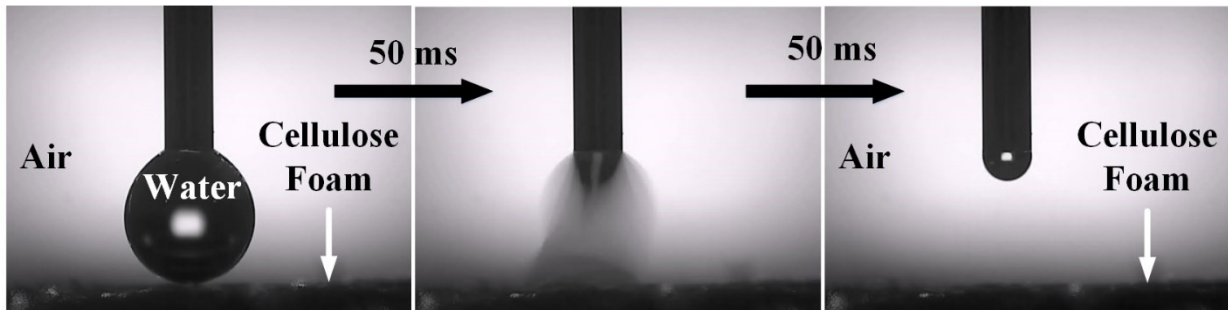
Figure 2.3: Contact angle measurement of the cellulose foam.

The reaction between cellulose and water molecules creates a single electrostatic potential field that can combine two reactive species into one reactive entity and turn the free water into immobilized water on the surface of cellulose. In addition, it is important to highlight the great potential of polymers carrying amine and hydroxyl groups in the development of triboelectric-positive materials [235], and these polymers exhibit a remarkable affinity for water absorption [236]. As cellulose contains plentiful hydroxyl groups that have a strong electron donation capacity, the cellulose with water fixed on the surface could participate in CE as a high electropositivity material. This can be clarified by analyzing the elemental composition and chemical states of cellulose.

The Fourier-transform infrared (FT-IR) spectroscopy of the cellulose foam under both dry and wet conditions, as shown in **Figure 2.4a**, reveals indications of intermolecular hydrogen bonding within the cellulose structure. Particularly notable is the presence of surface-OH participating in hydrogen bonds, typically observable within the wavenumber range of 3455–3410 cm^{-1} [237]. The peak at 1540 cm^{-1} can be attributed to the C-N-H vibrations of the amine group [238]. Further distinctive peaks in the FT-IR spectrum encompass -N=C=O stretching (at 2340 cm^{-1}) [239], C=O stretching (at 1727 cm^{-1}) [240], -OH in-plane bending (at 1330 cm^{-1}) [241], and -C-O-C pyranose ring vibration (at 1050 cm^{-1}) [242].
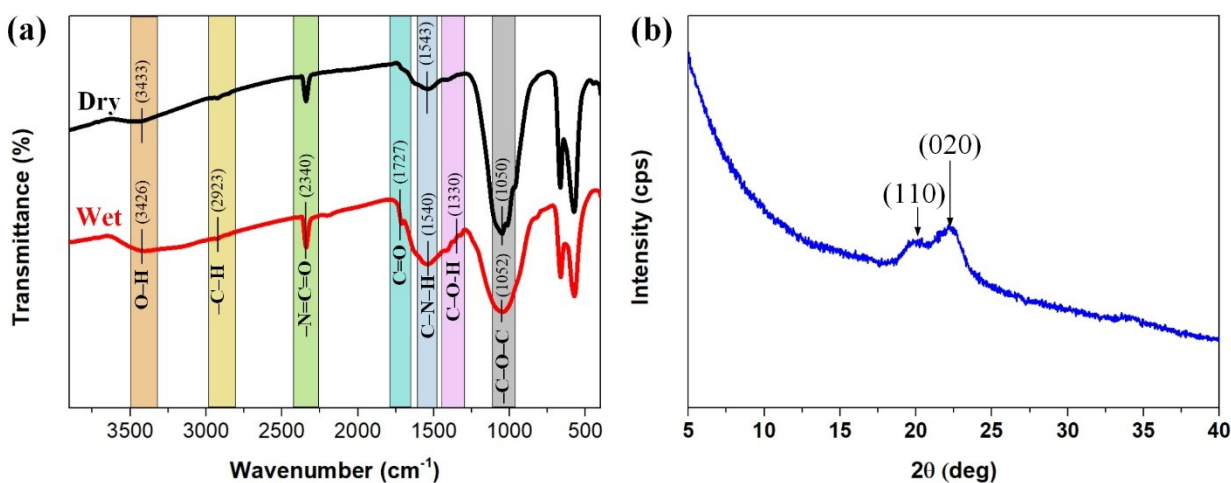
Figure 2.4: (a) FT-IR spectra of dry and wet cellulose foam. (b) XRD patterns of cellulose foam.

Additionally, the XRD pattern of the cellulose foam is depicted in **Figure 2.4b**. A CuKα X-ray source with a voltage of 45 kV and a current of 45 mA was used to record the diffraction patterns.

The main diffraction peaks appear at 2θ = 20° and 22.1°, corresponding to the (110) and (020) crystal planes, respectively, which are supposed to represent the typical cellulose II crystal structure [243, 244]. The peaks corresponding to (110) and (020) are formed by inter- and intra-hydrogen bonding [245], proposing a hydrogen-bonded network in cellulose [237].

3.2. Working mechanism

The working mechanism of the C-TEG relates to the phenomenon of electron transfer that occurs when two metal electrodes are electrically connected, as presented in **Figure 2.5a**. This electron transfer involves the displacement of electrons from the Al electrode to the Cu electrode. This migration process persists until their Fermi levels synchronize. It results in the establishment of a built-in electric field (E_{bi}) and a corresponding voltage (V_{bi}) across the electrodes. The mathematical representation of the V_{bi} is defined by the equation:

$$V_{bi} = (\phi 2 - \phi 1)/e \qquad (2.1)$$

where ϕ signifies the material work function and e represents fundamental unit charge [230-232, 246].

During the phase of stationary contact, referred to as the contacted still state, when the materials remain motionless, an equilibrium state is achieved. In this equilibrium, the E_{bi} prevents any further net charge transfer. Conversely, during dynamic contact phases like sliding, additional charges can be produced due to the conversion of mechanical frictional energy. These charges, denoted as Q_{tri}, originate from triboelectric charges generated by contact electrification during the sliding motion. Under the influence of the E_{bi}, these triboelectric charges experience separation, aligning themselves in one orientation. This phenomenon serves as the primary driving force for generating direct current within the C-TEG. The output current density (Jsc) can be expressed using the equation:

$$J_{SC} = Q_{tri}. \mu. E_{bi} \qquad (2.2)$$

where μ is the mobility of materials [247, 248].
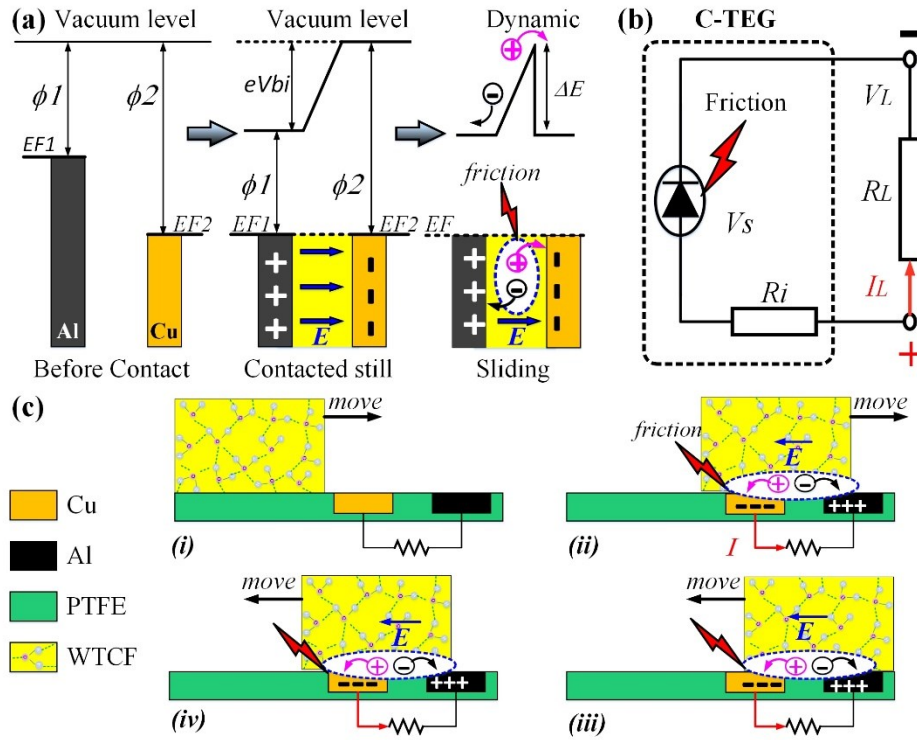
Figure 2.5: (a) Energy band diagrams of Al and Cu before making contact (left), in contact at the contacted steady state (center), and separation charges in a sliding state (right). Here, EF1- $\phi1$ and EF2- $\phi2$ are Fermi levels and work functions of Al and Cu, respectively, Vbi is the built-in voltage, and e is the unit charge. (b) Equivalent circuit of the C-TEG. (c) The working mechanism of the C-TEG.

The step-by-step illustrations in **Figure 2.5c** depict how the C-TEG operates, working in the freestanding mode. At the initial state, the WTCF slides in from the left, the circuit maintains an open state, and no current output is observed (**Figure 2.5c-i**). Upon contact between the WTCF and both Cu and Al electrodes, two electrodes are electrically connected through the conductive path within the WTCF, transforming the original open circuit into a closed circuit (**Figure 2.5c-ii**). It results in creating an electric field E_{bi} between the two electrodes due to their difference in work functions. Since the work function of Cu (~4.7 eV) is higher than that of Al (~4.2 eV) [236], the E_{bi} is directed from the Al electrode towards the Cu electrode. During the sliding motion, friction generates triboelectric charges at the contact interfaces, which subsequently separate under the influence of the E_{bi}, causing positive charges to migrate toward the Cu electrode and negative charges to flow toward the Al electrode via the conductive path within WTCF. It leads to electrons moving unidirectionally from the Al electrode to the Cu electrode through the external circuit,

generating a direct current. The device consistently produces DC outputs while WTCF maintains its movement towards the rightmost position (**Figure 2.5c-iii**) and subsequently reverses its motion backward (**Figure 2.5c-iv).** The process of reverse sliding follows the same principle as shown in **Figure 2.5c-ii**. Once the WTCF separates from the Al electrode and returns to its initial position (Figure **2c-i**), the circuit transitions into an open state, and no current flows in the external circuit. Thereby, the C-TEG exhibits its ability to continuously produce pulsed DC electricity through the periodic sliding of the WTCF.

From a circuit perspective, C-TEG can be modeled as a diode-like voltage source, with a voltage Vs induced through friction across the Cu/WTCF/Al contact interfaces, accompanied by an internal resistance Ri. This configuration results in the production of DC output current I_L and voltage V_L across the external resistance R_L. The corresponding equivalent circuit diagram of C-TEG is illustrated in **Figure 2.5b**.

3.3. Electrical output characteristics

If not mentioned in the following text, a prototype of C-TEG consists of copper and aluminum electrodes (1 cm x 4 cm x 100 µm) located on the surface of a mica substrate with a distance of 5 mm between these two, a cellulose foam (1 cm x 4 cm x 0.5 cm), and DI water. The cellulose foam was driven to move forward and backward at a frequency of ~0.5 Hz.

In order to demonstrate the critical role of the presence of water in generating high-output performance, the comparison of electrical outputs between a control device using a dry cellulose foam and a C-TEG using a wet cellulose foam is investigated. As displayed in **Figure 2.6a-c**, the control device can produce a peak open-circuit voltage (Voc) and short-circuit current (Isc) of about 0.1 V and 18 nA, respectively. Meanwhile, C-TEG with 0.1 mL absorbed water can output 0.54 V and 43.3 µA with DC, which is increased by 5.4 and 2405 times in comparison with the control device, respectively. As the amount of absorbed water increases to 0.4 mL, the value of Isc dramatically increases to 290 µA, corresponding to an output current density (Jsc) of 72.5 µA/cm^2. Thereafter, it increases very slowly and becomes considerably saturated at ~300 µA, which corresponds to a Jsc of 75 µA/cm^2. These results show that the Isc increases with the increase of water absorbency, which proves the key role of the presence of water in the electricity output performance. Indeed, the higher the amount of absorbed water, the more the molecules are fixed

by cellulose through hydrogen bonds, thus increasing the triboelectric charge quantity and then leading to an increase in the electric output [229]. In addition, this is presumably due to the effect of internal resistance on the output current. As mentioned above, when cellulose absorbs water molecules, a conductive path is formed by the hydrogen bond network of water molecules.

Consequently, the increasing amount of absorbed water leads to an increase in hydrogen bonds formed between water molecules and cellulose, then decreasing the internal resistance. In fact, the results shown in **Figure 2.6d** prove that the internal resistance measured between two electrodes decreases with the increase in the amount of absorbed water. The internal resistance measured in the case of a dry cellulose foam is about 1.475 MΩ, which is considerably larger than that in the case of wet cellulose-based devices. This value dramatically decreases from 73 to 50 kΩ when the amount of water absorption increases from 0.1 to 0.4 mL and then remains unchanged as the amount of water absorption increases to 0.6 mL. What is interesting is that the output voltage values of C-TEG are almost constant at ~0.5 V despite the increase of absorbed water, as shown in **Figure 2.6c**. This exhibits different behaviors from the current outputs. This is obviously due to the built-in voltage developed between Cu and Al electrodes when they are connected electrically through the wet cellulose foam. More importantly, C-TEG outputs only positive peaks for both current and voltage signals, as shown in **Figure 2.6a-b**, which indicates good direct-current output characteristics.

To confirm the DC output characteristics of the C-TEG, a loading resistance is applied in the external circuit. As plotted in **Figure 2.7a**, the device can produce a peak output current of about 200 μA at a load resistance of 10 Ω. This value is significantly decreased to 33.5 μA when the load resistance is increased to 10 kΩ. This figure demonstrates that all output signals have DC characteristics. **Figure 2.7b** shows the resistance dependence of both the current and power outputs with the load resistance, in which the current drops from 200 to 0.5 μA with the increase of the loading resistance (R) from 10 to 1 MΩ, meanwhile, the power initially rises and reaches a maximum value of 23.3 μW, which corresponds to a power density of 5.8 μW/cm^2, at a loading resistance of 2 kΩ and then decreases with a further increase in the R-value. Here, the maximum instantaneous power (*P*) is calculated by the equation:

$$P = R.i^2 \qquad\qquad (2.3)$$

where *i* is the peak current at the corresponding load resistance R.
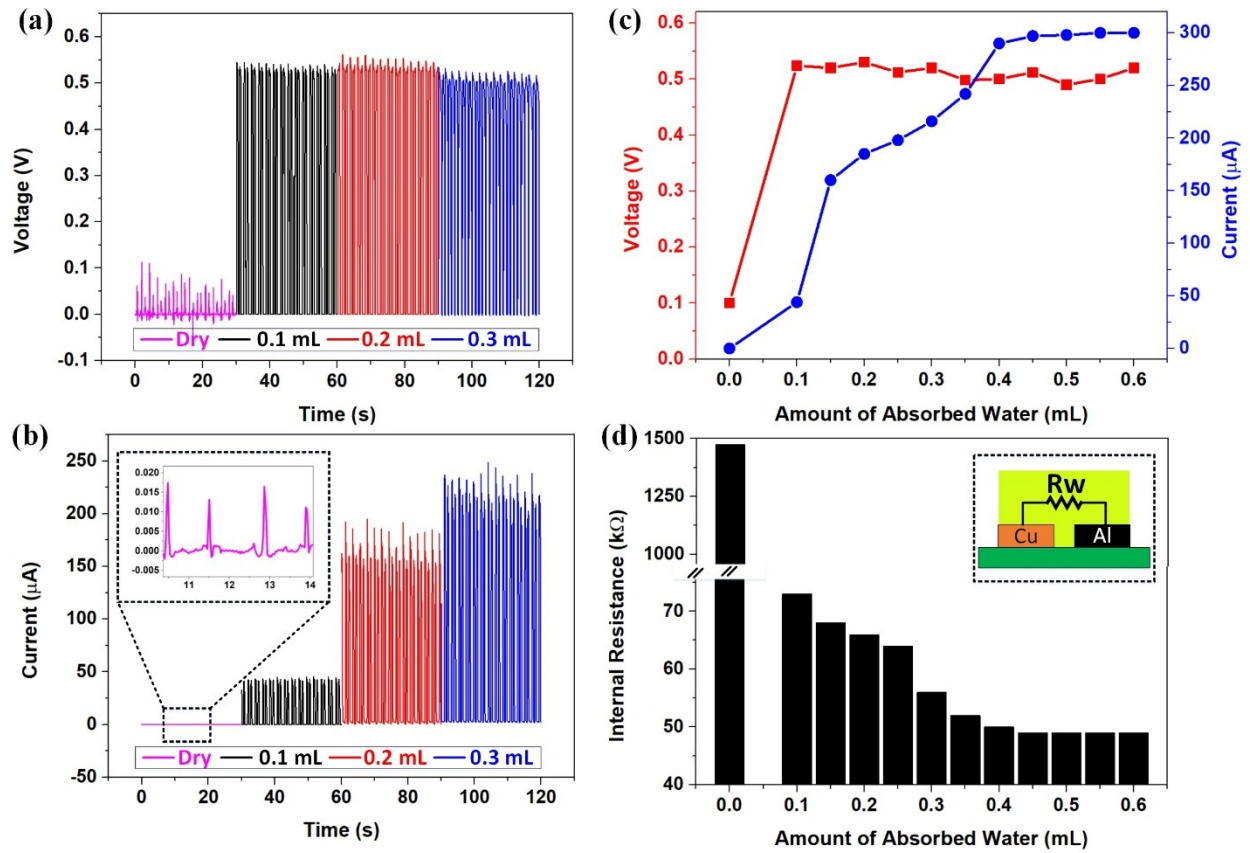
Figure 2.6: (a) Open-circuit voltage and (b) Short-circuit current of the control device (dry-based) and C-TEG with different amounts of absorbed water. (c) Effect of amount of absorbed water on electrical outputs. (d) The change of internal resistance at various amounts of absorbed water.

Additionally, the ability to generate DC outputs enables the C-TEG to directly charge an energy storage unit without requiring a rectifier. To demonstrate this capability, the charging behaviors of the C-TEG across different capacitors (47 to 1000 µF) are explored. **Figure 2.7c** depicts that the device could charge continuously different capacitors and the charging rates show that the lower the value of the capacitor, the faster the voltage will rise. Typically, a capacitor of 47 µF could be charged to 0.45 V at a very fast rate in the beginning, and then slows down reaching a saturated voltage of ~0.47 V. Similar tendencies were also observed in other capacitors. For the same charging voltage of 0.45 V, it took less than 8 s to charge a 47 and 100 µF capacitor, while 470 and 1000 µF capacitors took 20 and 40 s, respectively. The highest stored-energy *Ws* of the capacitor can be calculated by using the formula:

$$Ws = CV^2/2 \tag{2.4}$$

where *C* and *V* are the capacitance and charged voltage across the load capacitor. The *Ws* values of various capacitors after charging for 20 seconds are summarized **in Figure 2.7d.** It is observed that the highest energy stored is obtained at 76.8 µJ in the 1000 µF capacitor, suggesting that the optimal capacitance is 1000 µF.
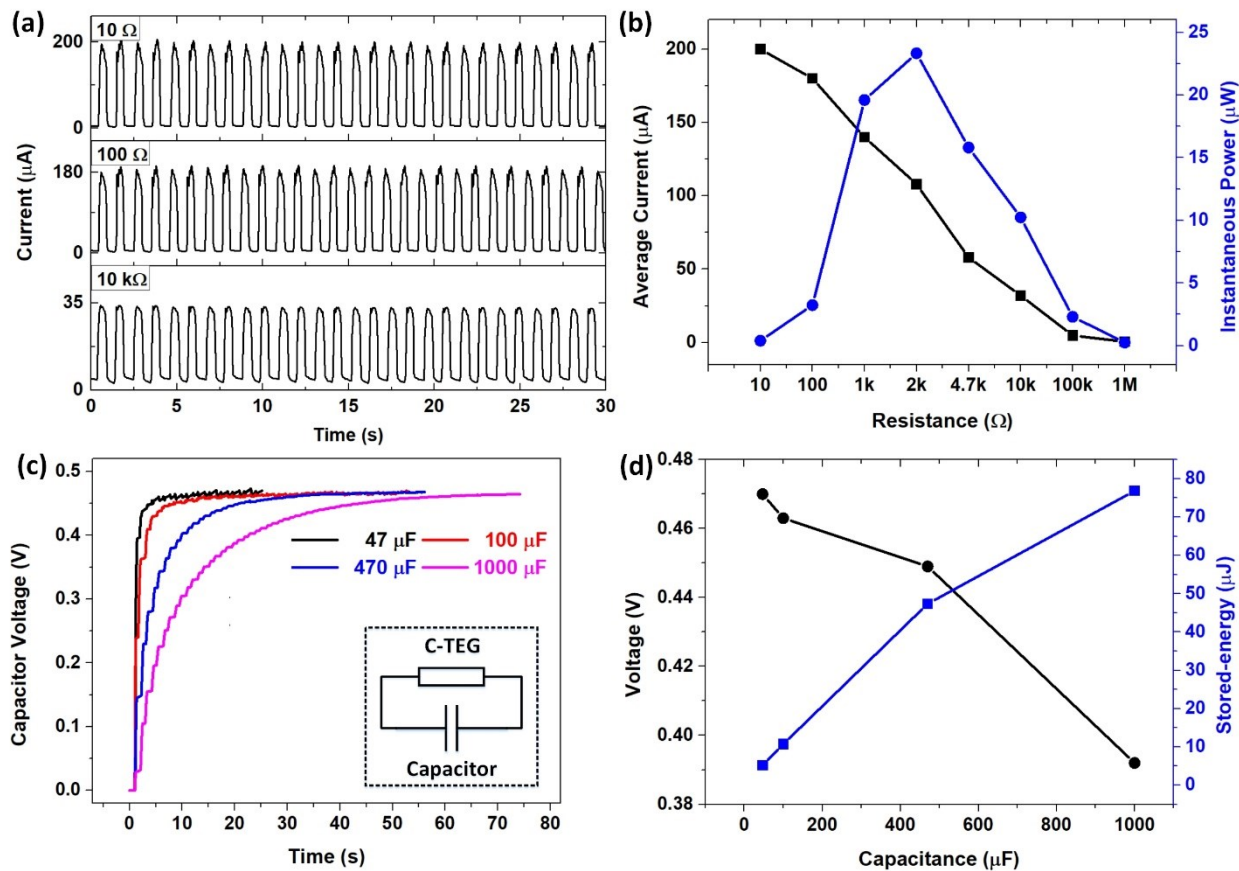
Figure 2.7: (a) The output current of C-TEG at various loading resistances. (b) The change in average current and instantaneous power concerning the loading resistance ranges from 10 Ω to 1 MΩ. (c) Charging behaviors of the C-TEG across different commercial capacitors. (d) Stored-energy Ws after charging various capacitors in 20 seconds.

So far, the role of the triboelectric effect in generating high output performance of C-TEG is considered by measuring the electric outputs of the device when the wet cellulose foam is stationary on the two electrodes (case 1) and comparing it with the electric outputs when the foam slides on the two electrodes (case 2). As depicted in **Figure 2.8a,** C-TEG can generate a continuous electric output of about 0.48 V and 1.5 µA, measured at 0.3 mL of absorbed water. It can be

observed that the peak of voltage outputs in case 1 and case 2 are approximate. However, the peak current output generated by case 2 is much higher than that in case 1, which corresponds to ~150 times. Besides, the total charges transferred correspond to a typical peak of current in case 2 is observed at an approximate value of 94.93 µC, which is 74.7 times higher than that in case 1, calculated with the same time interval of operation, as shown in **Figure 2.8b**. It is clear that triboelectric charges generated by the sliding of the wet cellulose foam contribute to this considerable difference in the electric output of these two case studies. It proves the essential role of the triboelectric effect in the electricity output performance of C-TEG.
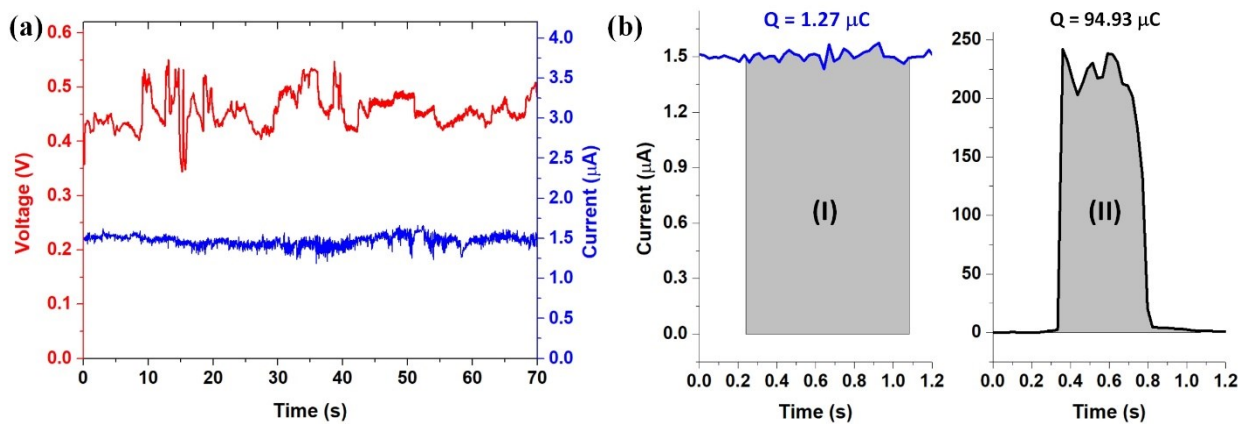
Figure 2.8: (a) The Electrical characteristics of C-TEG when the cellulose sponge is stationary on the two electrodes (case 1). (b) Transferred charges in a time interval of C-TEG in the case the sponge is stationary on the two electrodes (left), and the sponge slides (right).

3.4. Affecting parameters

Impacts of material selection on the output performance

An important aspect to examine is how the properties of the water affect the output performance of the C-TEG. The experiments are realized based on three different types of water, including DI water, tap water, and 0.22 M NaCl solution. **Figure 2.9a** presents the change in the average magnitude of current and voltage outputs of these three study cases. Considering the case using 0.22 M NaCl solution and tap water, C-TEG can generate an instantaneous I_{sc} of 354 and 440 µA, which are approximately 146% and 182% of that generated in the case using DI water, respectively. Meanwhile, the values of V_{oc} in three study cases vary from 0.48 to 0.54 V.

Simultaneously, to characterize the impacts of the selection of electrode pairs on the electrical output performance, Cu, Al, and ITO electrodes are utilized. The work function of ITO is about 5.0 eV based on literature [249, 250]. As mentioned above, the electricity generation of C-TEG is initiated due to the built-in voltage developed between two electrode contacts of different work functions. Therefore, the output performance is strongly influenced by the selection of the electrode pairs, in which the electrode pair with a large difference in work function is expected to generate higher output performance than that generated by the electrode pair with the same material, particularly the output voltage.

Indeed, the experimental results summarized in **Figure 2.9b** show that C-TEG using Cu-Cu and Al-Al electrode pairs produce voltage-current outputs with average peaks of 0.04 V - 2.3 μA and 0.12 V - 0.9 μA, respectively. These values are significantly lower than those generated in the cases using Al-Cu, ITO-Cu, and ITO-Al electrode pairs. Herein, the Al-Cu-based device can produce *Voc* and *Isc* of about 0.63 V and 216 μA, while these values are respectively obtained at 0.3 V - 25.3 μA and 0.9 V - 223 μA in the case of ITO-Cu and ITO-Al-based devices. The highest output performance is obtained in the case using the ITO-Al electrode pair. Obviously, the values of the output voltage are approximate to the value of the built-in voltage, estimated by *Eq. (2.1)*, mentioned in the above discussion. Accordingly, the electrode pairs with a large difference in work functions are desired for generating high outputs.

In the same manner, the impacts of the selected dielectric substrate on the output performance of C-TEG are also considered. **Figure 2.9c** shows the comparison of electrical outputs when using four substrates with different well-known materials in the triboelectric series: (most negative) polytetrafluoroethylene (PTFE), polyvinylidene fluoride (PVDF), mica, and nylon (most positive). From this figure, the peak output voltages generated in four study cases remain almost the same value with a difference of about 7% (~40 mV). The highest peak voltage is obtained at 0.6 V by using the PTFE and PVDF substrates. Meanwhile, the output currents show a considerable difference between the four substrates. The results show that the PTFE substrate can produce the highest output current with an average peak current of 314 μA. Meanwhile, the nylon substrate exhibits the lowest output current in comparison with those produced by other substrates with a peak current of 197 μA. The difference between the highest and lowest values of the current output in this study is about 60%. Interestingly, the ordering of the maximum current output matches well

with the triboelectric ordering between the materials of these substrates. In other words, the more negative triboelectric material could exhibit a higher output current.
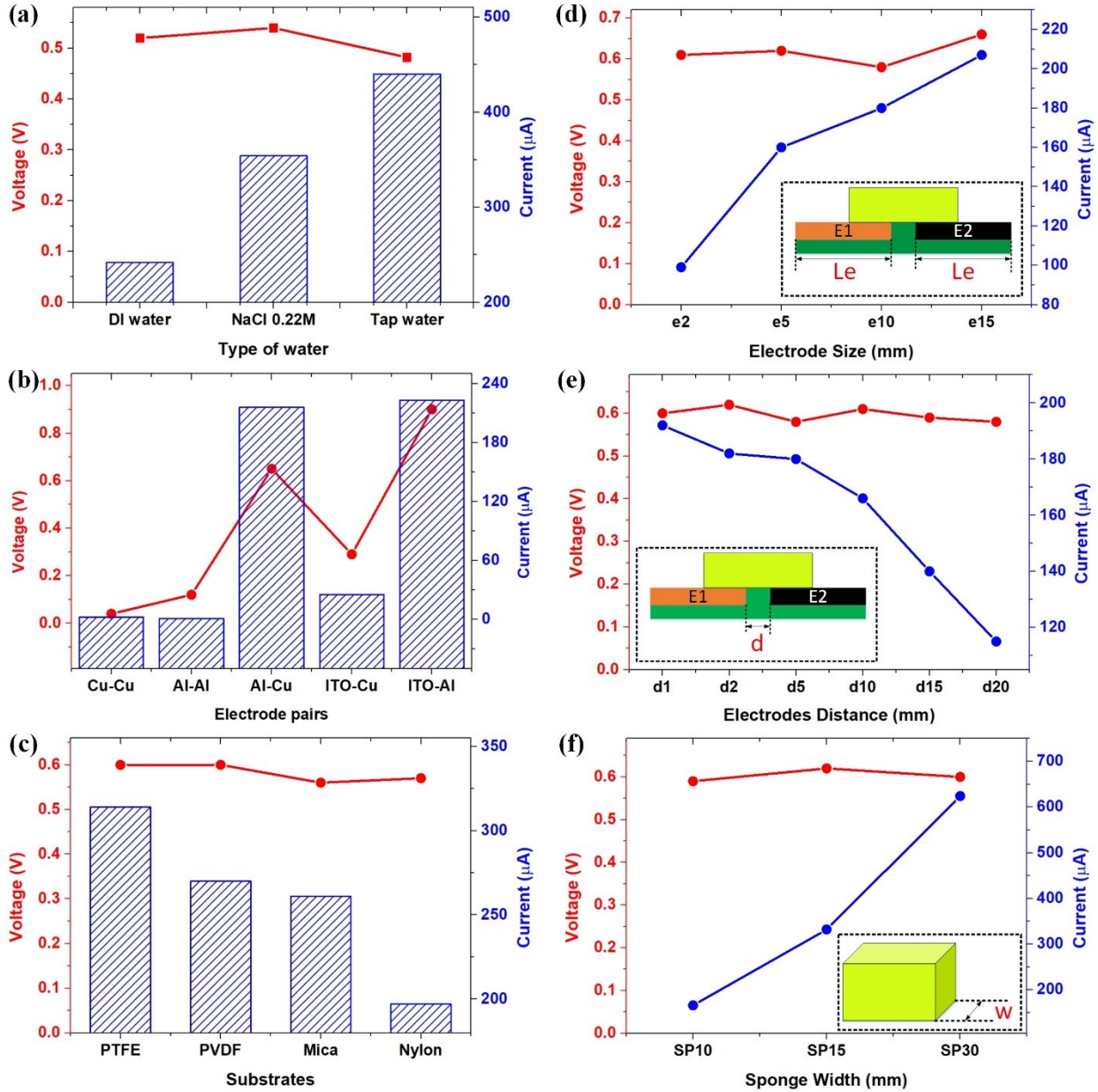
Figure 2.9: Dependence of output performance on materials selection: (a) water properties, (b) pairs of electrodes, (c) materials of substrates. Dependence of output performance on design structure: (d) electrode sizes; (e) distance between two electrodes; (f) cellulose foam sizes. Le is the width of the electrode, d is the distance between two electrodes, and w is the width of the cellulose foam.

Impacts of structure design on the output performance

To further optimize the output performance of this device, the effects of the design structure parameters are investigated, including the size of electrodes (width: Le), the distance between electrodes (d), and the size of the cellulose foam (sponge width: w). The detailed definitions and results are demonstrated in **Figures 2.9d-f**. First, the output current exhibits an upward trend from 99 to 207 µA, corresponding to an increment of 109 %, when the value of Le of electrodes increases from 2 to 15 mm while keeping d at 5 mm and w at 1 cm (**Figure 2.9d**). Similarly, when the width of the foam (w) increases from 10 to 30 mm, the output current increases from 166 to 624 µA, indicating an increment of 276 % (**Figure 2.9f**). The reason for this increasing trend could be related to the enhancement in the effective contact area of the cellulose foam and electrodes, in which the bigger size of electrodes and foam leads to a larger contact area, thus, resulting in a higher output current. On the other hand, by changing the distance d between electrodes, the output currents show an opposite trend in comparison with the above study cases. The results shown in **Figure 2.9e** reflect that the output current decreases with the increasing distance between electrodes and reaches the maximum value of 192 µA at $d = 1$ mm, measured with $Le = 1$ cm and $w = 1$ cm. In addition, as mentioned above, the output voltage of C-TEG mainly depends on the difference in the material work function of the two electrodes, here are Al and Cu. Therefore, the output voltages shown in **Figure 2.9d-f** remain almost unchanged at around 0.6 V.

It can be concluded that changing one parameter while keeping other parameters the same only changes the output currents to a certain extent but has little effect on the output voltage. The output voltage only depends on the material of the electrode pairs. The output performance of C-TEG could be enhanced by selecting a dielectric substrate based on a high electronegative material, ion-containing water, and electrode pairs with a large difference in work functions. Furthermore, the output performance could be also enhanced by increasing the size of the electrodes and the foam or reducing the distance between the two electrodes.

3.5. Applications

In comparison with various cellulose-based nanogenerators [220, 221, 223, 224, 251-255] and various DC mechanical energy harvesters [106, 107, 109, 256-260] reported by previous studies, this device shows a much higher current output, as shown in **Tables 2.1** and **2.2**, respectively.

Table 2.1: Peak voltage and current outputs of various cellulose-based nanogenerators

Types	Active layer	Size	Peak voltage (V)	Peak current (µA)	Refs
Piezoelectric	C/PDMS/AuNPs	3.5 cm x 8.5 cm	6	0.7	[251]
	CMC/PDMS/CNT	3.3 cm x 2.5 cm x 2 mm	30	0.5	[255]
	Cellulose/SbSI	1 cm x 1 cm x 50 µm	0.024	0.020	[253]
	TOCN/PDMS	1 cm x 2 cm x 0.48 µm	60	10.1	[254]
	MoS2/PVDF	3 cm x 3 cm	50	0.03	[252]
Triboelectric	Treated wood	4.5 cm x 4.5 cm	81	1.8	[220]
	PCL/GO	4 cm x 4 cm	120	4	[221]
	Ppy-MWCNT	6.25 cm^2	196.8	31.5	[223]
	CA/PEI/LTV	5 cm x 5 cm	478	157	[224]
Our generator	Cellulose/Water/Al/Cu	1 cm x 4 cm	~0.5	300	This work

Table 2.2: Peak voltage and current outputs of various DC mechanical energy harvesters

Types	Active layer	Size	Peak voltage (V)	Peak current (µA)	Refs
Piezoelectric	ZnO nanowire array	~2 mm^2	1 mV	$1.5.10^{-4}$	[260]
	ZnO nanowire-nanowall	3.14 mm^2	20 mV	15.7	[259]
	ZnO nanosheets-anionic layer heterojunction	-	0.75	16 µA/cm^2	[258]
	ZnO nanosheets/Zn:Al layered double hydroxide layer	6 mm^2	0.38	1.3	[256]
Triboelectric	PA/nylon-66	6.8 cm x 7 cm	4500 V	40	[107]
	FEP/Cu/Steel/Acrylic/ABS	7.5 cm x 7 cm	149.5	21.6	[106]
	PTFE/Al/Rubber	Rubber belt with 2 cm in width	3200	370	[257]
	PTFE/Acrylic	10 cm^2	33	65	[109]
Our generator	Cellulose/Water/Al/Cu	1 cm x 4 cm	~0.5	300	This work

In regard to enhancing the instantaneous current and voltage outputs, multiple unit cells of C-TEG could be connected in series or parallel configurations and then synchronize their outputs. Substantially, **Figure 2.10a-b** proves that four cells connecting in parallel could produce a peak output current of about 2 mA, while the output voltage can obtain a value of approximately 2 V when connecting four cells in series, respectively. This declares a promising potential to run a device for various practical applications.

More interestingly, C-TEG not only provides a mechanical-to-electrical conversion concept but also demonstrates the potential application as a self-powered sensor based on ion concentration dependency. To validate the sensing capability of the device, NaCl solutions with various concentrations are utilized. The real-time electrical responses are reported in **Figure 2.11**, which exhibits a monotonic increase trend of the output current with increasing the ion concentration in the range of 0 to 0.8 M (mol/L). This type of increasing tendency of the output current shows linearity, as depicted in **Figure 2.12a,** and thus can be fitted with a simple linear function

$$y = K1.x + K2 \tag{2.5}$$

where *y* represents the output current value, *x* is the input ion concentration, *K1* is sensitivity, and *K2* is the intercept. The linear regression analysis shows a high sensitivity K1 of about 589.02 $\mu A/M$ and a linearity R^2 = 0.996, which proves a great accuracy and potential application for measuring the ion concentration of NaCl solution.
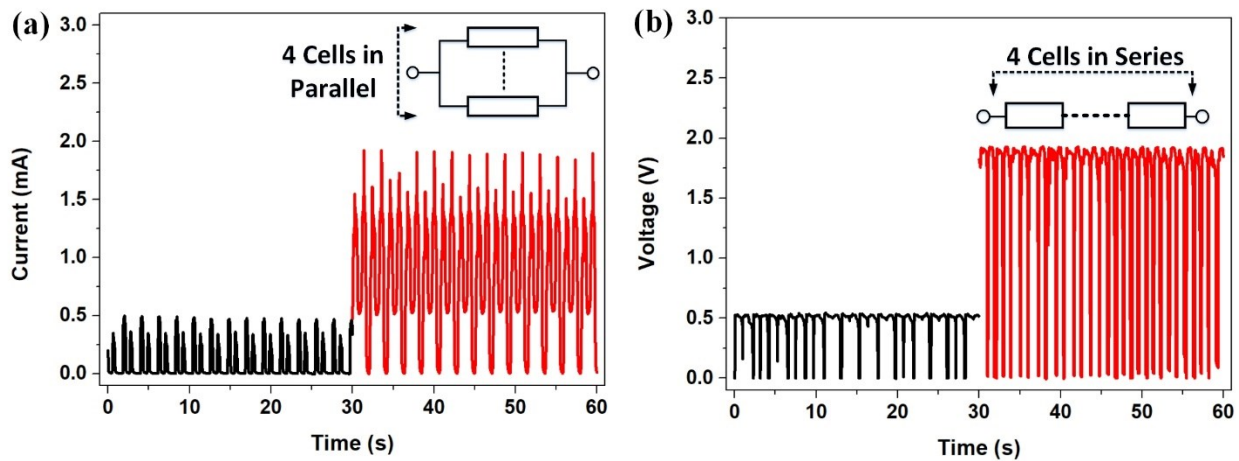
Figure 2.10: Demonstration of application of C-TEG. (a) Enhancing instantaneous current by connecting four unit cells in parallel. (b) Enhancing instantaneous voltage by connecting four unit cells in series.
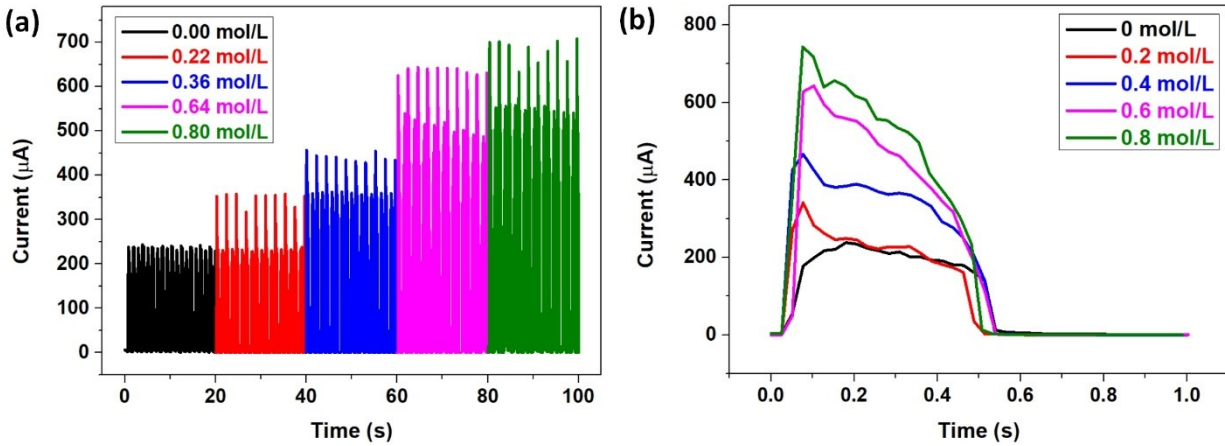
Figure 2.11: The effect of ion concentration of NaCl solution on the output current of C-TEG. (a) Real-time output current signals at various ion concentrations. (b) Enlarges view of typical output current-time curve.

Remarkably, the ability to generate DC outputs enables this device to directly charge the capacitor without requiring any rectifier. Accordingly, four cells in series can directly charge a 1 mF capacitor to 1.5 V within 140 s without requiring any rectifier **(Figure 2.12b),** corresponding to the stored energy of about 1.125 mJ, which is sufficiently high for directly powering many electronic devices. This result declares the potential application of C-TEG as a power source in self-powered systems.
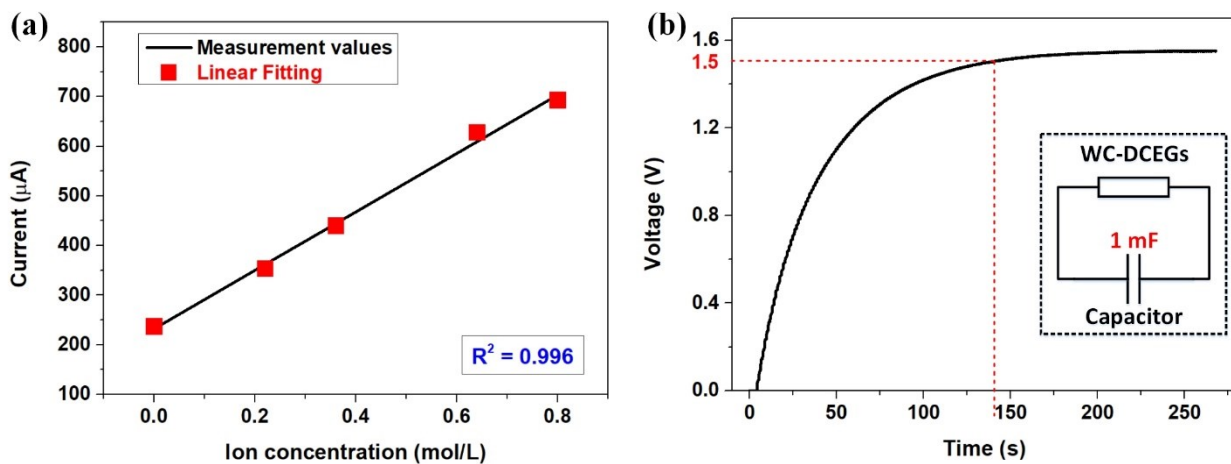
Figure 2.12: (a) Linear regression analysis between the output current and the ion concentration of NaCl solution. (b) The charging behavior of a 1 mF capacitor by four unit cells connecting in series. Measured at a cellulose foam (30 mm in width) wetted with 0.9 mL DI water, and Al/Cu electrodes (width: 1 cm, distance: 1 cm).

4. Conclusion

In conclusion, this study has successfully demonstrated a cellulose-based triboelectric generator (C-TEG) as a mechanical energy harvester, utilizing the combined effect of sliding contact electrification and direct charge transfer between two metal contacts with different work functions. The presence of absorbed water on the cellulose foam plays a pivotal role in achieving high-output performance. The research systematically investigated the impacts of the structural parameters and material selection on the output performance of C-TEG.

The results reveal that the output voltage depends solely on the electrode pair materials, while the output current is significantly influenced by the effective contact area and the properties of the triboelectric materials. The device is capable of producing DC power, with a maximum instantaneous current density of 75 µA/cm^2 and an induced voltage of approximately 0.48–0.90 V. Moreover, the potential for increasing the maximum output voltage and current is evident by connecting multiple C-TEG cells in series or parallel, indicating its significant potential for mechanical energy harvesting applications.

Furthermore, the linear relationship observed between the output current and the ion concentration of a NaCl solution suggests the utility of C-TEG in ion concentration sensing, with a detection sensitivity of about 589.02 µA/M. This implies promising prospects for self-powered sensor fabrication. In summary, the findings open up opportunities for the development of self-powered sensors that rely on the electrical output's dependence on various input stimuli, making C-TEG a viable and efficient strategy in the field of energy harvesting and self-powered sensing.

CHAPTER III – CELLULOSE-BASED TRIBOELECTRIC SELF-POWERED MULTIFUNCTIONAL SENSOR

Self-powered sensing systems are a crucial component in the field of the Internet of Things (IoT). Despite the development in sensor technologies, significant challenges persist in a single function and relying on batteries as their external power supply. This study introduces the cellulose-based triboelectric self-powered multifunctional sensor (C-TSMS). This device generates DC outputs via sliding contact electrification of a water-treated cellulose foam and direct charge transfer across two metal contacts. C-TSMS successfully achieved the integration of mechanical energy harvesting and multifunctional sensing demonstrating a promising self-powered multifunctional sensing capability. C-TSMS establishes robust linear relationships between the output current density and diverse stimuli like pressures, sliding velocities, water absorption, and ion concentrations. Remarkably, correlation coefficients consistently exceed 0.99, validating precision and linearity. For self-powered operation, C-TSMS achieves a peak current density of 340 $\mu A/cm^2$ and 0.5 V voltage. To boost the output voltage, series-connecting four C-TSMS cells can produce a peak voltage of 2 V. The generated energy is stored in a capacitor and successfully powers a commercial calculator, offering an opportunity for external power source elimination. Overall, C-TSMS presents innovative mechanical energy harvesting and self-powered multifunctional sensing, with significant potential.

1. Introduction

In recent years, sensors have demonstrated immense potential across diverse domains, including human-machine interaction, health monitoring, and the Internet of Things (IoT) [261]. These devices play an important role as crucial components, enabling the collection of external information from environments or objects, with particular significance in the field of IoT [262]. Despite the advancements in sensor technology, conventional sensors remain limited by their single-sensing functionality. Addressing this limitation requires combining various sensing mechanisms and the utilization of complex structures and manufacturing techniques to attain multifunctional sensing capabilities [110]. Therefore, developing a sustainable multifunctional sensor with the capacity to detect and distinguish multiple parameters coupled with simplicity in manufacturing is necessary. Besides the essential aspect of multifunctionality, the power supply

emerges as another fundamental requirement that demands serious consideration. Conventional sensors rely on batteries for their power source, posing a significant obstacle to achieving comprehensive flexibility [1]. This creates a need for self-powered systems capable of detecting external information without relying on external power sources.

To overcome these challenges, the concept of self-powered sensing technology arises as a viable solution that has garnered notable interest from the scientific community. A self-powered sensing system can be established by harmoniously integrating two primary components, including the active sensor module and energy harvesting units, into a unified framework. The system utilizes its electrical output signal, frequently presented as voltage or current outputs, as the sensing signal. Simultaneously, it harnesses ambient energy from the surrounding environments to supply power to the sensor module, enabling it to maintain regular functionality without relying on an external power supply [263]. Remarkably, most small electronics operate at low power levels, ranging from microwatts to milliwatts, making energy-harvesting methods a viable option for driving these devices [2].

Over the past few decades, converting mechanical energy into electricity has been an important approach widely employed for generating power among various ways to harvest energy [264]. Mechanical energy exists everywhere, including body human motions, vibrations, raindrops, water flow, ocean waves, wind, etc. These energies have been harnessed to produce electrical power using electromagnetic induction, piezoelectricity, pyroelectricity, and more recently, triboelectric technology. Notably, the triboelectric nanogenerator (TENG) introduced by Zhongling Wang et al. [134], has proven to be a potential technique for harvesting small mechanical energy and enabling self-powered sensing mechanisms due to its advantages of simple structure and high energy density [265-267]. This innovative device generates electrical output through contact electrification and electrostatic induction, which provides sufficient energy to power electronics. By analyzing the relationship between exerted stimuli inputs and electrical output signals, TENG can be utilized as a sensing device. Up to now, different TENG-based self-powered sensors have been developed to monitor different variables, such as pressure sensing [268], motion detection [110], humidity assessment [236], temperature measurement [269], ion concentration detection [270, 271], and chemical recognition [272]. Furthermore, TENG-based multifunctional sensors have been successfully realized. For instance, Den et al. [273] reported a super-stretchable multi-

sensing TENG that can detect strain gauge and dynamic motions of human body joints. Similarly, Wu et al. [274] developed a self-powered multifunctional sensor that is capable of detecting acceleration, force, and rotational parameters.

On another aspect, researchers are exploring functional materials to create highly sensitive multifunctional sensors, with a notable emphasis on cellulose foam [275]. This material has gained attention due to its impressive mechanical properties, encompassing attributes such as high porosity, compressibility, and a large specific surface area [219]. These characteristics render it particularly suitable for applications in physical sensing [224]. The abundance of hydroxyl and amine groups within cellulose enables robust capacity for electron donation, thus rendering it exceptionally compatible with the triboelectric effect [235]. Furthermore, cellulose's hydrophilic nature facilitates its interaction with water. When in contact with water, hydrogen bonds spontaneously form between the hydroxyl groups of cellulose and water molecules, resulting in water molecules fixing to the surface creating a conductive path within treated cellulose [225, 227, 228]. These unique properties of cellulose present a significantly factor for exploration in the advancement of self-powered sensing technology utilizing the triboelectric effect.

This chapter introduces a cellulose-based triboelectric self-powered multifunctional sensor (C-TSMS). The C-TSMS operates by generating electrical outputs through sliding contact electrification of a cellulose foam treated by water (the sliding element), combined with direct charge transfer across two metal contacts with different work functions. As the sliding element moves, friction generates triboelectric charges, which are then unidirectionally separated due to the influence of the built-in electric field resulting from the electrical connection of two metal contacts. Thereby, DC generation is achieved via the external circuit. The study systematically explores various physical and chemical stimuli, including pressures, sliding velocities, water absorptions within cellulose foam, and ion concentrations in water. By analyzing the correlation between the output current density and the corresponding exerted stimuli, the multifunctional sensing capability of C-TSMS is demonstrated. The experimental results exhibit strong linearity with high correlation coefficients exceeding 0.99, confirming their accuracy. Moreover, C-TSMS achieves a high current density of 340 μA/cm^2 but a relatively low voltage of 0.5 V. To boost the output voltage, four C-TSMS cells are connected in a series configuration, resulting in producing a peak voltage of 2 V. The generated energy is stored in a capacitor and successfully powers a

commercial calculator, offering an opportunity to eliminate the need for external power sources in self-powered sensing mechanism. Overall, these findings highlight the significant potential of the C-TSMS as an innovative approach for mechanical energy harvesting and self-powered multifunctional sensing.

2. Experimental section

2.1. Materials

Aluminum and copper tapes were purchased from Ducksung Hitech (Seoul, South Korea) for use as electrode materials. Cellulose foam was obtained from Hankook Tamina (Hanam, South Korea) and served as the active material. Distilled water and NaCl solution were provided by our research laboratory for subsequent experimental procedures. A polytetrafluoroethylene film with a thickness of 100 μm was sourced from Sigma-Aldrich (St. Louis, MO, USA) and utilized as the substrate for electrode attachment. Capacitors were bought from Rubycon (Nagato, Japan).

2.2. Fabrication of the C-TSMS

Rectangular pieces of Cu and Al tapes with dimensions of 1 cm x 2 cm were prepared and employed as the sensor's electrodes. An 8 cm x 8 cm PTFE film was utilized as the substrate onto which the Cu and Al electrodes were affixed. The electrodes were oriented in a parallel configuration, with a separation distance of approximately 5 mm. The water-treated cellulose foam (WTCF) was fabricated by absorbing water/NaCl solution into a cellulose foam (0.107 g/cm^3 - density). The treated foam was attached to a movable substrate. The movement of the sliding element was achieved through a slider-crank mechanism, allowing the C-TSMS to operate autonomously. To assess sensor performance, a range of load resistances (100 Ω to 2 MΩ) and capacitances (47 to 1000 μF) were integrated into the external circuit.

2.3. Characterization and Measurement

The electrical response characteristics were evaluated using a Keithley Instruments, Inc. multimeter model DMM7510 (Cleveland, OH, USA). The surface morphology of the cellulose foam was examined using a JEOL Field Emission Scanning Electron Microscopes (FE-SEM) model JSM-7600F (Tokyo, Japan).

2.4. Method

To comprehensively assess the C-TSMS's performance, an in-depth investigation of various operational parameters was conducted. Parameters including water absorption within cellulose foam, ion concentration of NaCl solution, sliding velocity, and vertical pressure were systematically varied. Analysis of the device's output performance, primarily through observing the generated output current, allowed the corresponding chemical and physical factors to be monitored. The electrical energy produced by the C-TSMS was also explored for its potential application in powering electronic devices, highlighting the multifunctional self-powered sensing capabilities of the device.

3. Results and discussions

3.1. Working mechanism and electrical responses

The structure design of the C-TSMS is the same as the C-TEG presented in *Chapter II*. **Figure 3.1a** illustrates the three-dimensional representation of the C-TSMS, showcasing the parallel alignment of Cu and Al electrodes. This arrangement allows the effective collection of triboelectricity generated by the motion of a water-treated cellulose foam (WTCF) across the surfaces of the PTFE film and electrodes. The experimental setup is illustrated in **Figure 3.1b**, which consists of a slider-crank mechanism to simulate the reciprocating motion of the WTCF, a C-TSMS cell, and the measurement equipment.

The step-by-step illustrations in **Figure 3.2** depict how the C-TSMS operates. Energy conversion within the C-TSMS involved three-step processes: (1) Charges are produced through frictional energy during the reciprocal sliding motion of the treated foam; (2) The built-in electric field between the Cu and Al electrodes separates the generated charges; and (3) Separated charges flow through the conductive path within the WTCF, resulting in generating DC outputs in external circuits, as shown in **Figure 3.2**. Briefly, the operation of C-TEG can be outlined within two primary states. Initially, in the absence of contact between the WTCF and both Cu and Al electrodes, there is no electric output observed (**Figure 3.2-i**). Subsequently, in the second state, when the WTCF establishes contact with both electrodes, the generation of direct current becomes attainable (**Figure 3.2-ii-iv**).
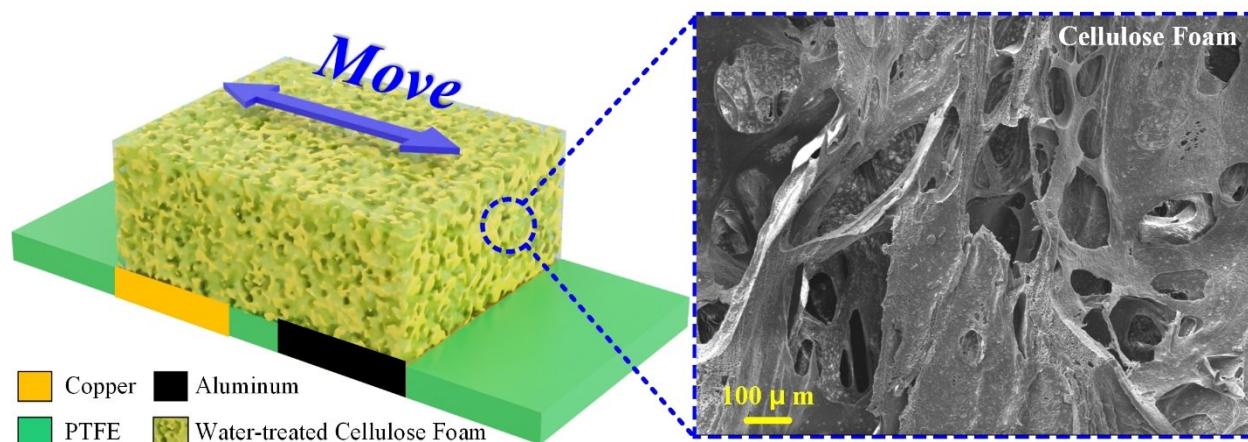
Figure 3.1: (a) Schematic diagram of the C-TSMS. The inset image: foam-like morphology of the cellulose foam. (b) Schematic diagram of the experimental setup.
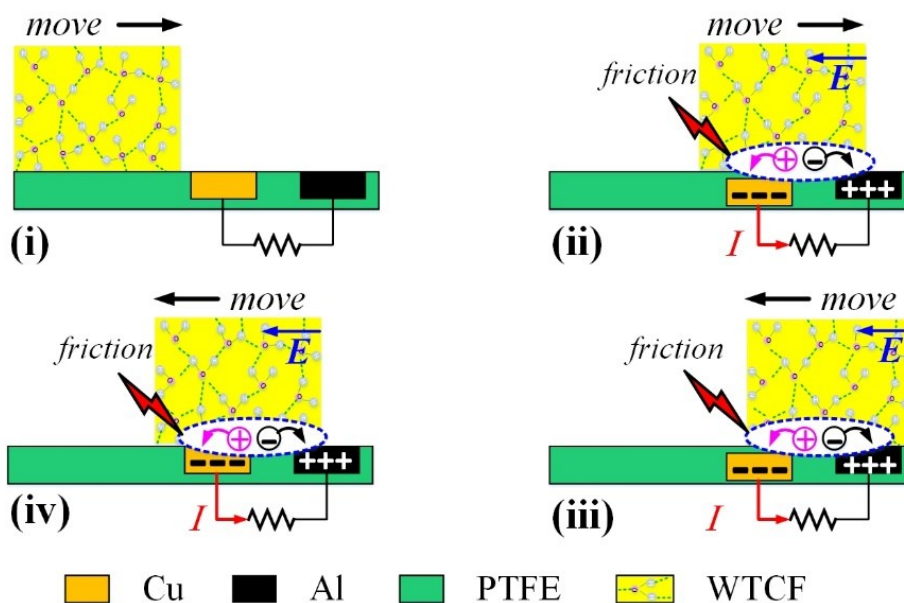
Figure 3.2: The working mechanism of the C-TSMS.

To evaluate the output performance of the C-TSMS, we developed a water-treated cellulose foam. This treated foam was created by utilizing cellulose foam (~0.43 g in mass) to absorb 0.9 mL of distilled water, resulting in water absorption of 2.11 g/g. Subsequently, we set the treated foam into a reciprocating motion across the PTFE and electrode surfaces at a velocity of 3 cm/s. The illustration of the experimental setup is shown in **Figure 3.3**, which consists of a slider-crank mechanism to simulate the reciprocating motion of the WTCF, a C-TSMS cell, and the measurement equipment.
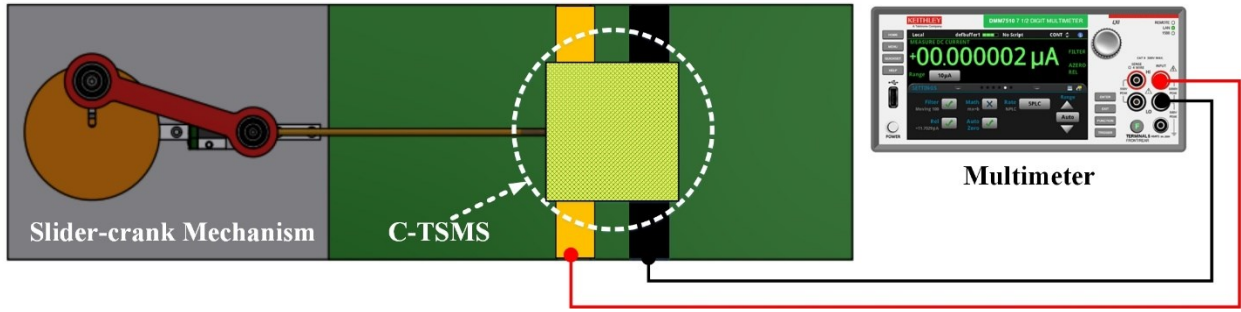
Figure 3.3: The experimental setup of the C-TSMS.

We assessed the open-circuit voltage output (*Voc*) and depicted the experimental results in **Figure 3.4a**. Clearly, the C-TSMS exhibited the ability to generate a continuous DC voltage characterized by positive pulses. These pulses collectively attain an average peak value of approximately 0.5 V. Notably, this value closely aligns with the calculated built-in voltage $V_{Cu\text{-}Al}$, as determined by **Eq. (2.1).** Additionally, we conducted measurements of the output current under the short-circuit condition, and from there, computed and graphed the corresponding current density (*Jsc*) in **Figure 3.4b**. Impressively, the device achieved a peak current density of approximately 94 $\mu A/cm^2$. The inset images provide magnified insight into the typical voltage and current peaks characteristic of an ideal operational cycle. These images clarify the consistency between the measured data and the theoretically predicted DC behavior.
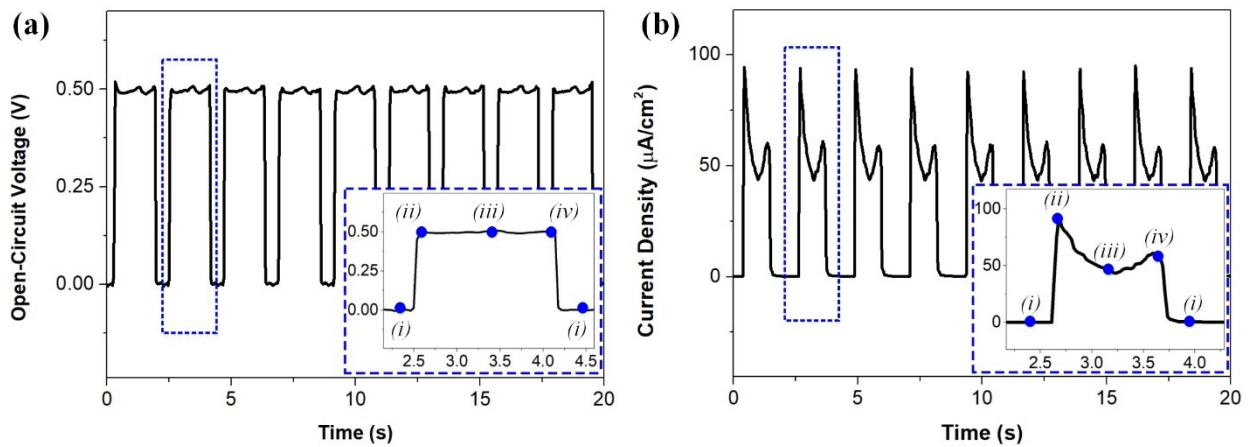
Figure 3.4: Electrical responses of the C-TSMS: (a) Open-circuit voltage and (b) Short-circuit current density. Inset images: Magnified views of output signals during an ideal operating cycle.

To confirm the DC characteristics, we conducted an investigation into the electrical responses of the C-TSMS using a range of load resistances and capacitances. The corresponding electric

69

circuits can be found in **Figure 3.5**. As depicted in **Figure 3.6a**, the electric outputs consistently presented themselves as all positive pulses, with the peak values of current density decreasing with increasing load resistance. Remarkably, at a load resistance of 100 Ω, the peak current density attained 70 $\mu A/cm^2$. However, this value significantly dropped to 26.9 $\mu A/cm^2$ at 1 $k\Omega$ and continued to diminish to 5.1 $\mu A/cm^2$ at 10 $k\Omega$. Further increase in load resistance resulted in a noticeable reduction, with the current density reaching 30 nA/cm^2 at a load resistance of 2 $M\Omega$, as depicted in **Figure 3.6b**. This figure also displays the relationship between the output power density and load resistance. According to this relationship, the power density initially increased with increasing load resistance. It reached a maximum value of 6.6 $\mu W/cm^2$ at 510 Ω. However, as the load resistance further increased, the power density started to decrease. Herein, the output power (P) was quantified by using **Eq. (2.3).**
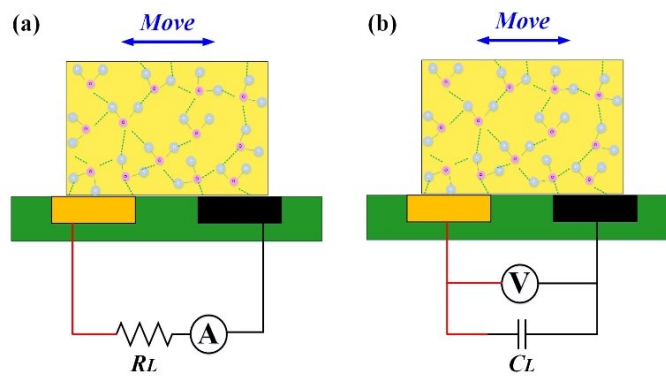
Figure 3.5: Electrical circuit for measuring (a) current outputs at various load resistances RL and (b) voltage at various load capacitances CL.
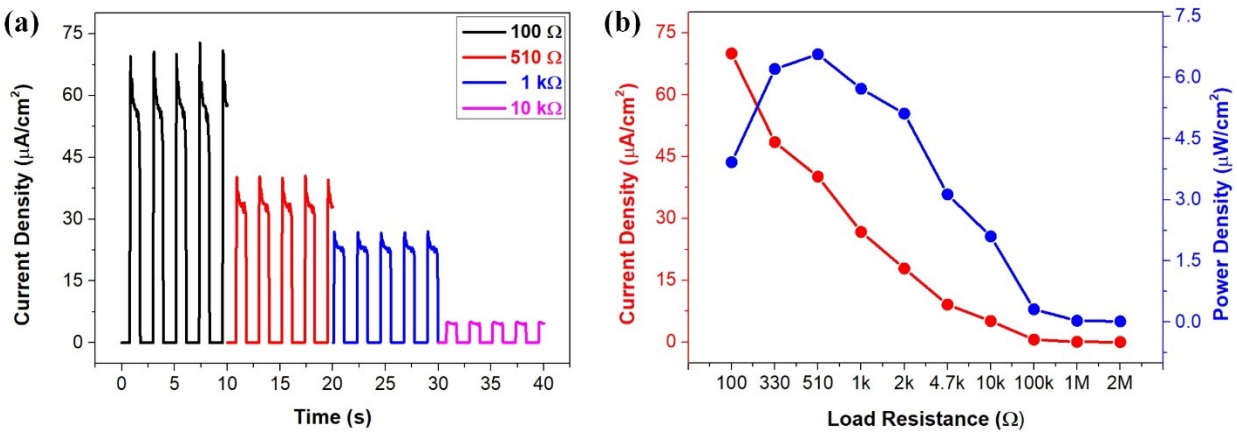
Figure 3.6: (a) Current densities under various load resistances. (b) Dependence of the current density and power density on load resistances.

Simultaneously, the C-TSMS's capacity to generate DC outputs eliminates the need for a rectifier when charging energy storage units. To verify this capability, we examined the charging behavior across varying load capacitances (C_L), including 100, 470, and 1000 µF. The experimental results, detailed in **Figure 3.7a**, reveal similar trends in charging voltage concerning both charging time and distinct load capacitances. In the initial stages, the capacitor is charged rapidly, and then, the charging rate gradually slows down until it reaches a saturated voltage. Interestingly, smaller C_L values require less time to reach saturation compared to larger C_L values. Moreover, **Figure 3.7b** declares that the peak current output of C-TSMS remains stable after approximately 500 seconds of operation, highlighting its reliable output stability.
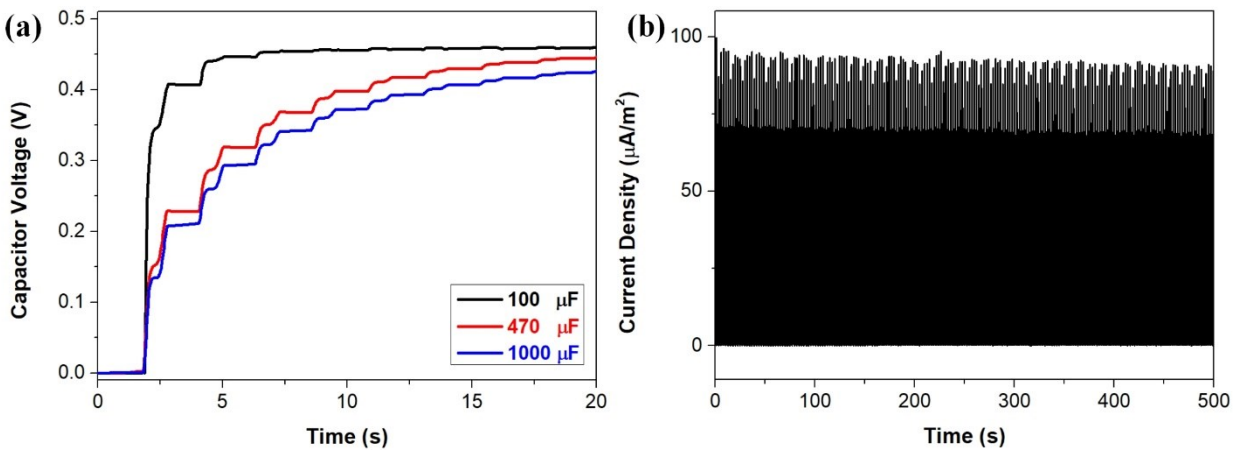
Figure 3.7: (a) Voltage variations of various capacitors charged by the C-TSMS. (b) Stability performance of the C-TSMS's output current.

3.2. Demonstration of multifunctional sensing technology

The multifunctional sensing capability of the C-TSMS was investigated through a comprehensive exploration of its output characteristics under diverse physical and chemical stimuli. By analyzing the resulting electrical responses, primarily by observing the output current, we could effectively monitor the corresponding stimuli exerted on the device. According to the relation implied by *Eq. (2.2),* the current density of the C-TSMS is closely related to the mobility of the active material, the WTCF, and the amount of triboelectric charge generated by friction. The mobility of the WTCF relates to the conductive path formed inside the cellulose foam, which is highly dependent on the amount of absorbed water and the ion concentration of the water,

meanwhile, the friction is affected by the applied pressure and velocity of the slider, as shown in **Figure 3.8a** and **b**, respectively.
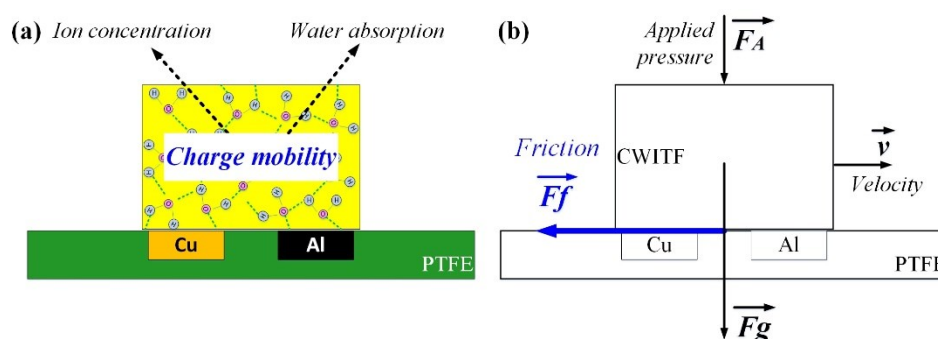
Figure 3.8: Affecting parameters of the (a) material mobility and (b) friction.

To gain insights into the relationship between material mobility and the output current of the C-TSMS, we performed current measurements at carrying levels of water absorption, which determine the amounts of water absorbed within cellulose foam. When the amount of absorbed water changes within the cellulose foam, the mobility of the treated foam will change accordingly. The increased presence of water molecules leads to an increase in the concentration of hydrogen bonds within the cellulose foam, thereby improving the mobility of the hydrogen-bonded network formed by water molecules and cellulose [236, 276, 277]. Consequently, this facilitates the movement of charges through the conducting path within the WTCF, thus enhancing the current output. **Figure 3.9a** plots the dependence of the output current density on the water absorption. As expected, the peak current density increased from 50.6 to 98.8 $\mu A/cm^2$ with a gradual increase in water absorption from 0.23 to 2.34 g/g.

Simultaneously, we examined how the output current varies with the ion concentration in water, using a NaCl solution. As depicted in **Figure 3.9b**, the current density increases drastically from 75.8 to 340 $\mu A/cm^2$ as the ion concentration increases from 0.1 to 1 mol/L (M). In more detail, the peak current density of the C-TSMS using 1 M NaCl solution is approximately 6.8 times higher than that observed with distilled water (0 M). Obviously, increasing the ion concentration in the water substantially contributes to an increase in conductivity within the WTCF. This is attributed to the greater availability of ions to transport charges, eventually improving charge mobility within the WTCF. Therefore, amplified current density finds its explanation in the alternation of ion concentration within the water.
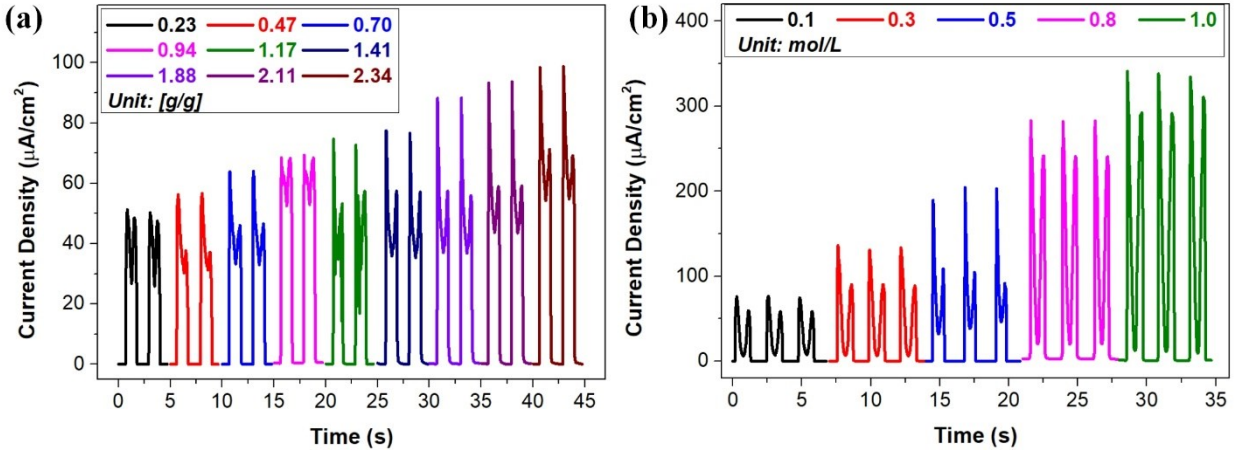
Figure 3.9: Dependence characteristics of the C-TSMS's current density on (a) water absorption of WTCF and (b) ion concentration in water.

It is worth noting that the observed increasing tendency is likely attributed to the impact of the mobility of the WTCF on the current output. Presumably, greater mobility (or low resistivity) corresponds to higher current density. To further validate this, experimental tests were performed to investigate the correlation between the WTCF's internal resistance and both water absorptions and ion concentrations. The results indicated a gradual decrease in internal resistance with increasing water absorption and ion concentration. Refer to **Figure 3.10** for comprehensive details. It is obvious that the internal resistance of WTCF decreased by approximately 17% and 25% when the water absorption increased from 0.23 to 2.34 g/g and the ion concentration in water increased from 0 to 1 M, respectively.

Importantly, alterations in peak current densities exhibit robust linear dependencies on fluctuations in water absorption within the WTCF and ion concentration in water. The fitting curves, illustrated in **Figures 3.11a** and **b**, were derived by effectively fitting the data concerning water absorption, ion concentration, and the corresponding current density data. The fitting curve can be characterized through a linear equation, expressed as:

$$Jsc = K1.x + K2 \tag{3.1}$$

where *Jsc* represents the peak current density, *x* is the independent variable, *K1* is the proportionality constant, and *K2* is the y-intercept. To provide a comprehensive understanding of the C-TSMS's performance characteristics, we defined the sensitivity (*S*) through the equation

73

$$S=\Delta Jsc/\Delta x \qquad (3.2)$$

where ΔJsc signifies the corresponding change in peak current density, and Δx denotes the incremental in relative input. Consequently, the water absorption and ion concentration sensitivities of the C-TSMS were determined to be 22.3 $(\mu A/cm^2)/(g/g)$ and 299.3 $(\mu A/cm^2)/(mol/L)$, respectively. To quantify the strength of the linear relationship, we calculated the coefficient of determination (R^2), which exceeded 0.99. This high R^2 value proves a highly accurate correlation between the C-TSMS's current outputs and the trends in water absorption and ion concentration. This finding suggests that the C-TSMS has remarkable promise in the domains of both water absorption and ion concentration detection.
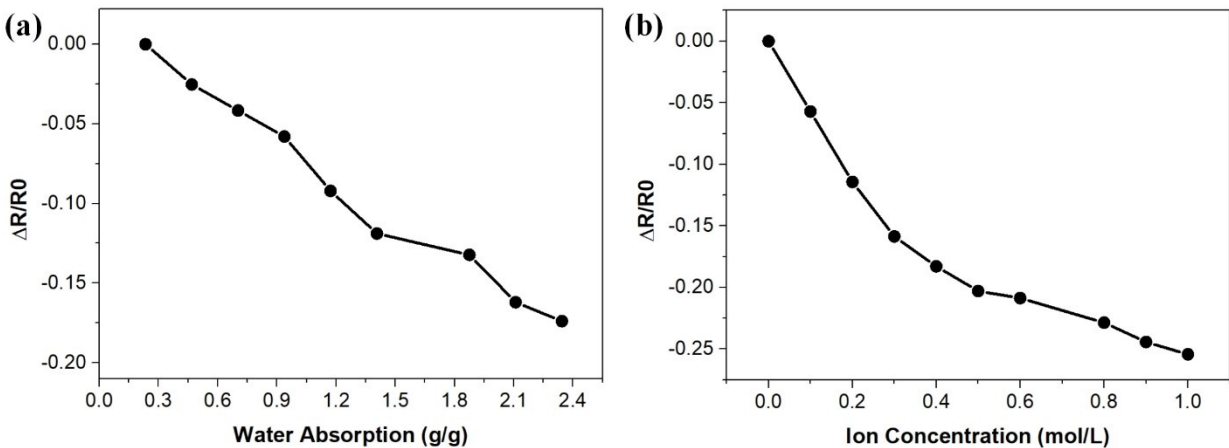
Figure 3.10: The change in the internal resistance of the water-treated cellulose foam as a function of (a) water absorption within cellulose foam and (b) ion concentration in water.
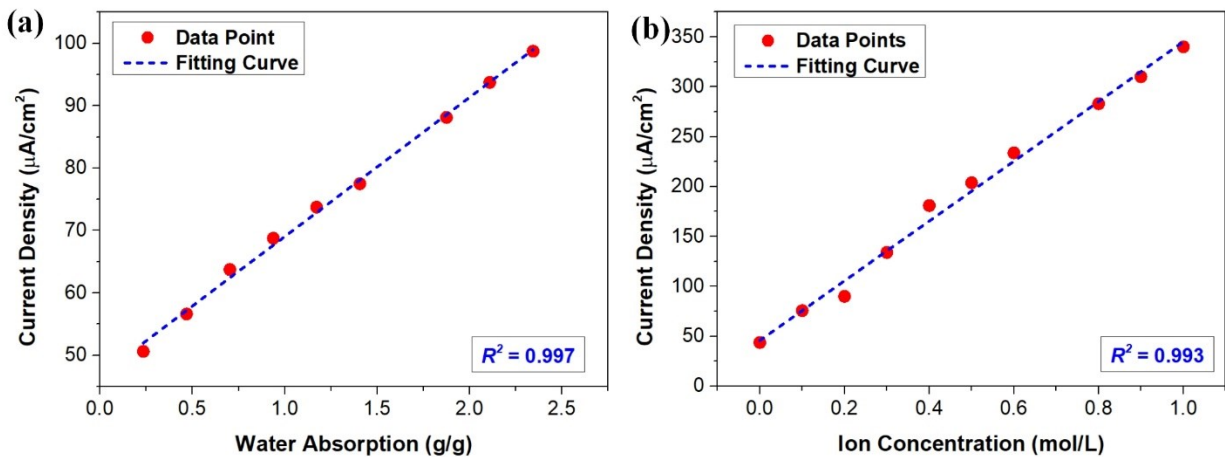
Figure 3.11: Fitting curves for current density data against (a) water absorption and (b) ion concentration.

More interestingly, we further demonstrated a promising potential application of the C-TSMS as pressure and velocity sensors. The amount of triboelectric charge caused by friction is highly dependent on the external pressure and sliding velocity applied to the slide element. To investigate the pressure sensing performance, we measured the output current under various pressure levels. A pressure gradient, created by a constant force, was exerted on the top side of the sliding element in a direction perpendicular to the device (refer to **Figure 3.8b**). During the test, the pressure gradient varied in the range from 0 to 12.26 kP. **Figure 3.12a** displays the electric outputs (*Jsc*) and highlights the analysis of how applied pressure influences the current response of the C-TSMS. At a pressure gradient of 123 Pa, the C-TSMS produced a *Jsc* of 27 µA/cm^2. This value considerably increased to 58.5 µA/cm^2 and then to 103.25 µA/cm^2 as the pressure gradient increased to 4.91 and 12.26 kPa, respectively. The clear correlation between the increased output current and greater pressure gradient can be attributed to the augmented generation of triboelectric charge through friction, as mentioned earlier. Increasing the applied pressure leads to an increment of effective contact area between frictional materials. This results in more adhesion between surfaces and higher friction forces, satisfying the general requirements of the friction equation

$$F_f = C_f . F_A \tag{3.3}$$

where F_f is the friction force, C_f is the coefficient of friction, and F_A is the applied force. Consequently, more triboelectric charges are generated, resulting in higher current output.

Furthermore, we examined an additional physical stimulus that influences the output performance–the sliding velocity. This exploration aimed to investigate the C-TSMS's response to varying sliding velocities, supporting our understanding of its sensing capabilities. In this model study, we systematically characterized current responses across a range of sliding velocities. As illustrated in **Figure 3.12b**, the findings reveal a decline in current density, ranging from 74.5 to 59.25 µA/cm^2, as the sliding velocity increases from 1.33 to 13.12 cm/s, while keeping other parameters unchanged. It is noted that this study introduced the concept of wet friction due to the presence of water within the cellulose foam. Prior research has reported that under wet conditions, the coefficient of friction decreases as the relative sliding velocity increases [278]. This phenomenon is mainly attributed to the reduction in the hydrolysis reaction as the velocity increases, resulting in reduced energy dissipation. Consequently, this contributes to a reduction in

the frictional force, which leads to a decrease in the quantity of triboelectric charge generated through friction. As a result, the current output experiences a decrease.
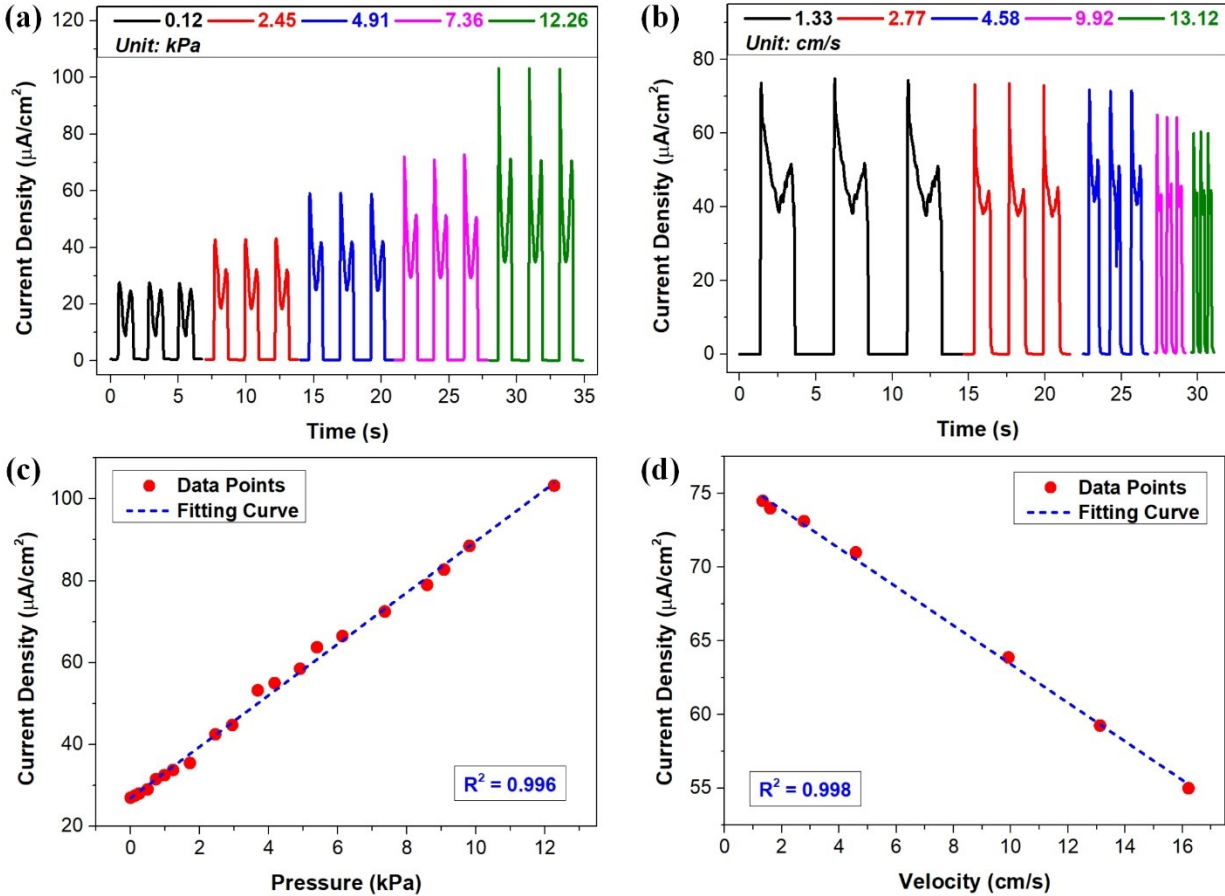
Figure 3.12: Dependence characteristics of C-TSMS's current density on (a) external pressure and (b) sliding velocity. Fitting curves for current density data against (c) external pressure and (d) sliding velocity.

To clarify the sensing capability of the C-TSMS, we conducted an extensive linear regression analysis, focusing on the correlation between the output current and both the input pressure gradient and velocity. **Figure 3.12c** represents the current density (Jsc) correlated with the pressure gradient, varying from 0 to 12.26 kPa, revealing a sensitivity of approximately 6.3 ($\mu A/cm^2$)/(kPa) and an impressive coefficient of determination of 0.996. Similarly, **Figure 3.12d** illustrates the current density as a function of the sliding velocity, ranging from 1.33 to 16.21 cm/s, and indicates a sensitivity of -1.31 ($\mu A/cm^2$)/(cm/s) along with an $R^2 = 0.998$. These results distinctly emphasize the exceptional ability of the C-TSMS to enable sensitive detection of both pressure and velocity variations.

In brief, it has become evident that modifying a single operational parameter while keeping other variables constant significantly affects the resulting current densities. Specifically, the current density exhibited an increase to a certain extent in response to the increased water absorption within the WTCF, ion concentration in water, and applied pressure gradient. Conversely, the current density demonstrated a decrease with an increase in sliding velocity. The nature of increasing and decreasing tendencies in the current density indicates linearity and can be effectively modeled with a linear function. The exceptional coefficients of determination ($R^2 >$ 0.99) prove the substantial potential of the C-TSMS across multifunctional sensing domains, particularly for detecting water absorption, ion concentration, pressure variations, and velocity changes.

3.3. Demonstration of self-powered technology

Figure 3.13a illustrates the complete power-supplying self-powered system, wherein the mechanical energy is converted into DC power by using C-TSMS devices, the generated energy is then stored in an energy storage unit, and subsequently utilized to directly power functional electronic devices. Especially, the capability to generate DC power enables C-TSMS to directly charge an energy storage unit without requiring a rectification method, thereby minimizing energy losses that arise from power management circuits.

Although the C-TSMS delivers a high output current density, its output voltage tends to be relatively low, affecting its applicability as a power source in self-powered systems. In regard to enhancing the voltage output, four unit cells of C-TSMS were connected in a series configuration and synchronized their outputs. The corresponding electrical responses are reported in **Figure 3.13b.** Interestingly, the configuration produced a peak voltage of approximately 2 V. Subsequently, the produced energy was directly employed to charge a capacitor. The voltage variations of capacitors charged by these four series-connected C-TSMS cells are illustrated in **Figure 3.13c**. As observed from this figure, charging a 100 µF capacitor to 1.5 V took less than 15 seconds, while the charging time for 470 µF and 1000 µF capacitors to the same voltage was 50 and 90 seconds, respectively. The inset image shows the curves depicting stored energy with respect to load capacitance for various charging durations. The stored energy (*Ws*) was calculated using Eq. (3.4). It can be observed that an amount of approximately 0.77 mJ and 1.23 mJ of energy were stored

after around 100 s of charging 470 and 1000 µF capacitors, respectively. This amount of energy is sufficient to power several electronic devices.
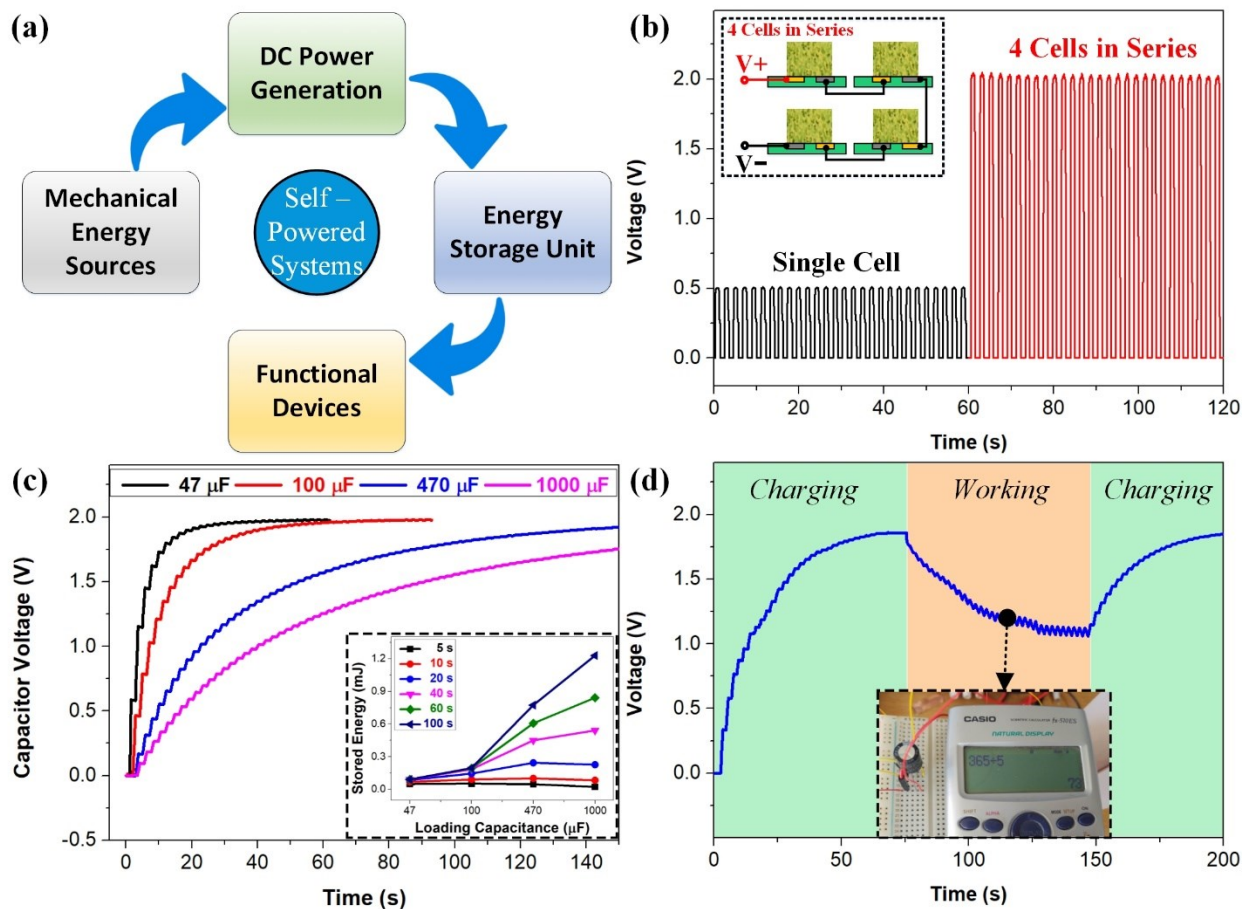
Figure 3.13: Demonstration of self-powered technology using the C-TSMS. (a) Schematic diagram of the complete power-supplying of self-powered system. (b) Enhancement in the output voltage of four series-connected C-TSMS cells. (c) Charging characteristics of diverse capacitors charged using four series-connected cells. Inset image: stored energy concerning the load capacitance for various charging durations. (d) Voltage profile of a 470 µF capacitor charged by four series-connected cells, accompanied by the operational curve for powering a commercial calculator.

Importantly, we experimentally clarified the potential application of energy generated from the C-TSMS devices by employing it to power a commercial CASIO scientific calculator *fx*-570ES, utilizing a 470 µF capacitor charged by four series-connected C-TSMS. Intriguingly, the stored electric energy efficiently powered the calculator for over 50 seconds after a charging time of ~70 seconds, as shown in **Figure 3.13d.** This graph plots the voltage profile of the capacitor during the charging process and the corresponding discharge curve (working) for sustaining the calculator.

This finding proves the great potential of the C-TSMS as a power source seamlessly integrated into self-powered systems.

Concisely, C-TSMS not only introduces the concept of a self-powered system but also showcases promising potential as a multifunctional sensor. This is based on the correlation between the current density and various physical and chemical stimuli, as mentioned previously. The data exhibited strong linear correlations characterized by high sensitivity and impressive coefficients of determination ($R^2 > 0.99$). These abilities give the C-TSMS substantial value for self-powered multifunctional sensing mechanisms.

4. Conclusion

In summary, this study presents an innovative cellulose-based triboelectric self-powered multifunctional sensor. This device effectively generates DC outputs through the use of water-treated cellulose foam and two metal contacts as active materials. Under optimized conditions, the C-TSMS achieves a remarkable current density of 340 $\mu A/cm^2$ and an induced voltage of 0.5 V. Although the relative output voltage may seem low, connecting four C-TSMS cells in a series configuration enhances it to a value of 2 V. The harvested energy can be effectively stored in a capacitor and used to power various electronic devices, exemplified by successfully powering a commercial calculator, demonstrating its practicality in self-powered systems.

Beyond its power generation capabilities, the C-TSMS proves to be a versatile multifunctional sensing mechanism. It exhibits a unique response characterized by robust linear relationships between current density and various applied stimuli, including ion concentrations, water absorption, pressures, and sliding velocities. The device accurately monitors these stimuli by tracking the corresponding output currents, with correlation coefficients consistently exceeding 0.99, validating their accuracy. In conclusion, the C-TSMS shows substantial potential as an innovative approach for mechanical energy harvesting and self-powered multifunctional sensing.

CHAPTER IV – ENHANCING PERFORMANCE OF CELLULOSE-BASED DIRECT-CURRENT TRIBOELECTRIC GENERATOR

This work presents an approach for enhancing the performance of the C-TEG proposed in *Chapter 3* by developing a new structural design, named SLITF-TEG. The new configuration comprises a metal electrode mounted on the surface of a dielectric layer, whereas another metal electrode was laminated to the WTCF and fixed to a movable substrate. It results in the lateral sliding mode of operation instead of the freestanding mode used in C-TEG. The conductive path formed by the hydrogen-bonded network of water molecules due to the interaction between water and cellulose enables charges generated by friction energy to be separated and transferred directly between two metal contacts, resulting in generating DC power. The SLITF-TEG demonstrates an impressive current density of 3.57 A/m2 and can harvest electric power up to 0.174 W/m2 with an induced voltage of approximately 0.55 V. The device generates a direct current in the external circuit, eliminating the limitations of low current density and alternating current found in traditional TEGs. By connecting six-unit cells of SLITF-TEG in series and parallel, the peak voltage and current can be increased up to 3.2 V and 12.5 mA, respectively. Furthermore, the SLITF-TEG has the potential to serve as a self-powered vibration sensor with high accuracy (R^2 = 0.99). The findings demonstrate the significant potential of the SLITF-TEG approach for efficiently harvesting low-frequency mechanical energy from the natural environment, with broad implications for a range of applications

1. Introduction

The demand for alternative renewable energies and energy harvesting technologies has increased in recent years, prompting scientists to search for new, green, reliable, and cost-effective sources of energy. While mechanical energies from wind, water flow, and ocean waves have been established as important sources of power generation, small mechanical energies such as human motions, low-frequency vibration, and raindrops have been overlooked due to their low input energy [4]. However, the rise of portable and functional electronic devices, such as those used in the Internet of Things (IoT), has created a need for continuous, stable, and portable power supplies, making energy harvesting techniques a viable option for powering such devices [1-3]. Additionally, water-based energy harvesting technology has garnered significant research interest due to its

potential, environmental friendliness, and wide availability [5-7]. As a result, researchers are focusing on developing devices capable of converting mechanical energy into electrical energy in a high-humidity environment.

The triboelectric generator (TEG) is a technology that can effectively harvest energy from small mechanical energy sources, introduced by Wang et al. [8-10]. Traditional TEGs work by coupling contact electrification (CE) and electrostatic induction, which involves the accumulation of charges with different signs on the corresponding surfaces when two materials are contacted or slid against each other [235]. Up to now, while several TEG designs have been developed to harvest ambient mechanical energy from the environment, most exhibit alternating current (AC) outputs, requiring conversion to direct current (DC) before use for powering electronic devices. This can be inconvenient and inefficient, particularly for low-power applications. To address this issue, novel strategies and technologies are being developed to directly convert mechanical energy into DC power, with a focus on enhancing the output power density, particularly the current density [107, 257, 279].

Recently, several methods have been proposed for generating DC power using water-based systems. These methods include DC-TEGs, which use water electrification and phase control with an array of disks [73], gas-liquid two-phase flow-based TENG device that combines contact electrification and the breakdown effect [194], and droplet-based electricity generators that produce DC power through direct charge transfer at the water-metal contact interface [147, 185, 188]. Additionally, researchers have developed devices that convert mechanical energy from the movement of a water droplet in any direction within a layered structure composed of graphene, water, and a semiconductor [189], as well as the movement of water between two semiconductors [143]. A particularly interesting development is the dynamic junction theory proposed by Solares-Bocmon et al. [246]. This theory explains the mechanism of the direct current generation at solid-liquid interfaces, which has important implications for the design and optimization of water-based energy harvesting devices. According to this theory, when two materials with different work functions are brought into contact, a charging effect occurs that aligns their Fermi levels and develops a built-in voltage to prevent further net charge transfer. When there is a relative mechanical movement at the contact interface, extra electrons and holes are generated due to the dynamic junction. These are then separated by the built-in electric field, producing direct current

in the external circuit. This means that DC power can be generated due to the movement of the water between two conductors.

On another hand, the output performance of TEGs has been reported to generally decrease in the presence of water due to charge dissipation of the triboelectric charges, which can limit their effectiveness [214-216]. To overcome this limitation, new materials with high triboelectric charges in high-humidity environments need to be identified. For instance, Wang et al. [229] developed a TENG that utilizes the participation of water molecules fixed by hydrogen bonds formed with hydroxyl groups in a polyvinyl alcohol film to enhance the output performance. This is achieved by increasing the charge quantity and, subsequently, the triboelectricity. Mandal et al. [236] proposed a DC generator that employs an active protein layer with a hydrogen-bonded network of water molecules to transfer charges and generate electricity between two dissimilar metal contacts. Interstingly, cellulose has emerged as a promising functional material for the development of low-cost and eco-friendly energy harvesting technologies [219]. Cellulose contains abundant hydroxyl groups that endow it with a strong electron donation capacity, making it highly suitable for the triboelectric effect [218, 224]. Moreover, cellulose is hydrophilic and tends to strongly interact with water. When cellulose comes into contact with water, the hydroxyl groups spontaneously form hydrogen bonds with water molecules. This leads to the fixing of water molecules on the surface of cellulose and the formation of a conductive path through the hydrogen-bonded network of water molecules [225-228]. This property of cellulose could be an important factor to explore in solving the problem of the decreasing trend of electricity performance in high-humidity environments.

In this chapter, we introduce a novel direct-current triboelectric generator (TEG) that uses a water-treated cellulose foam (WTCF), made by absorbing water into a cellulose foam, as its active layer to generate electric power from low-frequency vibration energy. The SLITF-TEG comprises a metal electrode mounted on the surface of a dielectric layer, whereas another metal electrode was laminated to the WTCF and fixed to a movable substrate. The mechanism of this device relates to the CE and the charging effect between two materials with different work functions, a well-known phenomenon that was thoroughly characterized by Lord Kelvin [230, 231]. This device is capable of converting mechanical energy from the relative sliding of the WTCF into DC power based on the dynamic junction of the WTCF and metal contacts. The study systematically examined the

impacts of working parameters and material selection on the SLITF-TEG 's output performance. Our findings show that SLITF-TEG can produce an impressive current density of 3.57 A/m^2, a power density of 0.174 W/m^2, and an induced voltage of approximately 0.55 V. The voltage and current can be increased up to 3.2 V and 12.5 mA by simply synchronizing the outputs of six-unit cells of SLITF-TEG connecting in series and parallel, respectively. Six-unit cells in series can produce an output energy of 2 mJ in 100 s and store it directly in a 1 mF capacitor without requiring rectification. This amount of energy is adequate for powering various electronic devices. Additionally, we demonstrate the great accuracy and potential application of SLITF-TEG for measuring the vibration frequency/sliding velocity with a high coefficient of determination ($R^2 =$ 0.99). Overall, these results illustrate the high potential of SLITF-TEG in mechanical energy harvesting and the field of self-powered sensor fabrication.

2. Experimental section

For preparing the materials, aluminum (Al) and copper (Cu) tapes were bought from Ducksung Hitech (Ducksung Hitech Co., LTD, Seoul, South Korea). The cellulose foam is manufactured by Hankook Tamina (Hankook Tamina Co., LTD, Hanam, South Korea). Distilled water was used from our research laboratory. Indium tin oxide (ITO) electrode (10 Ω/sq), polytetrafluoroethylene film (PTFE, 100 μm -thick), and polyvinylidene fluoride (PVDF, 50 μm -thick) were purchased from Sigma-Aldrich (Sigma-Aldrich, St. Louis, MO, USA). Besides, the mica, nylon, and resistors were purchased from a local market. Capacitors were purchased from Rubycon (Rubycon Corporation, Nagato, Japan).

To fabricate the SLITF-TEG, the Cu and Al tapes were cut into rectangular pieces of the same size (2 cm x 4 cm or 2 cm x 3.5 cm), and devised the electrical circuit as the bottom and top electrodes, respectively. A PTFE film (8 cm x 8 cm) was utilized as the dielectric layer and a water-treated cellulose foam (WTCF), was fabricated by absorbing distilled water (1 to 3.5 mL) into a cellulose foam (3 cm x 4 cm or 2 cm x 3.5 cm; 0.5 cm -thick), was used as an active friction layer. The Cu electrode was mounted on the PTFE layer, whereas the Al electrode was laminated to the WTCF and fixed to a movable substrate. The WTCF reciprocates on the surface of the dielectric layer and the bottom electrode, resulting in the lateral sliding mode of operation of the SLITF-

TEG. Load resistances (10 Ω to 10 MΩ) and capacitances (0.1 to 6.8 mF) are applied in the external circuit.

The general physical process for energy conversion has three important steps: charge generation, charge separation, and charge flow [268]. In the proposed mechanism, charges are generated by friction energy during the relative sliding of the WTCF and separated under the effect of the built-in electric field developed between the two metal contacts. These charges are facilitated to transfer through metal/WTCF/metal counterparts via a conductive path formed inside the WTCF in one orientation, leading to generating a direct current through an external circuit. The impacts of working parameters and material selection on the output performance of the SLITG-TEG are systematically investigated, including vibration frequency, water absorption, different materials of the dielectric layers, and electrode pair materials.

3. Results and discussions

3.1. Electric output characteristics

The schematic experimental setup of the system consists of a slider crank mechanism that simulates mechanical vibration, a SLITF-TEG cell, and external measuring equipment, as shown in **Figure 4.1**.
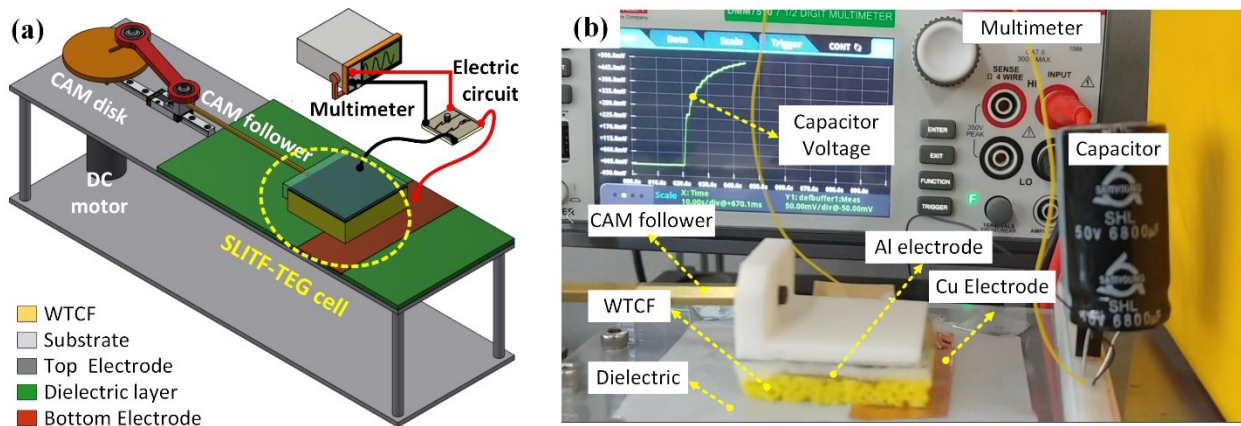
Figure 4.1: (a) Schematic diagram and (b) Real photograph of the experimental setup of the SLITF-TEG.

For constructing the SLITF-TEG cell, we used copper (Cu) and aluminum (Al) films (2 cm × 4 cm) as the bottom and top electrodes, respectively, and placed a PTFE film (8 cm × 8 cm) as the dielectric layer. We then fabricated the WTCF by absorbing 3.5 mL of distilled water into a

cellulose foam (3 cm × 4 cm × 0.5 cm, 0.64 g -mass). The Cu electrode was mounted on the PTFE layer, whereas the Al electrode was laminated to the WTCF and fixed to a movable substrate (8.78 g mass). To evaluate the electric output characteristics of SLITF-TEG, The WTCF was driven to reciprocate on Cu and PTFE surfaces with a period time of about 2 s, corresponding to a sliding velocity of 3.5 cm/s, as shown in **Figure 4.2**.
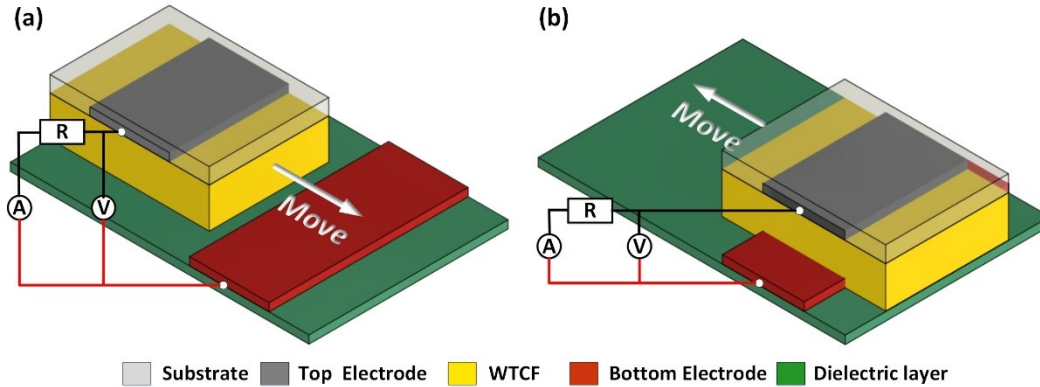
Figure 4.2: 3D schematic illustrations of the measurement setup and the external circuit corresponding to (a) disconnected and (b) connected states of the ideal cycle of operation.

We measured the voltage output under the open-circuit condition and plotted the results in **Figure 4.3a**. It can be observed that the device can produce a continuous DC voltage (Voc) with all positive pulses due to the continuous reciprocating motion, with an average peak value of ~0.52 V and a time interval of the pulse ΔT of ~2 s. We also measured the current output under the short-circuit condition (Isc). The current peaks showed an increasing trend with the increasing number of movement cycles and approached a stable saturation value after a sufficiently long time, as shown in **Figure 4.4a. Figure 4.3b** displays the Isc curve based on the saturation, in which a similar signal waveform to the voltage output is observed. From this figure, the peak current value can reach ~3.12 mA, corresponding to a current density of 2.6 A/m2, and the time interval between current peaks is also ΔT. The estimated charge transfer during one movement cycle obtained 3.3 mC, corresponding to a charge density of 2.75 C/m2, as shown in the inset image. The estimated charge transfer Q is described by

$$Q = \int i.dt \tag{4.1}$$

where i is the instantaneous current and t is the time.
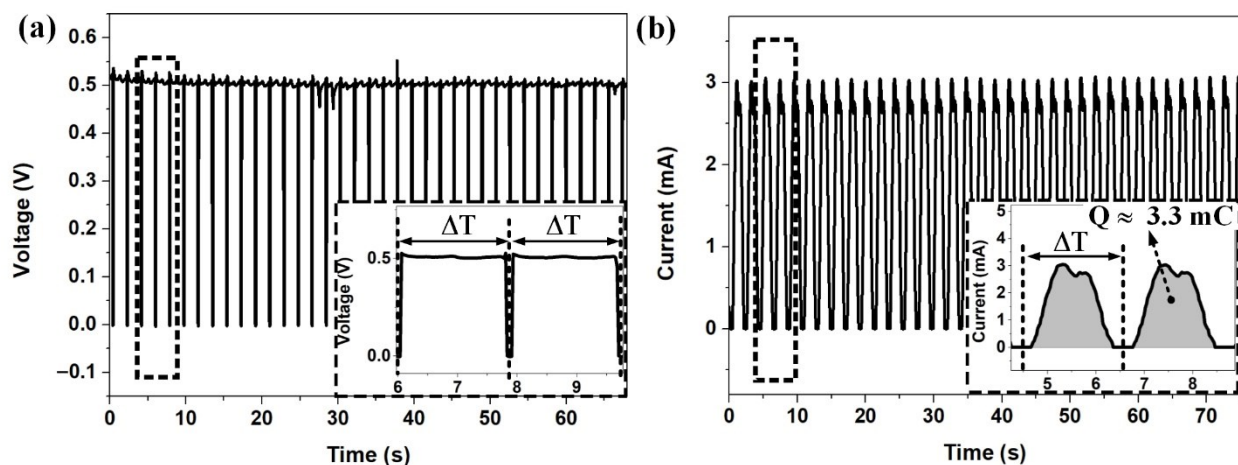
Figure 4.3: The electrical characteristics of the SLITF-TEG. (a) The open-circuit voltage. Inset image: partial magnified view of the voltage. (b) The short-circuit current. Inset image: partial magnified view of the current signal and estimated charge transferred.
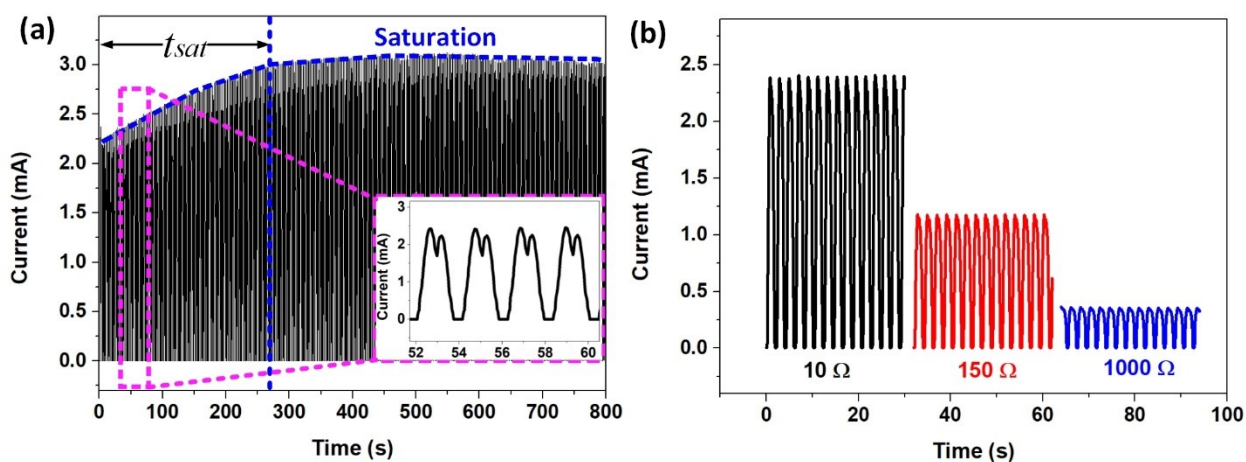
Figure 4.4: Electrical responses of the SLITF-TEG. The current outputs are measured under (a) the short-circuit condition and (b) various load resistances in the external circuit (10 Ω, 150 Ω, and 1000 Ω).

Importantly, we observed that the DC pulse outputs were obtained when the WTCF was brought into contact with the Cu electrode following the reciprocating motion. Otherwise, both voltage and current outputs are negligible, and the current flow is unidirectional from the Cu electrode to the Al electrode. We also confirmed experimentally the DC characteristics of electric outputs by applying various load resistances and capacitances in the external circuit. The current outputs measured at 10 Ω, 150 Ω, and 1000 Ω load resistances are plotted in **Figure 4.4b**, and the corresponding enlarged views of typical peaks are illustrated in the inset image of **Figure 4.5a**. All these results illustrate pulsed DC characteristics of SLITF-TEG.

We also investigated the dependence of current output on the load resistance in a range from 10 Ω to 10 MΩ and found that the value of peak current can reach 2.386 mA at 10 Ω and dramatically decreases to 50 µA and then 50 nA when the load resistance increases to 10 kΩ and then 10 MΩ, respectively. Figure 2e also displays the output power (P) as a function of external resistance. The power initially increases with increasing the external resistance to reach a maximum value of 208.86 µW at 150 Ω, corresponding to a power density of 0.174 W/m2, and then decreases with a further increase in the RL-value. We calculated the output power by using **Eq. (2.3).**

The ability of the SLITF-TEG to generate DC outputs allows for the direct charging of energy storage units without the need for a rectifier. We verified this capability by exploring the charging behaviors across different load capacitances CL (0.1 to 6.8 mF) of the SLITF-TEG, and the experimental results are presented in **Figure 4.5b**. The trends of charging voltage with the charging time and various load capacitances CL have similar tendencies, where the capacitor is typically charged rapidly in the beginning and slows down until reaching a saturated voltage. It is noted that the smaller CL needs less time to reach saturation than the larger CL. Moreover, the stored power–time relationships for a fixed capacitor CL = 6.8 mF are plotted in the inset image, which indicates an optimum charging time where the maximum stored power is obtained. This inset image also shows the stored energy–time relationship, which increases gradually until reaching a saturation value of approximately 0.884 mJ. We calculated the stored energy Ws by using **Eq. (2.4).**
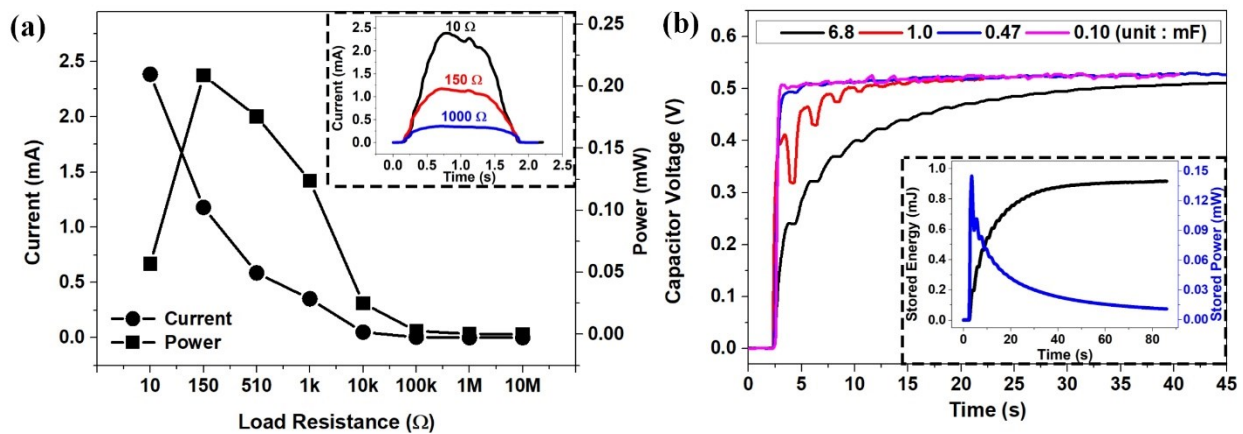
Figure 4.5: (a) The impedance-matching curve of the SLITF-TEG. Power and average current as a function of load resistance. Inset image: Enlarged view of typical peaks of current output at

different load resistances. (b) Charging voltage on various load capacitances. Inset image: Stored energy-time and stored power-time relationships for a fixed capacitor of 6.8 mF.

3.2. Working mechanism

SLITF-TEG works by exploiting the natural electron transfer that occurs when two materials with different work functions come into contact, in which electrons transfer from the material with a lower work function to the material with a higher work function. This transfer continues until the Fermi levels of both materials align, resulting in a built-in electric field (Ebi) and a voltage (Vbi) across the materials (**Figure 4.6a**). The built-in voltage V_{bi} is given by **Eq. (2.1)**, where $\phi 1$ and $\phi 2$ are the material work functions of materials 1 and 2, respectively, and q is the elementary charge [230-232, 246].
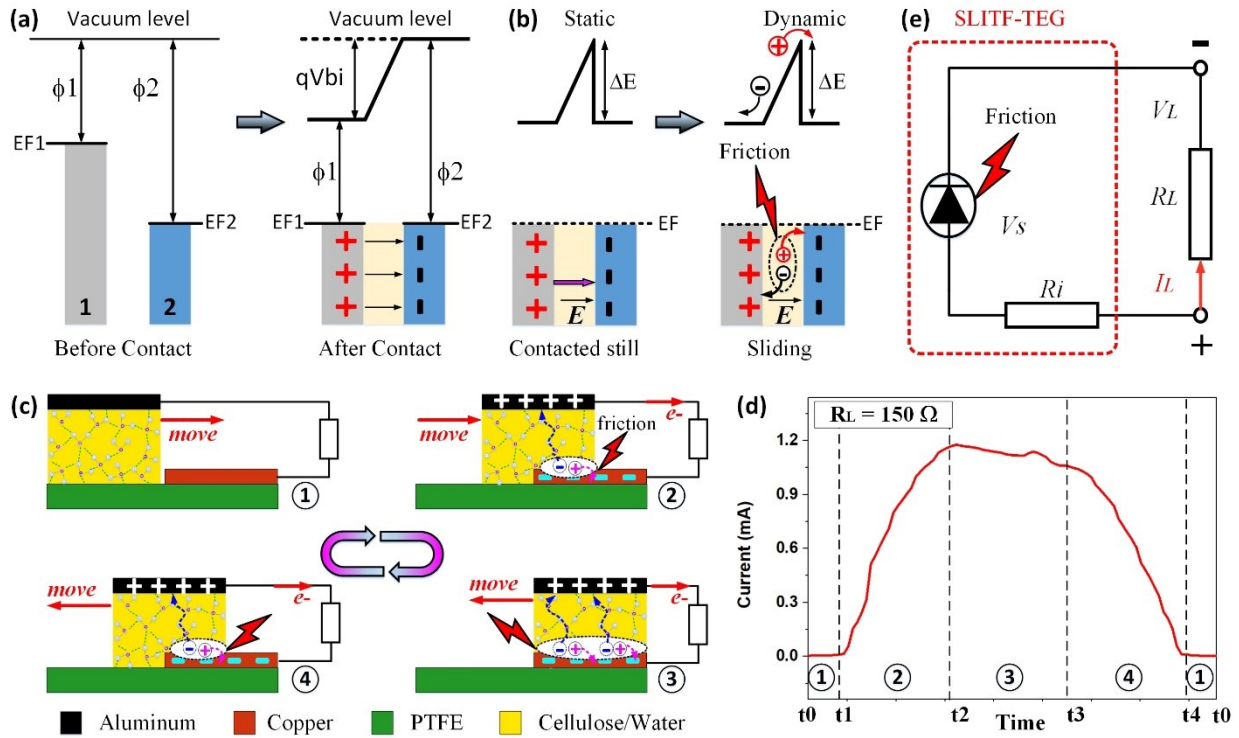
Figure 4.6: (a) Electron energy levels of materials 1 and 2 before and after making contact. Here, EF1 and EF2 are Fermi levels of materials 1 and 2, respectively. (b) Space charge, built-in electric field, and potential after two materials are in contact at a static state and separation charges in a dynamic state. (c) The working mechanism of the sliding mode SLITF-TEG. (d) Magnified view of a current output signal during an ideal operating cycle of the SLITF-TEG. (e) Equivalent circuit diagram of the SLITF-TEG.

When the two materials are in static contact (i.e., contacted still), the equilibrium state is established, and the built-in electric field prevents further net charge transfer. On the contrary, when they are in dynamic contact (i.e., sliding), extra charges (or nonequilibrium carriers) can be generated due to mechanical friction energy (**Figure 4.6b**). These extra charges (Qtri) can come from two sources: (1) charges generated by the CE during the sliding friction and (2) charges generated by energy released as a result of bond breakage at the interface during dynamic friction. These extra charges will be separated under the effect of the built-in electric field in one orientation, providing the main driving force of DC generation in the SLITF-TEG. The generated current density (J_{SC}) can be expressed by **Eq. (2.2)** [247, 248]. Therefore, the use of WTCF plays a crucial role in generating high-output performance. As mentioned above, the interaction between the water and cellulose leads to the fixing of water molecules on the surface of cellulose and the formation of a conductive path through the hydrogen-bonded network of water molecules inside the cellulose foam. Accordingly, more charges will be generated during the friction and these charges will be facilitated to flow through the whole circuit, leading to generating high-output performance, particularly high-output current.

The working mechanism of SLITF-TEG is illustrated in **Figure 4.6c**. When the WTCF was not in contact with the bottom electrode (Cu), there was no current output in the external circuit (**Figure 4.6c**, step 1). However, when it was brought into contact, the top electrode (Al) affixed to WTCF was connected electrically with the Cu electrode through a conductive path formed by the hydrogen-bonded network of water molecules inside WTCF (**Figure 4.6c**, step 2). This leads to the development of the built-in electric field/voltage across Al and Cu electrodes caused by their difference in work functions. During the sliding of WTCF on the Cu electrode, extra charges are generated due to CE at the contact interface and then separated by the built-in electric field via the conductive path. The work functions of Cu and Al were approximately 4.7 eV and 4.2 eV [236, 246, 280-282], respectively; thus, the built-in electric field points from the Al electrode to the Cu electrode. As a result, charges will flow through WTCF/metals interfaces to the external circuit in one orientation. Concisely, negative charges/electrons generated by the friction energy transfer from the Cu electrode to WTCF and then to the Al electrode via the conductive path formed inside WTCF under the effect of the built-in electric field and eventually to the Cu electrode via the external circuit. The output electrons flowed unidirectionally from the Al electrode to the Cu

electrode, resulting in DC power generation. The DC outputs are still obtained even when WTCF continues sliding to the end of the right alignment (**Figure 4.6c**, step 3) and then moving back to the initial state (**Figure 4.6c**, step 4). The reverse lateral sliding process is the same as in Figure **5.3c**, step 2. Thereafter, no current flowed in the external circuit when WTCF separated from the Cu electrode and moved backward to the initial position as in Figure **5.3c**, step 1.

Briefly, the working mechanism of SLITF-TEG can be divided into two primary states. In the first state, the WTCF and the Cu electrode were separated, and the electric outputs were negligible (**Figure 4.6c**, step 1). In the second state, the WTCF was brought into contact and slid on the surface of the Cu electrode (**Figure 4.6c**, steps 2–4), and voltage/current was generated. The maximum output was achieved when the WTCF and the Cu electrode were in full contact (**Figure 4.6c**, step 3). Consequently, the SLITF-TEG can produce continuous pulsed DC electricity by periodically sliding the WTCF. Notably, the DC characteristics of the device depend on the built-in electric field developed between two electrodes.

A detailed current output signal during one movement cycle, measured at a load resistance of 150 Ω, is shown in **Figure 4.6d**, demonstrating the consistency between the electrical responses and the working mechanism. The current output starts when the WTCF contacts the Cu electrode (*i1*) and increases until the WTCF and the Cu electrode are in full contact (*i2*). When the WTCF moves backward (*i3*), the current value decreases as the contact area between the WTCF and the Cu electrode decreases. Once the WTCF separates from the Cu electrode (*i4*), the current becomes negligible. The corresponding experiment is presented in **Figure 4.7.**

It is worth noting that the Cu/WTCF/Al structure acts as a diode-like component, allowing current to flow through the structure in a single orientation during the electricity generation process. Looking at the device from a circuit perspective, the SLITF-TEG can be modeled as a friction-induced generation diode-like voltage source (Vs) (Cu/WTCF/Al—related to the voltage difference formed by the nonequilibrium carriers during the sliding friction), an internal resistance Ri (WTCF), and a load resistance RL. This device can produce DC output (IL) and voltage (VL) through the external resistance RL. **Figure 4.6e** illustrates the equivalent circuit diagram of SLITF-TEG.
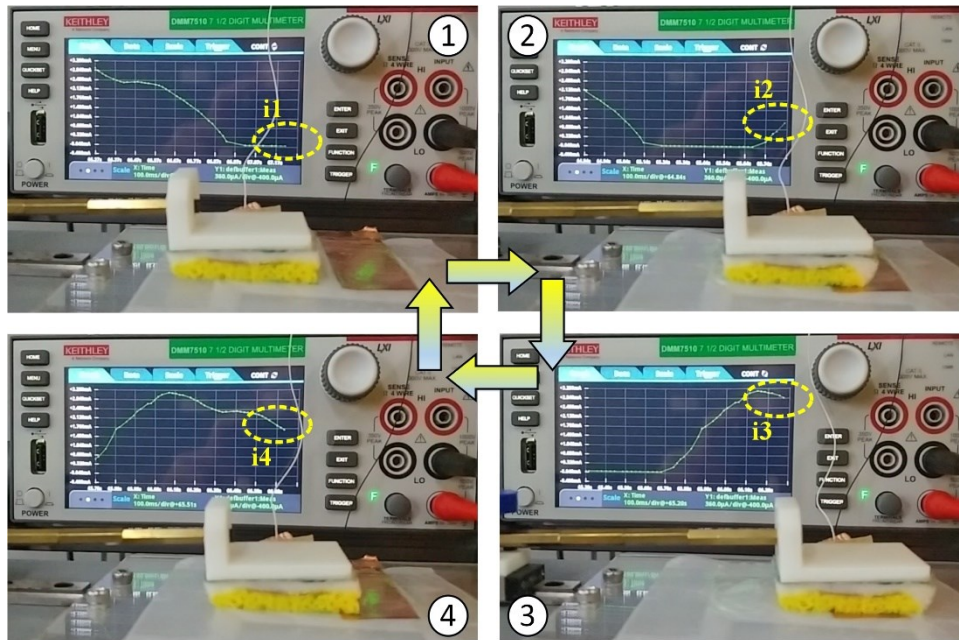
Figure 4.7: Demonstration of the consistency between the electrical responses and the working mechanism of the SLITF-TEG.

3.3. Affecting parameters

In order to gain further insights into the electrical output and impedance characteristics of the SLITF-TEG, we explored the influence of different working parameters. As a model study, we first investigated the important role of mechanical friction in generating high-output performance. We measured the electric responses when keeping the WTCF stationary on the Cu electrode and then compared it with that of the sliding mode mentioned earlier. The electric outputs of the stationary mode showed a constant voltage of approximately 0.52 V, while the current dramatically decreased from 75 µA to a stable saturation value of 8 µA after 700 s (**Figure 4.8**). Although the maximum voltages in both stationary and sliding modes were almost the same, the current generated in the sliding mode was more than 375 times higher than those in the stationary mode, demonstrating the essential role of mechanical friction and the CE in enhancing the output performance of the SLITF-TEG.
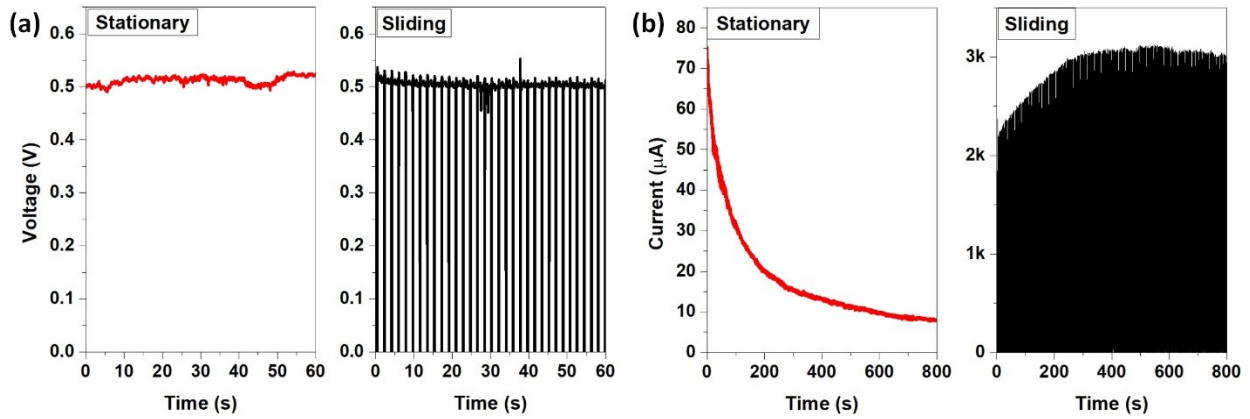
Figure 4.8: The comparison of (a) open-circuit voltage and (b) short-circuit current of the SLITF-TEG in the stationary and sliding modes.

Simultaneously, we examined the effects of sliding velocity, which is driven by the vibration frequency of the reciprocating motion, on the maximum instantaneous electric outputs (Voc and Isc). By comparing the electric outputs under different vibration frequencies in the range from 0.21 to 2.22 Hz, we found that the sliding velocity had little effect on the peak values of Voc and Isc, with a slight difference of less than 1% and 6%, respectively (**Figures 4.9** and **4.10a**). However, we observed a decreasing trend in the time interval for reaching the maximum instantaneous current and the transferred charge (Qc) during one movement cycle with increasing vibration frequency, as depicted in **Figure 4.10b**. From this figure, the value of Qc decreased from 6.55 to 0.64 mC/cycle when the vibration frequency increased from 0.21 to 2.22 Hz. This could be due to the decrease in the working period caused by the increase in the vibration frequency.
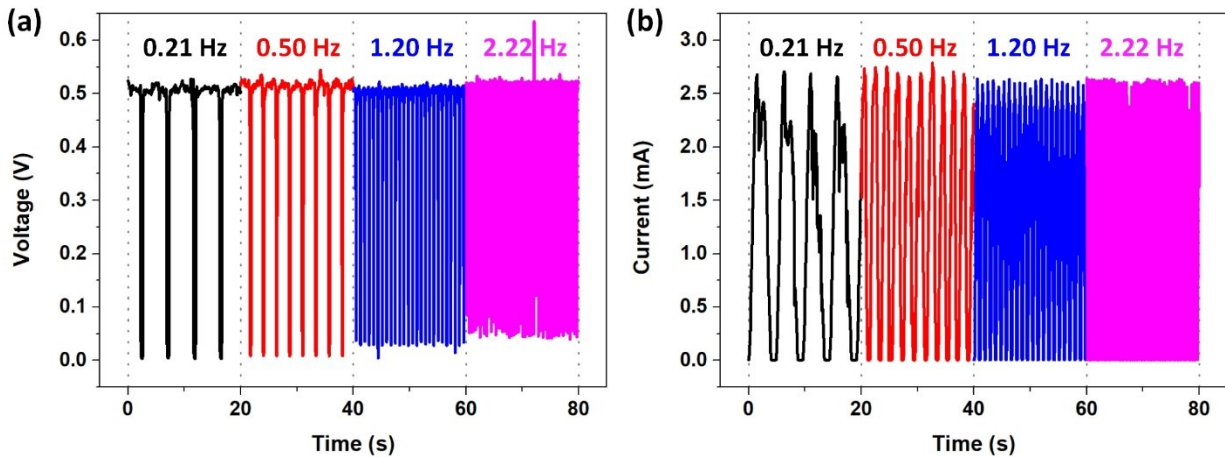
Figure 4.9: (a) Open-circuit voltage and (b) Short-circuit current of the SLITF-TEG under different vibration frequencies.

Figure 4.10: The dependence of (a) open-circuit voltage and short-circuit current and (b) Transferred charges during one movement cycle on the vibration frequency. Inset image: Enlarged view of typical peaks of current output with different frequencies.

We also investigated the essential role of water absorption of WTCF on the electric outputs to further optimize the output performance of the SLITF-TEG. Water absorption is defined as the amount of water absorbed by the cellulose foam and is calculated as the ratio of the weight of water absorbed to the weight of the dry cellulose foam. The results showed an impressive power generation capacity, in which the current output exhibited an upward trend from 0.5 to 3.12 mA, corresponding to a current density from ~0.42 to 2.6 A/m2, when the water absorption of the WTCF increased from 1.56 to 5.46 g/g, as presented in **Figure 4.11a**.

This was presumably due to the effect of the internal resistance of WTCF on the current output. Previous studies have demonstrated that the increasing amount of absorbed water leads to an increase in the concentration of hydrogen bonds, resulting in a decrease the internal resistance [236]. Therefore, charges generated during the sliding motion are facilitated to transfer through the conductive path formed by the hydrogen-bonded network of water molecules inside WTCF, leading to generating high output current. To test this hypothesis, we measured the internal resistance of WTCF at different water absorption levels, finding that the internal resistance of WTCF considerably decreased from 217 to 102 kΩ when the water absorption increased from 1.56 to 5.46 g/g (**Figure 4.11b**). Meanwhile, the peak voltage output remained almost the same at ~0.52 V despite the increase in water absorption.

Subsequently, to demonstrate the crucial role of the WTCF in the enhancement of energy conversion of the SLITF-TEG, we compared it to a conventional solid-solid triboelectric generator (SS-TEG) with the same structural design but using dry cellulose foam instead of WTCF. We found that SS-TEG exhibited a peak Voc of about 0.2 V and Isc of 30 nA with AC output characteristics (**Figure 4.12**).
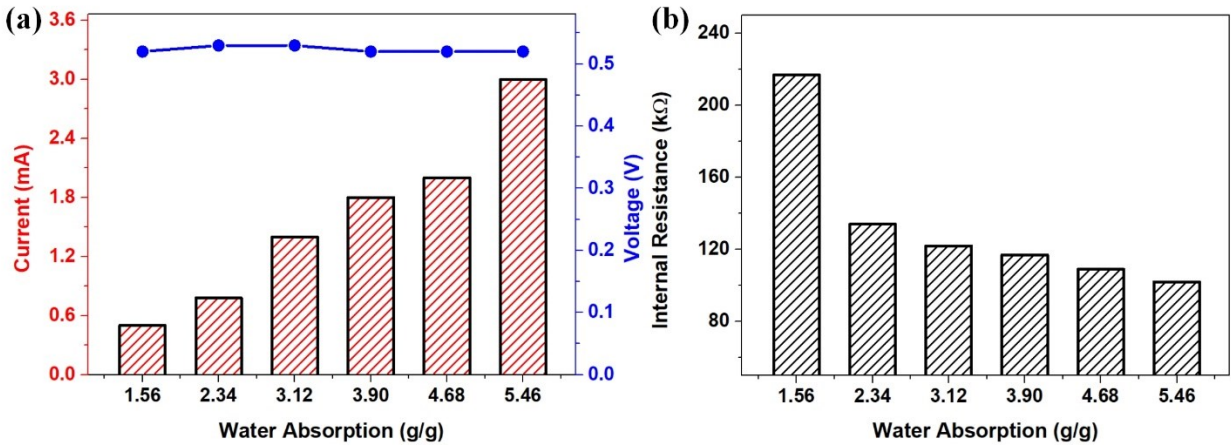
Figure 4.11: The dependence of (a) open-circuit voltage and short-circuit current and (b) Internal resistance of WTCF on the water absorption.
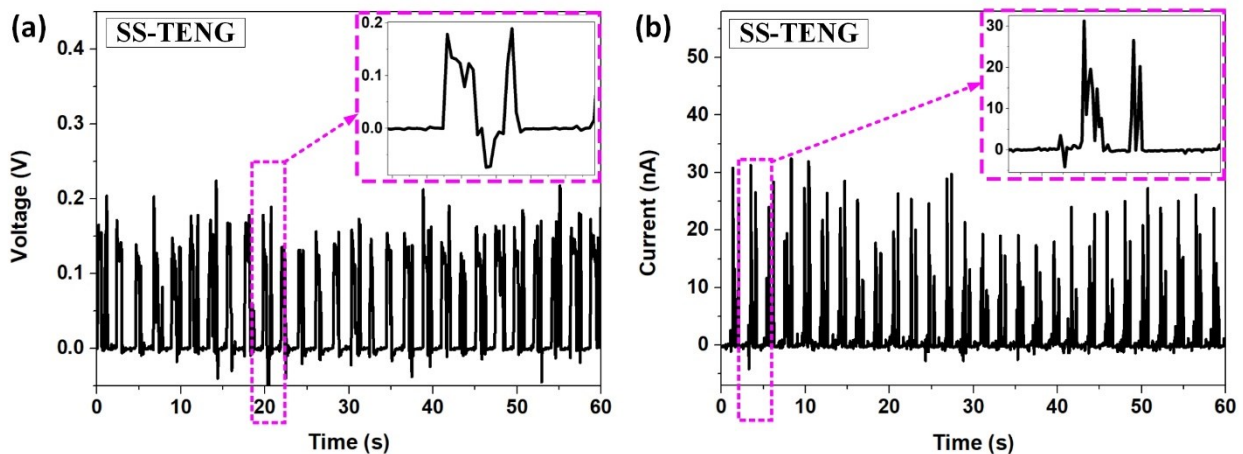
Figure 4.12: (a) Open-circuit voltage and (b) Short-circuit current of the SS-TEG using a dry cellulose foam.

Furthermore, we also realized an electrochemical cell (EC) composed of Al and Cu electrodes immersed in water, which implied constant voltage and current outputs with average values of ~0.5 V and 5 μA, respectively (**Figure 4.13a**). Comparison between the SLITF-TEG, SS-TEG, and EC found significant improvements in generating a high output current of SLITF-TEG, with over 600

times more output current than both the SS-TEG and EC (**Figure 4.13b**). Notably, the internal resistances in the cases of SS-TEG and EC are respectively obtained at 6 MΩ, and 1.2 MΩ, considerably higher than the internal resistance of the SLITF-TEG (102~207 kΩ). Overall, these results strongly support our conclusion that fabricated WTCF is essential for an effective mechanical-to-electrical energy conversion technology.
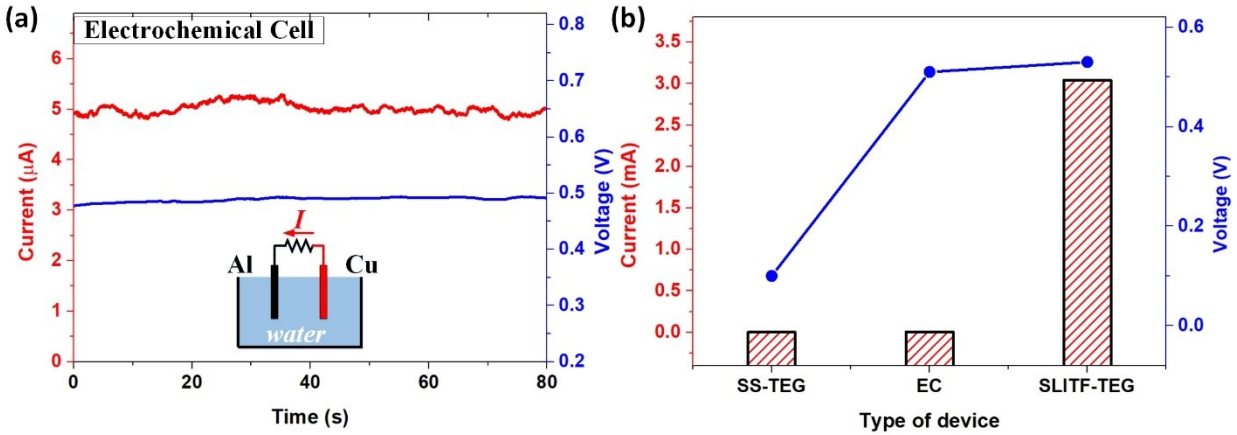
Figure 4.13: (a) Open-circuit voltage and short-circuit current of an electrochemical cell. (b) Comparison in output performances of SS-TEG, EC, and SLITF-TEG.

Further research revealed how the dielectric layer impacts the output performance. In the triboelectric mechanism, selecting material pairs with a large difference in surface charge is critical for generating more triboelectric charges and then maximizing the outputs. As previously mentioned, water and cellulose foam are combined into one reactive entity and participate in CE as a high electropositivity material. Certainly, a dielectric layer with a high negative surface charge is suitable for generating a relatively high electrical [283]. To confirm this, we considered different polymers within the triboelectric series, including (most negative) PTFE, PVDF, nylon, and mica (most positive), as possible dielectric layers. Experimentally proved that the peak voltage remained at almost the same value, but more negative materials exhibited higher current outputs (**Figures 4.14** and **4.15**).

The average peak Isc generated using mica as the dielectric layer was observed at 2.23 mA, with an estimated charge density of about 1.61 C/m2. Replacing the mica layer with nylon, PVDF, and PTFE layers resulted in a significant improvement in the average peak Isc by approximately 13%, 31%, and 37%, while the transferred charge density increased by 26%, 36%, and 64%,

respectively. Interestingly, the maximum current output order matched well with the triboelectric ordering between the materials of the dielectric layers, where the more negative triboelectric materials generated higher current outputs. This increasing trend could be attributed to the increase in the number of triboelectric charges generated by the CE of the WTCF and the dielectric layer. The electropositive WTCF produced more triboelectric charges during CE with a higher negative triboelectric material, resulting in higher current outputs.
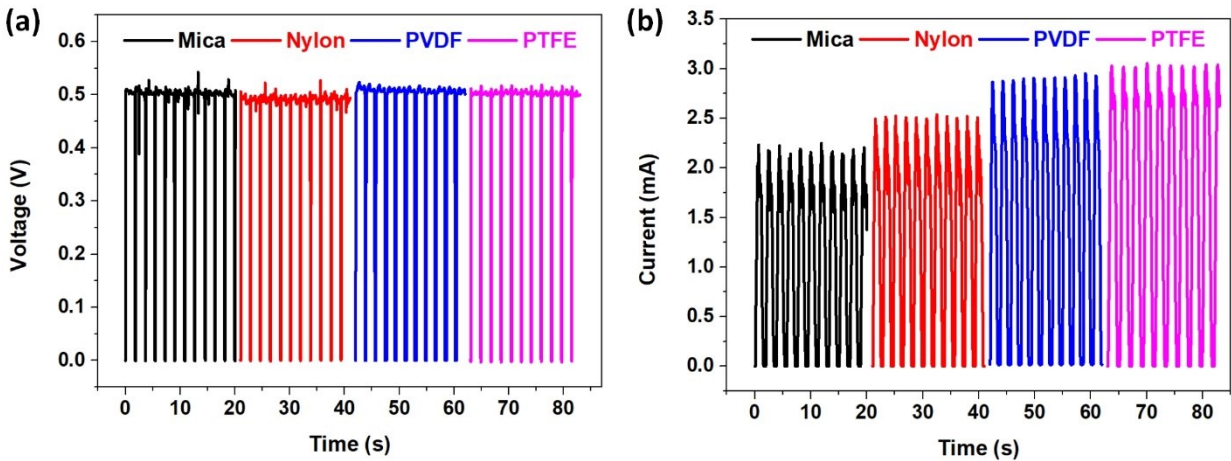
Figure 4.14: (a) Open-circuit voltage and (b) Short-circuit current of the SLITF-TEG using different materials of the dielectric layer.
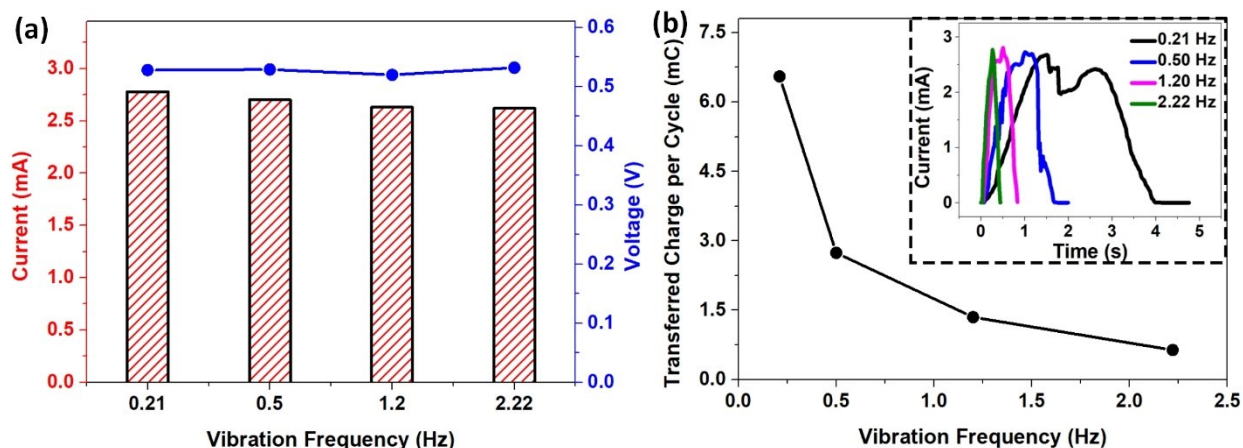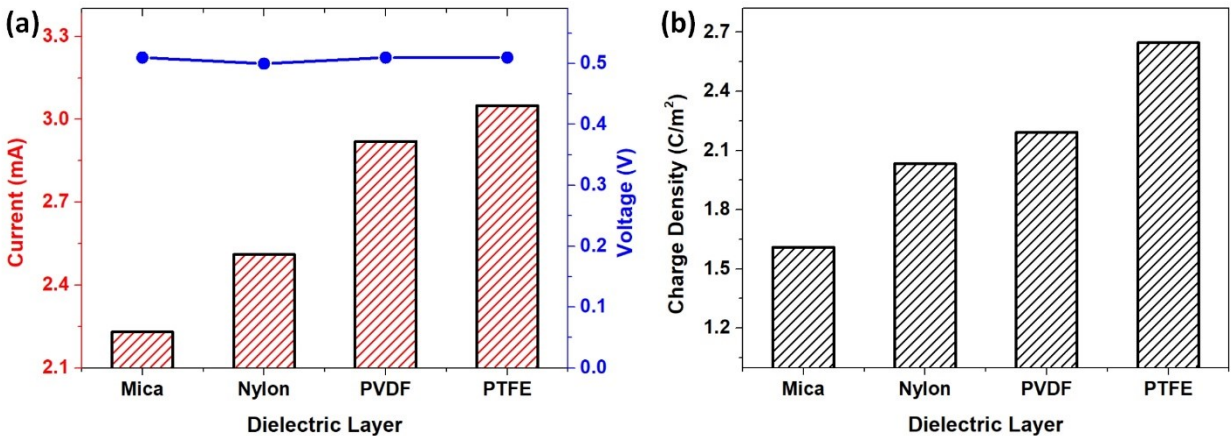

Figure 4.15: The dependence of (a) open-circuit voltage and short-circuit current and (b) transferred charge density during one movement cycle using different polymers for dielectric layers.

96

3.4. Applications

To demonstrate the great potential application of SLITF-TEG as an advanced mechanical energy harvester, we compared its output performance with various cellulose-based nanogenerators and DC mechanical energy harvesters [12, 34, 61–72] (see **Table 4.1**). For instance, Bai et al. [224] developed a high-output CP/LTV-TENG that can produce a peak Voc of 478 V and a current density (Jsc) of 0.063 A/m2. Chen et al. [107] reported a low-cost and efficient DC FLU-TENG that can generate DC energy with a peak Voc of 4500 V and a Jsc of 0.0084 A/m2. Moreover, Zheng et al. [254] designed high-performance flexible piezoelectric nanogenerators using a flexible porous CNF/PDMS aerogel film that can produce a Voc of ~60 V and a Jsc of ~0.0505 A/m2. Although SLITF-TEG shows a high current output density, the voltage output is relatively low, around 0.5 V, compared to the reported studies. In regard to enhancing the maximum voltage and current outputs, multiple unit cells of SLITF-TEG could be connected in series or parallel and synchronize their outputs. Importantly, the output current density generated by SLITF-TEG increased by 376% compared to those generated by the C-TEG mentioned in *Chapter II*, demonstrating the advance of this newly designed device in enhancing output performance (see **Table 4.1**).

Table 4.1: Peak voltage and current density of various mechanical energy harvesters

Types	Active materials	Size	Peak voltage (V)	Current density (A/m^2)	Ref.
Piezoelectric Generator	C/PDMS/AuNPs	3.5 cm x 8.5 cm	6 V	$2.35.10^{-4}$	[251]
	CMC/PDMS/CNT	3.3 cm x 2.5 cm x 2 mm	30	$6.06.10^{-4}$	[255]
	Cellulose/SbSI	1 cm x 1 cm x 50 μm	0.024	2.10^{-4}	[253]
	TOCN/PDMS	1 cm x 2 cm x 0.48 μm	60	$5.05.10^{-2}$	[254]
	MoS2/PVDF	3 cm x 3 cm	50	$3.33.10^{-5}$	[252]
	ZnO nanowire array	~2 mm^2	10^{-3}	$7.5.10^{-5}$	[260]
	ZnO nanosheets/Zn: Al layered double hydroxide layer	6 mm^2	0.38	0.217	[256]
Triboelectric Generator	Treated wood	4.5 cm x 4.5 cm	81	$8.89.10^{-4}$	[220]
	PCL/GO	4 cm x 4 cm	120	$2.5.10^{-3}$	[221]
	Ppy-MWCNT	6.25 cm^2	196.8	$5.04.10^{-2}$	[223]

	CA/PEI/LTV	5 cm x 5 cm	478	$6.30.10^{-2}$	[224]
	PA/nylon-66	6.8 cm x 7 cm	4500	$8.40.10^{-3}$	[107]
	FEP/Cu/Steel/Acrylic/ABS	7.5 cm x 7 cm	149.5	$4.11.10^{-3}$	[106]
	PTFE/Acrylic	10 cm^2	33	0.065	[109]
	Cellulose/Water/Al/Cu	1 cm x 4 cm	~0.5	0.75	Chapter II
Our generator	Cellulose/Water/Al/Cu	2 cm x 3.5 cm	~0.5	3.57	This work

In this study, WTCF was fabricated by absorbing 2.5 mL water into a cellulose foam with the dimension of 2 cm × 3.5 cm × 0.5 cm (0.37 g -mass). The corresponding electrical responses are reported in **Figure 4.16**, which prove that a single cell of SLITF-TEG can produce a maximum instantaneous Voc of 0.55 V and Isc of 2.5 mA, corresponding to a current density of 3.57 A/m2. Intriguingly, six-unit cells connecting in parallel could produce a peak current of about 12.5 mA, and a voltage of approximately 3.2 V could be obtained by six-unit cells connecting in series. Remarkably, the ability to generate DC outputs enables this device to directly charge an energy storage unit, such as a capacitor, without requiring any rectifier. The charging behaviors of different capacitors are presented in **Figure 4.17**.
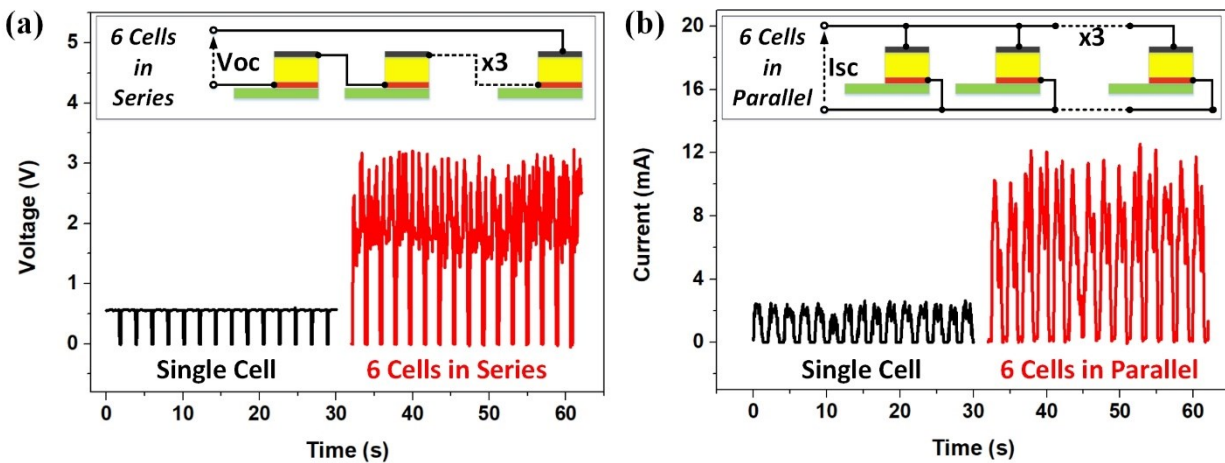
Figure 4.16: Demonstration of application of SLITF-TEG. (a) Enhancing instantaneous voltage by connecting six-unit cells in series. (b) Enhancing instantaneous current by connecting six-unit cells in parallel.

Moreover, the curves of stored energy concerning the load capacitance for various charging times presented in **Figure 4.18a** declare the highest stored energy is obtained at 2 mJ in the 1 mF capacitor after a charging time of ~100 s, suggesting that the optimal capacitance is 1 mF. This amount of energy is sufficiently high for directly powering many electronic devices. We

98

experimentally clarified by powering a commercial light-emitting diode directly from six-unit cells of SLITF-TEG connecting in series (inset image of **Figure 4.18a**). This proves the promising potential of SLITF-TEG as a power source to run electronic devices for various practical applications.
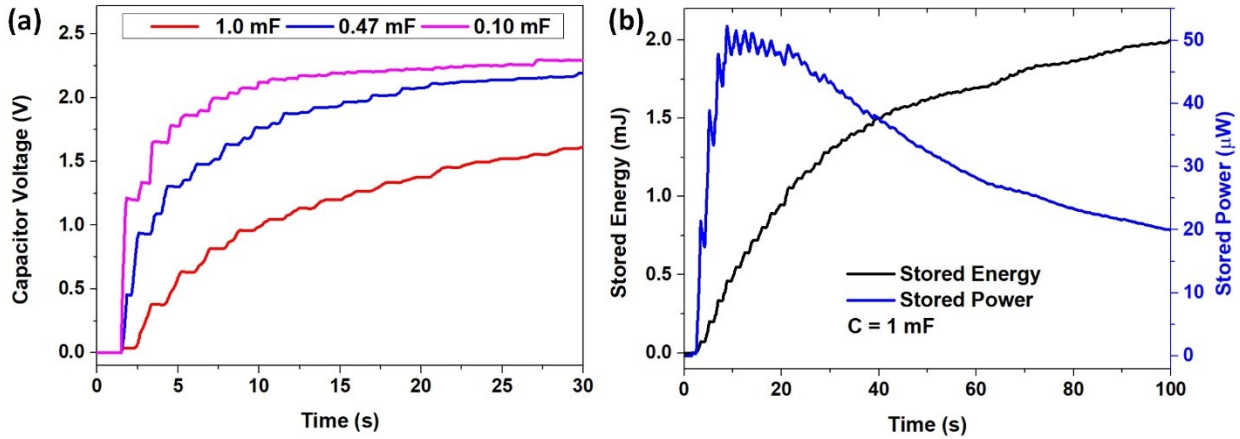
Figure 4.17: (a) Charging behaviors of six-unit cells of SLITF-TEG at different load capacitances. (b) Stored energy-time and stored power-time relationships for a fixed capacitor of 1 mF.

More interestingly, SLITF-TEG not only provides a mechanical-to-electrical conversion concept but also demonstrates a promising potential application as a self-powered sensor based on the dependence of transferred charges during one movement cycle (Qc) and the vibration frequency (f). To validate the sensing capability of the device, we drove the reciprocating motion at various frequencies in a range from 0.21 to 2.22 Hz. The experimental results are presented and discussed above (**Figure 4.10**), where the value of Qc decreases from 6.55 to 0.64 mC/cycle when the applied vibration frequency increases from 0.21 to 2.22 Hz, respectively. After analyzing the data and fitting a curve, we found a strong inversely proportional relationship between the transferred charge during one period of motion and the vibration frequency. The fitting curve can be described by a simple inverse function equation

$$Qc = K.\frac{1}{f} \qquad (4.2)$$

where K is the constant of proportionality, as presented in **Figure 4.18b**. The data followed an inverse power function with a constant K of 1.4587 and a high coefficient of determination R^2 of 0.99, indicating a high level of accuracy and the potential application of this function in determining the vibration frequency and then sliding velocity.
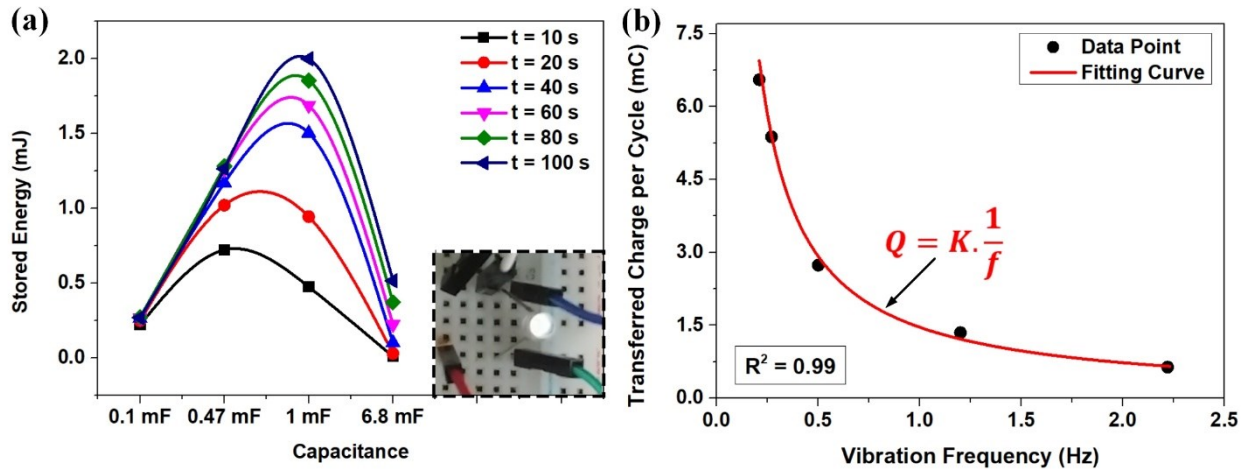
Figure 4.18: Demonstration of application of SLITF-TEG. (a) Stored energy concerning the load capacitance for various charging times. Inset image: a light-emitting diode powered by six-unit cells in series. (b) Inverse regression analysis between the transferred charge and the frequency of the reciprocating motion.

4. Conclusion

In summary, this study has demonstrated the effectiveness of the liquid-solid interface-treated foam triboelectric generator (SLITF-TEG) in converting mechanical energy into DC power. The SLITF-TEG utilizes cellulose-water interface-treated foam as an active layer and generates electricity through a combination of contact electrification due to the sliding friction and the direct charge transfer between two electrodes with different work functions. The research systematically examined the impacts of working parameters and material selection on the SLITF-TEG 's output performance. The results highlight the significant influence of triboelectric material properties on current output, while voltage output is dependent on the materials of the electrode pairs. Under optimized conditions, a single SLITF-TEG can produce DC power with a remarkable current density of 3.57 A/m^2. By connecting multiple unit cells of SLITF-TEG in series and parallel, it becomes possible to increase the maximum voltage and current outputs, making the device suitable for powering electronic devices in various practical applications. Moreover, the SLITF-TEG exhibits a strong inversely proportional relationship between the transferred charge of one movement cycle and the vibration frequency ($R^2 = 0.99$), indicating its potential as an efficient approach for mechanical energy harvesting and self-powered sensor development.

CHAPTER V – CONCLUSION AND FUTURE WORK

1. Conclusion

The thesis carries out extensive research on the conversion of mechanical energy to electrical energy based on triboelectricity. *Chapter I* provides a comprehensive overview of fundamental theories, basic principles, structural designs, affecting factors, and applications of the FluTENG, encompassing both water-based and air-based energy systems. In this chapter, the recent progress of self-powered sensors based on the FluTENGs is reviewed, with discussions on their pros and cons. The chapter emphasizes the need to address challenges related to optimizing structural design, material selection, charge generation, and collection methods to efficiently convert mechanical energy into DC power. It also highlights the importance of achieving higher power and current densities for enhanced energy harvesting and sensitivity. This chapter lays the groundwork for the innovative energy harvesting and sensing technologies proposed in the subsequent chapters.

This thesis proposes an innovative method for harvesting mechanical energy by harnessing the combined effects of triboelectrification and direct charge transfer between two metal contacts. This approach deviates from the traditional TENGs, which rely on the electrostatic induction process for energy collection. The device consists of a dielectric layer, a water-treated cellulose foam as the active layer (WTCF), and two metal contacts. As the active layer undergoes continuous reciprocating motion, it generates electrical energy with pulsed DC characteristics. The energy conversion process involves three main steps: (1) Charge generation through the triboelectric effect due to friction energy; (2) Charge separation as generated charges are separated under the built-in electric field developed between two metal contacts through the hydrogen-bonded network inside the active layer; and (3) Charge flow between the electrodes in one orientation, resulting in the unidirectional flow of output electrons in the external circuit, ultimately achieving DC power generation.

In *Chapters II* and *III*, this thesis introduces and tests two original demonstrations in the realms of energy harvesting and sensing technologies. The setup employed in these chapters involves two parallel metal contacts on a dielectric layer, designed to capture electricity generated by the sliding of the WTCF layer, operating in a freestanding mode. Several unique aspects stand out in terms of theory, device structure, and applications:

1. Systematic study: the thesis thoroughly examines various physical characteristics to identify critical parameters for material selection in triboelectrification and the optimization of structural designs.

2. Stimuli analysis: It investigates and analyzes different physical and chemical stimuli, including sliding velocity, pressure, ion concentration, and water absorption, as key factors influencing the device's performance.

3. Multistimuli detection: The device can detect multiple input stimuli based on the correlation between the output signals, particularly the current output, and the applied stimuli.

4. Power generation: The device produces sufficient energy to power electronic devices, showcasing its potential as a reliable power source.

5. Unified energy harvesting and sensing: The combination of energy harvesting and sensing technologies within a single device holds significant promise for the development of self-powered sensing systems.

For more details, in *Chapter II,* the device exhibits impressive performance characteristics, including a current density of around 0.75 A/m^2 and an induced voltage ranging from 0.48 V to 0.9 V, displaying consistent DC characteristics. It also demonstrates remarkable accuracy in measuring ion concentration in aqueous solutions, achieving a high correlation coefficient (R^2=0.996). Additionally, the potential for increasing the output voltage and current is explored by connecting multiple unit cells in series and parallel configurations.

In *Chapter III*, the device successfully integrates mechanical energy harvesting with multifunctional sensing, showcasing its capabilities as a self-powered multifunctional sensor. The sensing technology reveals strong linear relationships between the output current density and various stimuli, including pressure, sliding velocity, water absorption, and ion concentrations, consistently exceeding a correlation coefficient of 0.99. To operate in a self-powered mode, connecting four-unit cells in series can yield a peak voltage of 2 V. The generated energy can be stored in a capacitor and effectively powers a commercial calculator, offering the potential to eliminate the need for an external power source.

In *Chapter IV*, an effective method for enhancing the device's output performance through innovative structural design is introduced and demonstrated. This newly designed device features

a metal contact attached to the WTCF, moving in tandem as the active layer, while the other metal contact is situated on the dielectric layer. This configuration departs from the freestanding mode of operation in *Chapters II* and *III,* adopting a new sliding mode of operation. As a result, the device achieves a significant boost in output performance, reaching an ultrahigh level of current density, surpassing amperes per meter squared. Specifically, the maximum instantaneous current and power densities increase to 3.57 A/m^2 and 174 mW/m^2, respectively.

2. Future work

The current cellulose-based TEGs have made significant progress compared to traditional TENGs, but there are still challenges to overcome. These include low electrical output and relatively low voltage outputs (around 0.5-0.9 V), which can be inconvenient for powering electronic devices requiring higher voltages. Additionally, these devices have been manually fabricated for small-scale testing, and there is a need for advancements to enable large-scale production. Material selection is crucial for improving device durability and environmental suitability, presenting a challenge for current C-TEGs. Standardized comparison methods are also needed for sustainable development in this field.

The future direction of research focuses on:

1. Developing a universal energy harvesting system capable of converting various forms of mechanical energy from natural and environmental sources, such as human movements, wind, waves, raindrops, transportation, and vibrations.
2. Creating multifunctional sensing systems that can detect and monitor physical, chemical, and biological information from diverse environments.
3. Designing self-charging power sources, such as mechano-electrochemical supercapacitors and packaging, to provide energy for electronics, hydrogen production systems, and smart city applications.
4. Designing self-powered smart sensors for integration into smart vehicles, intelligent transportation, healthcare monitoring, and human-machine interaction systems.
To address these challenges, future work should focus on:

1. Enhancing electrical outputs by increasing contact area, charge density, and potential difference, as well as improving energy storage and utilization through power and energy management units.

2. Tackling industrialization and manufacturing issues by creating adaptable infrastructure, simplifying materials and processing steps, and achieving cost-efficiency and versatile designs.

3. Ensuring environmental suitability by improving materials for extreme conditions, enhancing environmental durability, and developing methods to estimate unpredictable conditions like corrosion and wear.

4. Implement standardization by establishing comprehensive measurement and comparison methods for output performance and efficiency, facilitating standardized evaluation of progress in the field.
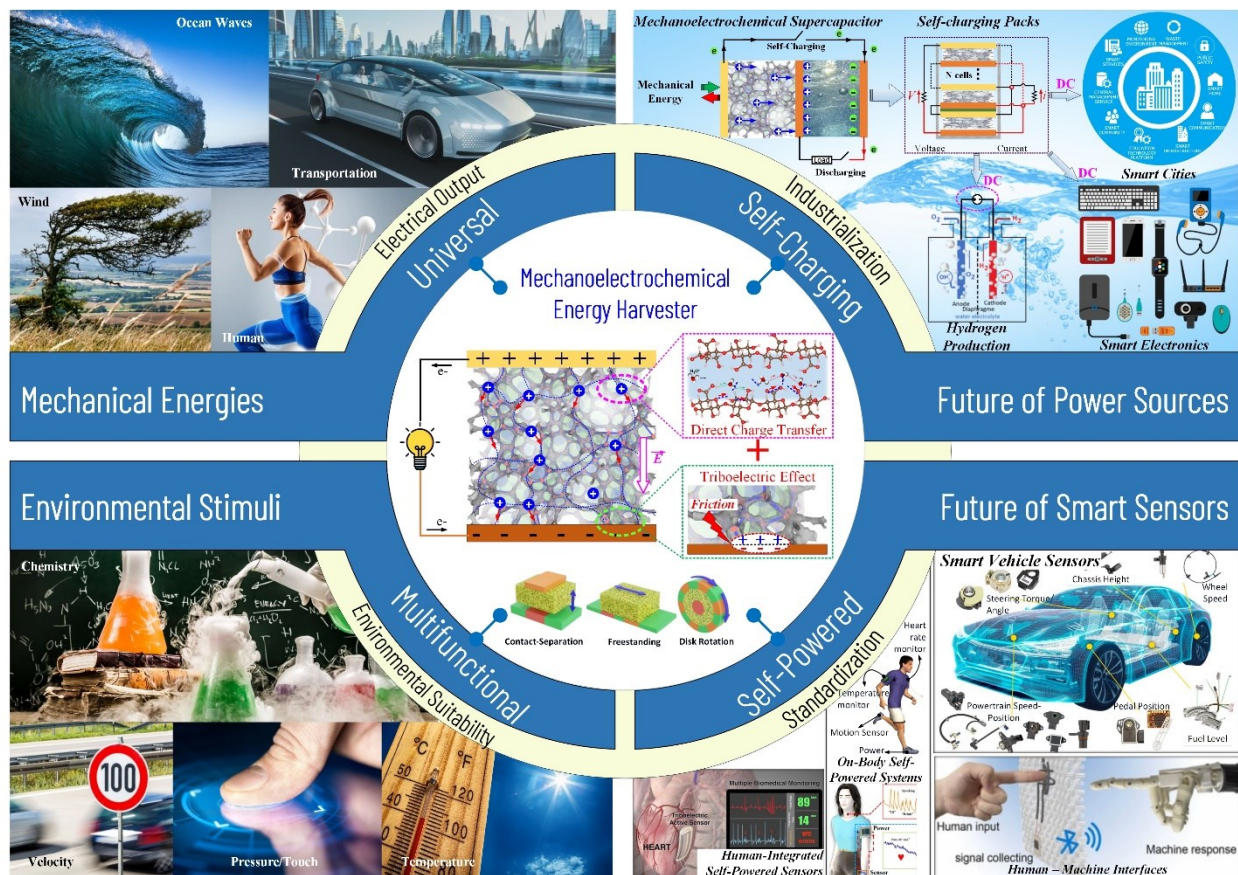
Figure 5.1: Schematic diagram showing the overview of the future direction of research.

Publications

[1]   **Q.-T. Nguyen**, C.-D. Le, D.-L. Vu, T.-H. Nguyen, K. K. Ahn, and S. Ganachari, "High Output Direct-Current Nanogenerators Based on Charge Redistribution at Wet Cellulose/Metal Contact Interfaces," International Journal of Energy Research, vol. 2023, pp. 1-12, 2023.

[2]   **Q. T. Nguyen**, D. L. Vu, C. D. Le, and K. K. Ahn, "Recent Progress in Self-Powered Sensors Based on Liquid-Solid Triboelectric Nanogenerators," Sensors (Basel), vol. 23, no. 13, Jun 25 2023.

[3]   **Q. T. Nguyen**, D. L. Vu, C. D. Le, and K. K. Ahn, "Enhancing the Performance of Triboelectric Generator: A Novel Approach Using Solid-Liquid Interface-Treated Foam and Metal Contacts," Polymers (Basel), vol. 15, no. 10, May 20 2023.

[4]   D. L. Vu, C. D. Le, **Q. T. Nguyen**, K. K. Ahn, and P. K. Kulriya, "Driving the Polyvinylidene Fluoride Crystallization via Surface Functionalization of Ferromagnetic Nanoparticles for Liquid-Solid Triboelectric Nanogenerator Enhancement," International Journal of Energy Research, vol. 2023, pp. 1-11, 2023.

[5]   **Q. T. Nguyen**, C. P. Vo, T. H. Nguyen, and K. K. Ahn, "A Direct-Current Triboelectric Nanogenerator Energy Harvesting System Based on Water Electrification for Self-Powered Electronics," Applied Sciences, vol. 12, no. 5, 2022.

[6]   **Q.-T. Nguyen** and K.-K. K. Ahn, "Fluid-Based Triboelectric Nanogenerators: A Review of Current Status and Applications," International Journal of Precision Engineering and Manufacturing-Green Technology, vol. 8, no. 3, pp. 1043-1060, 2020.

References

[1]   C. Xu, Y. Song, M. Han, and H. Zhang, "Portable and wearable self-powered systems based on emerging energy harvesting technology," *Microsyst Nanoeng,* vol. 7, p. 25, 2021.

[2]   A. Raj and D. Steingart, "Review—Power Sources for the Internet of Things," *Journal of The Electrochemical Society,* vol. 165, no. 8, pp. B3130-B3136, 2018.

[3]   S. Zhang *et al.*, "Current advances and challenges in nanosheet-based wearable power supply devices," *iScience,* vol. 24, no. 12, p. 103477, Dec 17 2021.

[4]   P. K. Annamalai, A. K. Nanjundan, D. P. Dubal, and J. B. Baek, "An Overview of Cellulose-Based Nanogenerators," *Advanced Materials Technologies,* vol. 6, no. 3, 2021.

[5]   Z. Sun *et al.*, "Emerging design principles, materials, and applications for moisture-enabled electric generation," *eScience,* vol. 2, no. 1, pp. 32-46, 2022.

[6]   J. Tan *et al.*, "Self-sustained electricity generator driven by the compatible integration of ambient moisture adsorption and evaporation," *Nat Commun,* vol. 13, no. 1, p. 3643, Jun 25 2022.

[7]   T. G. Yun, J. Bae, A. Rothschild, and I. D. Kim, "Transpiration Driven Electrokinetic Power Generator," *ACS Nano,* vol. 13, no. 11, pp. 12703-12709, Nov 26 2019.

[8]   F.-R. Fan, Z.-Q. Tian, and Z. Lin Wang, "Flexible triboelectric generator," *Nano Energy,* vol. 1, no. 2, pp. 328-334, 2012.

[9]   Z. L. Wang, "Triboelectric Nanogenerators as New Energy Technology for Self-Powered Systems and as Active Mechanical and Chemical Sensors," *ACS Nano,* vol. 7, no. 11, pp. 9533-9557, 2013.

[10]   Z. L. Wang and W. Wu, "Nanotechnology-enabled energy harvesting for self-powered micro-/nanosystems," *Angew Chem Int Ed Engl,* vol. 51, no. 47, pp. 11700-21, Nov 19 2012.

[11]   L. Liu, Q. Shi, J. S. Ho, and C. Lee, "Study of thin film blue energy harvester based on triboelectric nanogenerator and seashore IoT applications," *Nano Energy,* vol. 66, 2019.

[12]   Q.-T. Nguyen and K.-K. K. Ahn, "Fluid-Based Triboelectric Nanogenerators: A Review of Current Status and Applications," *International Journal of Precision Engineering and Manufacturing-Green Technology,* vol. 8, no. 3, pp. 1043-1060, 2020.

[13]   L. Pan *et al.*, "Liquid-FEP-based U-tube triboelectric nanogenerator for harvesting water-wave energy," *Nano Research,* vol. 11, no. 8, pp. 4062-4073, 2018.

[14]   U. Khan and S. W. Kim, "Triboelectric Nanogenerators for Blue Energy Harvesting," *ACS Nano,* vol. 10, no. 7, pp. 6429-32, Jul 26 2016.

[15]   S. Hu *et al.*, "Vibration-Driven Triboelectric Nanogenerator for Vibration Attenuation and Condition Monitoring for Transmission Lines," *Nano Lett,* vol. 22, no. 13, pp. 5584-5591, Jul 13 2022.

[16]   Y. Wang *et al.*, "A humidity resistant and high performance triboelectric nanogenerator enabled by vortex-induced vibration for scavenging wind energy," *Nano Research,* vol. 15, no. 4, pp. 3246-3253, 2021.

[17]   H. Zhang *et al.*, "Triboelectric Nanogenerator for Harvesting Vibration Energy in Full Space and as Self-Powered Acceleration Sensor," *Advanced Functional Materials,* vol. 24, no. 10, pp. 1401-1407, 2014.

[18]   Z. Lin *et al.*, "Super-robust and frequency-multiplied triboelectric nanogenerator for efficient harvesting water and wind energy," *Nano Energy,* vol. 64, 2019.

[19]   X. Fan *et al.*, "Triboelectric-electromagnetic hybrid nanogenerator driven by wind for self-powered wireless transmission in Internet of Things and self-powered wind speed sensor," *Nano Energy,* 2019.

[20]   T. Zhao, S. Cao, S. Yang, R. Guo, S. Sang, and H. Zhang, "A self-powered counter/timer based on a clock pointer-like frequency-tunable triboelectric nanogenerator for wind speed detecting," *Nano Energy,* vol. 65, 2019.

[21]   P. Cheng *et al.*, "Atmospheric pressure difference driven triboelectric nanogenerator for efficiently harvesting ocean wave energy," *Nano Energy,* vol. 54, pp. 156-162, 2018.

[22]   N. Wang *et al.*, "Kelp-inspired biomimetic triboelectric nanogenerator boosts wave energy harvesting," *Nano Energy,* vol. 55, pp. 541-547, 2019.

[23]   W. Liu *et al.*, "Torus structured triboelectric nanogenerator array for water wave energy harvesting," *Nano Energy,* vol. 58, pp. 499-507, 2019.

[24]   M. Olsen, R. Zhang, J. Ortegren, H. Andersson, Y. Yang, and H. Olin, "Frequency and voltage response of a wind-driven fluttering triboelectric nanogenerator," *Sci Rep,* vol. 9, no. 1, p. 5543, Apr 3 2019.

[25]   J. Wang *et al.*, "Self-Powered Wind Sensor System for Detecting Wind Speed and Direction Based on a Triboelectric Nanogenerator," *ACS Nano,* vol. 12, no. 4, pp. 3954-3963, Apr 24 2018.

[26]   P. Wang *et al.*, "An Ultra-Low-Friction Triboelectric-Electromagnetic Hybrid Nanogenerator for Rotation Energy Harvesting and Self-Powered Wind Speed Sensor," *ACS Nano,* vol. 12, no. 9, pp. 9433-9440, Sep 25 2018.

[27]   Y. Wu, Y. Hu, Z. Huang, C. Lee, and F. Wang, "Electret-material enhanced triboelectric energy harvesting from air flow for self-powered wireless temperature sensor network," *Sensors and Actuators A: Physical,* vol. 271, pp. 364-372, 2018.

[28]   L.-b. Huang, W. Xu, G. Bai, M.-C. Wong, Z. Yang, and J. Hao, "Wind energy and blue energy harvesting based on magnetic-assisted noncontact triboelectric nanogenerator," *Nano Energy,* vol. 30, pp. 36-42, 2016.

[29]   A. Ahmed, I. Hassan, M. Hedaya, T. Abo El-Yazid, J. Zu, and Z. L. Wang, "Farms of triboelectric nanogenerators for harvesting wind energy: A potential approach towards green energy," *Nano Energy,* vol. 36, pp. 21-29, 2017.

[30]   X. Liu, K. Zhao, and Y. Yang, "Effective polarization of ferroelectric materials by using a triboelectric nanogenerator to scavenge wind energy," *Nano Energy,* vol. 53, pp. 622-629, 2018.

[31]   M. T. Rahman, M. Salauddin, P. Maharjan, M. S. Rasel, H. Cho, and J. Y. Park, "Natural wind-driven ultra-compact and highly efficient hybridized nanogenerator for self-sustained wireless environmental monitoring system," *Nano Energy,* vol. 57, pp. 256-268, 2019.

[32]   Y. Feng, L. Zhang, Y. Zheng, D. Wang, F. Zhou, and W. Liu, "Leaves based triboelectric nanogenerator (TENG) and TENG tree for wind energy harvesting," *Nano Energy,* vol. 55, pp. 260-268, 2019.

[33]   H. Lin *et al.*, "Angle-shaped triboelectric nanogenerator for harvesting environmental wind energy," *Nano Energy,* vol. 56, pp. 269-276, 2019.

[34]   A. N. Ravichandran, C. Calmes, J. R. Serres, M. Ramuz, and S. Blayac, "Compact and high performance wind actuated venturi triboelectric energy harvester," *Nano Energy,* vol. 62, pp. 449-457, 2019.

[35]   M. Xu *et al.*, "An aeroelastic flutter based triboelectric nanogenerator as a self-powered active wind speed sensor in harsh environment," *Extreme Mechanics Letters,* vol. 15, pp. 122-129, 2017.

[36]   H. Kim, Q. Zhou, D. Kim, and I.-K. Oh, "Flow-induced snap-through triboelectric nanogenerator," *Nano Energy,* vol. 68, 2020.

[37]   F. Yi *et al.*, "Self-Powered Trajectory, Velocity, and Acceleration Tracking of a Moving Object/Body using a Triboelectric Sensor," *Advanced Functional Materials,* vol. 24, no. 47, pp. 7488-7494, 2014.

[38]   L. M. Zhang *et al.*, "Multilayer wavy-structured robust triboelectric nanogenerator for harvesting water wave energy," *Nano Energy,* vol. 22, pp. 87-94, 2016.

[39]   B. D. Chen *et al.*, "Water wave energy harvesting and self-powered liquid-surface fluctuation sensing based on bionic-jellyfish triboelectric nanogenerator," *Materials Today,* vol. 21, no. 1, pp. 88-97, 2018.

[40] S. L. Zhang *et al.*, "Rationally designed sea snake structure based triboelectric nanogenerators for effectively and efficiently harvesting ocean wave energy with minimized water screening effect," *Nano Energy,* vol. 48, pp. 421-429, 2018.

[41] D. Zhang, J. Shi, Y. Si, and T. Li, "Multi-grating triboelectric nanogenerator for harvesting low-frequency ocean wave energy," *Nano Energy,* vol. 61, pp. 132-140, 2019.

[42] Y. Bai *et al.*, "High-performance triboelectric nanogenerators for self-powered, in-situ and real-time water quality mapping," *Nano Energy,* vol. 66, 2019.

[43] P. Cheng *et al.*, "Largely enhanced triboelectric nanogenerator for efficient harvesting of water wave energy by soft contacted structure," *Nano Energy,* vol. 57, pp. 432-439, 2019.

[44] W. Zhong, L. Xu, H. Wang, D. Li, and Z. L. Wang, "Stacked pendulum-structured triboelectric nanogenerators for effectively harvesting low-frequency water wave energy," *Nano Energy,* vol. 66, 2019.

[45] S. Wang *et al.*, "A facile respiration-driven triboelectric nanogenerator for multifunctional respiratory monitoring," *Nano Energy,* vol. 58, pp. 312-321, 2019.

[46] Q. Zhou *et al.*, "High humidity- and contamination-resistant triboelectric nanogenerator with superhydrophobic interface," *Nano Energy,* vol. 57, pp. 903-910, 2019.

[47] Z. Lin *et al.*, "Rationally designed rotation triboelectric nanogenerators with much extended lifetime and durability," *Nano Energy,* vol. 68, 2020.

[48] J. Pei, J. Huang, Z. Huang, and K. Liu, "Liquid flow-induced electricity in carbon nanomaterials," *Sustainable Energy & Fuels,* vol. 3, no. 3, pp. 599-610, 2019.

[49] P. Jiang *et al.*, "Signal Output of Triboelectric Nanogenerator at Oil-Water-Solid Multiphase Interfaces and its Application for Dual-Signal Chemical Sensing," *Adv Mater,* vol. 31, no. 39, p. e1902793, Sep 2019.

[50] D. Choi, D. W. Kim, D. Yoo, K. J. Cha, M. La, and D. S. Kim, "Spontaneous occurrence of liquid-solid contact electrification in nature: Toward a robust triboelectric nanogenerator inspired by the natural lotus leaf," *Nano Energy,* vol. 36, pp. 250-259, 2017.

[51] W. Zhang, P. Wang, K. Sun, C. Wang, and D. Diao, "Intelligently detecting and identifying liquids leakage combining triboelectric nanogenerator based self-powered sensor with machine learning," *Nano Energy,* vol. 56, pp. 277-285, 2019.

[52] X. Zhang, Y. Zheng, D. Wang, Z. U. Rahman, and F. Zhou, "Liquid–solid contact triboelectrification and its use in self-powered nanosensor for detecting organics in water," *Nano Energy,* vol. 30, pp. 321-329, 2016.

[53] Y. Wu *et al.*, "A Self-Powered Triboelectric Nanosensor for PH Detection," *Journal of Nanomaterials,* vol. 2016, p. 6, 2016, Art. no. 5121572.

[54] W. Tang *et al.*, "Liquid-Metal Electrode for High-Performance Triboelectric Nanogenerator at an Instantaneous Energy Conversion Efficiency of 70.6%," *Advanced Functional Materials,* vol. 25, no. 24, pp. 3718-3725, 2015.

[55] M.-L. Seol, S.-B. Jeon, J.-W. Han, and Y.-K. Choi, "Ferrofluid-based triboelectric-electromagnetic hybrid generator for sensitive and sustainable vibration energy harvesting," *Nano Energy,* vol. 31, pp. 233-238, 2017.

[56] Z.-H. Lin, G. Cheng, L. Lin, S. Lee, and Z. L. Wang, "Water–Solid Surface Contact Electrification and its Use for Harvesting Liquid-Wave Energy," *Angewandte Chemie International Edition,* vol. 52, no. 48, pp. 12545-12549, 2013.

[57] X. Li, J. Tao, X. Wang, J. Zhu, C. Pan, and Z. L. Wang, "Networks of High Performance Triboelectric Nanogenerators Based on Liquid–Solid Interface Contact Electrification for Harvesting Low-Frequency Blue Energy," *Advanced Energy Materials,* vol. 8, no. 21, p. 1800705, 2018.

[58]   X. Cui, H. Zhang, S. Cao, Z. Yuan, J. Ding, and S. Sang, "Tube-based triboelectric nanogenerator for self-powered detecting blockage and monitoring air pressure," *Nano Energy,* vol. 52, pp. 71-77, 2018.

[59]   J. Chen *et al.*, "Self-Powered Triboelectric Micro Liquid/Gas Flow Sensor for Microfluidics," *ACS Nano,* vol. 10, no. 8, pp. 8104-8112, 2016/08/23 2016.

[60]   Q. Shi, H. Wang, H. Wu, and C. Lee, "Self-powered triboelectric nanogenerator buoy ball for applications ranging from environment monitoring to water wave energy farm," *Nano Energy,* vol. 40, pp. 203-213, 2017.

[61]   J.-W. Lee and W. Hwang, "Theoretical study of micro/nano roughness effect on water-solid triboelectrification with experimental approach," *Nano Energy,* vol. 52, pp. 315-322, 2018.

[62]   X. Yang, S. Chan, L. Wang, and W. A. Daoud, "Water tank triboelectric nanogenerator for efficient harvesting of water wave energy over a broad frequency range," *Nano Energy,* vol. 44, pp. 388-398, 2018.

[63]   X. Chen *et al.*, "Transparent and stretchable bimodal triboelectric nanogenerators with hierarchical micro-nanostructures for mechanical and water energy harvesting," *Nano Energy,* vol. 64, 2019.

[64]   D. Yoo *et al.*, "Biomimetic anti-reflective triboelectric nanogenerator for concurrent harvesting of solar and raindrop energies," *Nano Energy,* vol. 57, pp. 424-431, 2019.

[65]   X. J. Zhao, S. Y. Kuang, Z. L. Wang, and G. Zhu, "Highly Adaptive Solid-Liquid Interfacing Triboelectric Nanogenerator for Harvesting Diverse Water Wave Energy," *ACS Nano,* vol. 12, no. 5, pp. 4280-4285, May 22 2018.

[66]   P. Dhiman *et al.*, "Harvesting energy from water flow over graphene," *Nano Lett,* vol. 11, no. 8, pp. 3123-7, Aug 10 2011.

[67]   B. Kil Yun, H. Soo Kim, Y. Joon Ko, G. Murillo, and J. Hoon Jung, "Interdigital electrode based triboelectric nanogenerator for effective energy harvesting from water," *Nano Energy,* vol. 36, pp. 233-240, 2017.

[68]   Z. H. Lin, G. Cheng, S. Lee, K. C. Pradel, and Z. L. Wang, "Harvesting water drop energy by a sequential contact-electrification and electrostatic-induction process," *Adv Mater,* vol. 26, no. 27, pp. 4690-6, Jul 16 2014.

[69]   H.-Y. Park, H. K. Kim, Y.-H. Hwang, and D.-M. Shin, "Water-through triboelectric nanogenerator based on Ti-mesh for harvesting liquid flow," *Journal of the Korean Physical Society,* vol. 72, no. 4, pp. 499-503, 2018.

[70]   S. S. Kwak *et al.*, "Triboelectrification-Induced Large Electric Power Generation from a Single Moving Droplet on Graphene/Polytetrafluoroethylene," *ACS Nano,* vol. 10, no. 8, pp. 7297-7302, Aug 23 2016.

[71]   L. E. Helseth, "Electrical energy harvesting from water droplets passing a hydrophobic polymer with a metal film on its back side," *Journal of Electrostatics,* vol. 81, pp. 64-70, 2016.

[72]   T. Kim *et al.*, "Design and optimization of rotating triboelectric nanogenerator by water electrification and inertia," *Nano Energy,* vol. 27, pp. 340-351, 2016.

[73]   T. Kim *et al.*, "Direct-current triboelectric nanogenerator via water electrification and phase control," *Nano Energy,* vol. 52, pp. 95-104, 2018.

[74]   X. Zhang, Y. Zheng, D. Wang, and F. Zhou, "Solid-liquid triboelectrification in smart U-tube for multifunctional sensors," *Nano Energy,* vol. 40, pp. 95-106, 2017.

[75]   D. Choi, S. Lee, S. M. Park, H. Cho, W. Hwang, and D. S. Kim, "Energy harvesting model of moving water inside a tubular system and its application of a stick-type compact triboelectric nanogenerator," *Nano Research,* vol. 8, no. 8, pp. 2481-2491, 2015.

[76]   J. Xiong *et al.*, "Self-restoring, waterproof, tunable microstructural shape memory triboelectric nanogenerator for self-powered water temperature sensor," *Nano Energy,* vol. 61, pp. 584-593, 2019.

[77]   J. Tan, J. Duan, Y. Zhao, B. He, and Q. Tang, "Generators to harvest ocean wave energy through electrokinetic principle," *Nano Energy,* vol. 48, pp. 128-133, 2018.

[78]   Y. Liu, Y. Zheng, T. Li, D. Wang, and F. Zhou, "Water-solid triboelectrification with self-repairable surfaces for water-flow energy harvesting," *Nano Energy,* vol. 61, pp. 454-461, 2019.

[79]   H. Cho *et al.*, "Toward sustainable output generation of liquid–solid contact triboelectric nanogenerators: The role of hierarchical structures," *Nano Energy,* vol. 56, pp. 56-64, 2019.

[80]   J. Nie, Z. Wang, Z. Ren, S. Li, X. Chen, and Z. Lin Wang, "Power generation from the interaction of a liquid droplet and a liquid membrane," *Nat Commun,* vol. 10, no. 1, p. 2264, May 22 2019.

[81]   C. R. S. Rodrigues, C. A. S. Alves, J. Puga, A. M. Pereira, and J. O. Ventura, "Triboelectric driven turbine to generate electricity from the motion of water," *Nano Energy,* vol. 30, pp. 379-386, 2016.

[82]   R. Hinchet *et al.*, "Transcutaneous ultrasound energy harvesting using capacitive triboelectric technology," *Science,* vol. 365, no. 6452, pp. 491–494, 2019.

[83]   S. S. Kwak *et al.*, "Butylated melamine formaldehyde as a durable and highly positive friction layer for stable, high output triboelectric nanogenerators," *Energy & Environmental Science,* vol. 12, no. 10, pp. 3156-3163, 2019.

[84]   J. Kim *et al.*, "High Permittivity CaCu3Ti4O12 Particle-Induced Internal Polarization Amplification for High Performance Triboelectric Nanogenerators," *Advanced Energy Materials,* vol. 10, no. 9, 2020.

[85]   W. Seung *et al.*, "Boosting Power-Generating Performance of Triboelectric Nanogenerators via Artificial Control of Ferroelectric Polarization and Dielectric Properties," *Advanced Energy Materials,* vol. 7, no. 2, 2017.

[86]   M. Xu *et al.*, "A highly-sensitive wave sensor based on liquid-solid interfacing triboelectric nanogenerator for smart marine equipment," *Nano Energy,* vol. 57, pp. 574-580, 2019.

[87]   Q. Shi, H. Wang, T. Wang, and C. Lee, "Self-powered liquid triboelectric microfluidic sensor for pressure sensing and finger motion monitoring applications," *Nano Energy,* vol. 30, pp. 450-459, 2016.

[88]   M. Wang *et al.*, "Air-Flow-Driven Triboelectric Nanogenerators for Self-Powered Real-Time Respiratory Monitoring," *ACS Nano,* vol. 12, no. 6, pp. 6156-6162, Jun 26 2018.

[89]   Z. L. Wang, "Triboelectric nanogenerators as new energy technology and self-powered sensors - principles, problems and perspectives," *Faraday Discuss,* vol. 176, pp. 447-58, 2014.

[90]   S.-H. Kwon *et al.*, "An effective energy harvesting method from a natural water motion active transducer," *Energy Environ. Sci.,* vol. 7, no. 10, pp. 3279-3283, 2014.

[91]   G. Cheng, Z.-H. Lin, Z.-l. Du, and Z. L. Wang, "Simultaneously Harvesting Electrostatic and Mechanical Energies from Flowing Water by a Hybridized Triboelectric Nanogenerator," *ACS Nano,* vol. 8, no. 2, pp. 1932-1939, 2014/02/25 2014.

[92]   L. Zhang *et al.*, "Self-powered all-in-one fluid sensor textile with enhanced triboelectric effect on all-immersed dendritic liquid-solid interface," *ACS Appl Mater Interfaces,* vol. 10, no. 36, pp. 30819-30826, Sep 12 2018.

[93]   S.-B. Jeon, M.-L. Seol, D. Kim, S.-J. Park, and Y.-K. Choi, "Self-powered ion concentration sensor with triboelectricity from liquid-solid contact electrification," *Advanced Electronic Materials,* vol. 2, no. 5, p. 1600006, 2016.

[94]   W. Kim, D. Choi, J.-Y. Kwon, and D. Choi, "A self-powered triboelectric microfluidic system for liquid sensing," *Journal of Materials Chemistry A,* vol. 6, no. 29, pp. 14069-14076, 2018.

[95]   F. Yi *et al.*, "A highly shape-adaptive, stretchable design based on conductive liquid for energy harvesting and self-powered biomechanical monitoring," *Sci Adv,* vol. 2, no. 6, p. e1501624, Jun 2016.

[96]   S. Cui, Y. Zheng, T. Zhang, D. Wang, F. Zhou, and W. Liu, "Self-powered ammonia nanosensor based on the integration of the gas sensor and triboelectric nanogenerator," *Nano Energy,* vol. 49, pp. 31-39, 2018.

[97]   H. Wang, H. Wu, D. Hasan, T. He, Q. Shi, and C. Lee, "Self-powered dual-mode amenity sensor based on the water-air triboelectric nanogenerator," *ACS Nano,* vol. 11, no. 10, pp. 10337-10346, Oct 24 2017.

[98]   C. Zhang, T. Zhou, W. Tang, C. Han, L. Zhang, and Z. L. Wang, "Rotating-Disk-Based Direct-Current Triboelectric Nanogenerator," *Advanced Energy Materials,* vol. 4, no. 9, 2014.

[99]   D. Liu *et al.*, "Hugely Enhanced Output Power of Direct-Current Triboelectric Nanogenerators by Using Electrostatic Breakdown Effect," *Advanced Materials Technologies,* vol. 5, no. 7, 2020.

[100]   L. Zhou *et al.*, "Rationally Designed Dual-Mode Triboelectric Nanogenerator for Harvesting Mechanical Energy by Both Electrostatic Induction and Dielectric Breakdown Effects," *Advanced Energy Materials,* vol. 10, no. 24, 2020.

[101]   S. Li *et al.*, "A Fully Self-Powered Vibration Monitoring System Driven by Dual-Mode Triboelectric Nanogenerators," *ACS Nano,* vol. 14, no. 2, pp. 2475-2482, Feb 25 2020.

[102]   G. Qiao, J. Wang, X. Yu, R. Jia, T. Cheng, and Z. L. Wang, "A bidirectional direct current triboelectric nanogenerator with the mechanical rectifier," *Nano Energy,* vol. 79, 2021.

[103]   J. Zhu *et al.*, "Continuous direct current by charge transportation for next-generation IoT and real-time virtual reality applications," *Nano Energy,* vol. 73, 2020.

[104]   X. Y. Di Liu, Hengyu Guo, Linglin Zhou, Xinyuan Li, Chunlei Zhang, and Z. L. W. Jie Wang, "A constant current triboelectric nanogenerator arising from electrostatic breakdown," *Science Advances,* vol. 5, no. 4, p. EAAV6437, 2019.

[105]   J. Wang *et al.*, "Direct-Current Rotary-Tubular Triboelectric Nanogenerators Based on Liquid-Dielectrics Contact for Sustainable Energy Harvesting and Chemical Composition Analysis," *ACS Nano,* vol. 13, no. 2, pp. 2587-2598, Feb 26 2019.

[106]   J. Wang *et al.*, "Cylindrical Direct-Current Triboelectric Nanogenerator with Constant Output Current," *Advanced Energy Materials,* vol. 10, no. 10, 2020.

[107]   C. Chen *et al.*, "Direct Current Fabric Triboelectric Nanogenerator for Biomotion Energy Harvesting," *ACS Nano,* vol. 14, no. 4, pp. 4585-4594, Apr 28 2020.

[108]   H. Ryu, J. H. Lee, U. Khan, S. S. Kwak, R. Hinchet, and S.-W. Kim, "Sustainable direct current powering a triboelectric nanogenerator via a novel asymmetrical design," *Energy & Environmental Science,* vol. 11, no. 8, pp. 2057-2063, 2018.

[109]   Z. Zhao *et al.*, "Rationally patterned electrode of direct-current triboelectric nanogenerators for ultrahigh effective surface charge density," *Nat Commun,* vol. 11, no. 1, p. 6186, Dec 3 2020.

[110]   J. Xu, Z. Xie, H. Yue, Y. Lu, and F. Yang, "A triboelectric multifunctional sensor based on the controlled buckling structure for motion monitoring and bionic tactile of soft robots," *Nano Energy,* vol. 104, 2022.

[111]   S. Farhad, M. Saffar-Avval, and M. Younessi-Sinaki, "Efficient design of feedwater heaters network in steam power plants using pinch technology and exergy analysis," *International Journal of Energy Research,* vol. 32, no. 1, pp. 1-11, 2008.

[112]   N. Kaur and K. Pal, "Triboelectric Nanogenerators for Mechanical Energy Harvesting," *Energy Technology,* vol. 6, no. 6, pp. 958-997, 2018.

[113]   S. Priya, "Advances in energy harvesting using low profile piezoelectric transducers," *Journal of Electroceramics,* vol. 19, no. 1, pp. 167-184, 2007.

[114] C. Zhao *et al.*, "Hybrid piezo/triboelectric nanogenerator for highly efficient and stable rotation energy harvesting," *Nano Energy,* vol. 57, pp. 440-449, 2019.

[115] S. Chamanian, H. Uluşan, Ö. Zorlu, S. Baghaee, E. Uysal-Biyikoglu, and H. Külah, "Wearable battery-less wireless sensor network with electromagnetic energy harvesting system," *Sensors and Actuators A: Physical,* vol. 249, pp. 77-84, 2016.

[116] C. Hao *et al.*, "Two-dimensional triboelectric-electromagnetic hybrid nanogenerator for wave energy harvesting," *Nano Energy,* vol. 58, pp. 147-157, 2019.

[117] S. Pan and Z. Zhang, "Fundamental theories and basic principles of triboelectric effect: A review," *Friction,* vol. 7, no. 1, pp. 2-17, 2018.

[118] S. Wang, L. Lin, and Z. L. Wang, "Triboelectric nanogenerators as self-powered active sensors," *Nano Energy,* vol. 11, pp. 436-462, 2015.

[119] S. Bilgen, K. Kaygusuz, and A. Sari, "Renewable Energy for a Clean and Sustainable Future," *Energy Sources,* vol. 26, no. 12, pp. 1119-1129, 2004.

[120] Y. Liu *et al.*, "Integrating a Silicon Solar Cell with a Triboelectric Nanogenerator via a Mutual Electrode for Harvesting Energy from Sunlight and Raindrops," *ACS Nano,* vol. 12, no. 3, pp. 2893-2899, Mar 27 2018.

[121] H. Yong, J. Chung, D. Choi, D. Jung, M. Cho, and S. Lee, "Highly reliable wind-rolling triboelectric nanogenerator operating in a wide wind speed range," *Sci Rep,* vol. 6, p. 33977, Sep 22 2016.

[122] S.-J. Park *et al.*, "Self-sustainable wind speed sensor system with omni-directional wind based triboelectric generator," *Nano Energy,* vol. 55, pp. 115-122, 2019.

[123] M. Taghavi, A. Sadeghi, B. Mazzolai, L. Beccai, and V. Mattoli, "Triboelectric-based harvesting of gas flow energy and powerless sensing applications," *Applied Surface Science,* vol. 323, pp. 82-87, 2014.

[124] Z. Zhao *et al.*, "Freestanding Flag-Type Triboelectric Nanogenerator for Harvesting High-Altitude Wind Energy from Arbitrary Directions," *ACS Nano,* vol. 10, no. 2, pp. 1780-7, Feb 23 2016.

[125] Z.-H. Lin *et al.*, "A Self-Powered Triboelectric Nanosensor for Mercury Ion Detection," *Angewandte Chemie International Edition,* vol. 52, no. 19, pp. 5065-5069, 2013.

[126] Z. Wen *et al.*, "Blow-driven triboelectric nanogenerator as an active alcohol breath analyzer," *Nano Energy,* vol. 16, pp. 38-46, 2015.

[127] J. H. Lee, S. Kim, T. Y. Kim, U. Khan, and S.-W. Kim, "Water droplet-driven triboelectric nanogenerator with superhydrophobic surfaces," *Nano Energy,* vol. 58, pp. 579-584, 2019.

[128] G. Zhu, J. Chen, T. Zhang, Q. Jing, and Z. L. Wang, "Radial-arrayed rotary electrification for high performance triboelectric generator," *Nat Commun,* vol. 5, p. 3426, Mar 4 2014.

[129] W. Yang *et al.*, "3D Stack Integrated Triboelectric Nanogenerator for Harvesting Vibration Energy," *Advanced Functional Materials,* vol. 24, no. 26, pp. 4090-4096, 2014.

[130] A. F. Diaz and R. M. Felix-Navarro, "A semi-quantitative tribo-electric series for polymeric materials: the influence of chemical structure and properties," *Journal of Electrostatics,* vol. 62, no. 4, pp. 277-290, 2004.

[131] Y. Zi, S. Niu, J. Wang, Z. Wen, W. Tang, and Z. L. Wang, "Standards and figure-of-merits for quantifying the performance of triboelectric nanogenerators," *Nat Commun,* vol. 6, p. 8376, Sep 25 2015.

[132] X. Li *et al.*, "Long-Lifetime Triboelectric Nanogenerator Operated in Conjunction Modes and Low Crest Factor," *Advanced Energy Materials,* vol. 10, no. 7, 2020.

[133] L. Zhou, D. Liu, J. Wang, and Z. L. Wang, "Triboelectric nanogenerators: Fundamental physics and potential applications," *Friction,* vol. 8, no. 3, pp. 481-506, 2020.

[134] Z. L. Wang and A. C. Wang, "On the origin of contact-electrification," *Materials Today,* vol. 30, pp. 34-51, 2019.

[135]   Z. H. Lin, G. Cheng, L. Lin, S. Lee, and Z. L. Wang, "Water-solid surface contact electrification and its use for harvesting liquid-wave energy," *Angew Chem Int Ed Engl,* vol. 52, no. 48, pp. 12545-9, Nov 25 2013.

[136]   S. A. Nahian, R. K. Cheedarala, and K. K. Ahn, "A study of sustainable green current generated by the fluid-based triboelectric nanogenerator (FluTENG) with a comparison of contact and sliding mode," *Nano Energy,* vol. 38, pp. 447-456, 2017.

[137]   T. Huang *et al.*, "A Multifunction Freestanding Liquid-Solid Triboelectric Nanogenerator Based on Low-Frequency Mechanical Sloshing," *ACS Appl Mater Interfaces,* vol. 14, no. 49, pp. 54716-54724, Dec 14 2022.

[138]   Y. S. Guang Zhu, Peng Bai, Jun Chen, Qingshen Jing, Weiqing Yang, and Zhong Lin Wang, "Harvesting Water Wave Energy by Asymmetric Screening of Electrostatic Charges on a Nanostructured Hydrophobic Thin-Film Surface," *ACS Nano,* vol. 8, no. 6, pp. 6031-6037, 2014.

[139]   S. Jang *et al.*, "Monocharged electret based liquid-solid interacting triboelectric nanogenerator for its boosted electrical output performance," *Nano Energy,* vol. 70, 2020.

[140]   C.-D. Le, C.-P. Vo, T.-H. Nguyen, D.-L. Vu, and K. K. Ahn, "Liquid-solid contact electrification based on discontinuous-conduction triboelectric nanogenerator induced by radially symmetrical structure," *Nano Energy,* vol. 80, 2021.

[141]   C. Li, X. Liu, D. Yang, and Z. Liu, "Triboelectric nanogenerator based on a moving bubble in liquid for mechanical energy harvesting and water level monitoring," *Nano Energy,* vol. 95, 2022.

[142]   J. Yu and T. Ma, "Triboelectricity-based self-charging droplet capacitor for harvesting low-level ambient energy," *Nano Energy,* vol. 74, 2020.

[143]   Y. Lu *et al.*, "Polarized Water Driven Dynamic PN Junction-Based Direct-Current Generator," *Research (Wash D C),* vol. 2021, p. 7505638, 2021.

[144]   J. Zhang, S. Lin, M. Zheng, and Z. L. Wang, "Triboelectric Nanogenerator as a Probe for Measuring the Charge Transfer between Liquid and Solid Surfaces," *ACS Nano,* vol. 15, no. 9, pp. 14830-14837, Sep 28 2021.

[145]   X. Li, J. Tao, X. Wang, J. Zhu, C. Pan, and Z. L. Wang, "Networks of High Performance Triboelectric Nanogenerators Based on Liquid-Solid Interface Contact Electrification for Harvesting Low-Frequency Blue Energy," *Advanced Energy Materials,* vol. 8, no. 21, 2018.

[146]   L. Yang, Y. Wang, Y. Guo, W. Zhang, and Z. Zhao, "Robust Working Mechanism of Water Droplet-Driven Triboelectric Nanogenerator: Triboelectric Output versus Dynamic Motion of Water Droplet," *Advanced Materials Interfaces,* vol. 6, no. 24, 2019.

[147]   Q. T. Nguyen, C. P. Vo, T. H. Nguyen, and K. K. Ahn, "A Direct-Current Triboelectric Nanogenerator Energy Harvesting System Based on Water Electrification for Self-Powered Electronics," *Applied Sciences,* vol. 12, no. 5, 2022.

[148]   L. Wang *et al.*, "Harvesting energy from high-frequency impinging water droplets by a droplet-based electricity generator," *EcoMat,* vol. 3, no. 4, 2021.

[149]   Z. Li *et al.*, "A droplet-based electricity generator for large-scale raindrop energy harvesting," *Nano Energy,* vol. 100, 2022.

[150]   K. Munirathinam, D.-S. Kim, A. Shanmugasundaram, J. Park, Y.-J. Jeong, and D.-W. Lee, "Flowing water-based tubular triboelectric nanogenerators for sustainable green energy harvesting," *Nano Energy,* vol. 102, 2022.

[151]   X. Li, T. H. Lau, D. Guan, and Y. Zi, "A universal method for quantitative analysis of triboelectric nanogenerators," *Journal of Materials Chemistry A,* vol. 7, no. 33, pp. 19485-19494, 2019.

[152]   Y. Wang, Y. Yang, and Z. L. Wang, "Triboelectric nanogenerators as flexible power sources," *npj Flexible Electronics,* vol. 1, no. 1, 2017.

[153]   R. K. Cheedarala, L. C. Duy, and K. K. Ahn, "Double characteristic BNO-SPI-TENGs for robust contact electrification by vertical contact separation mode through ion and electron charge transfer," *Nano Energy,* vol. 44, pp. 430-437, 2018.

[154]   Q. Shi, T. He, and C. Lee, "More than energy harvesting – Combining triboelectric nanogenerator and flexible electronics technology for enabling novel micro-/nano-systems," *Nano Energy,* vol. 57, pp. 851-871, 2019.

[155]   X. J. Zhao *et al.*, "Biocide-free antifouling on insulating surface by wave-driven triboelectrification-induced potential oscillation," *Advanced Materials Interfaces,* vol. 3, no. 17, p. 1600187, 2016.

[156]   D. L. Vu and K. K. Ahn, "Triboelectric enhancement of polyvinylidene fluoride membrane using magnetic nanoparticle for water-based energy harvesting," *Polymers (Basel),* vol. 14, no. 8, p. 1547, Apr 11 2022.

[157]   C.-D. Le, C.-P. Vo, T.-H. Nguyen, D.-L. Vu, and K. K. Ahn, "Liquid-solid contact electrification based on discontinuous-conduction triboelectric nanogenerator induced by radially symmetrical structure," *Nano Energy,* vol. 80, p. 105571, 2021/02/01/ 2021.

[158]   L. E. Helseth and X. D. Guo, "Contact electrification and energy harvesting using periodically contacted and squeezed water droplets," *Langmuir,* vol. 31, no. 10, pp. 3269-3276, 2015/03/17 2015.

[159]   Z. H. Lin, G. Cheng, W. Z. Wu, K. C. Pradel, and Z. L. Wang, "Dual-Mode Triboelectric Nanogenerator for Harvesting Water Energy and as a Self-Powered Ethanol Nanosensor," (in English), *Acs Nano,* vol. 8, no. 6, pp. 6440-6448, Jun 2014.

[160]   J. Bardeen, "Electrical Conductivity of Metals," *Journal of Applied Physics,* vol. 11, no. 2, pp. 88-111, 1940.

[161]   Y. Yang, J. Park, S. H. Kwon, and Y. S. Kim, "Fluidic Active Transducer for Electricity Generation," *Sci Rep,* vol. 5, p. 15695, Oct 29 2015.

[162]   Y. Song *et al.*, "Highly Compressible Integrated Supercapacitor–Piezoresistance-Sensor System with CNT–PDMS Sponge for Health Monitoring," *Small,* vol. 13, no. 39, p. 1702091, 2017.

[163]   S. Jung, J. Lee, T. Hyeon, M. Lee, and D.-H. Kim, "Fabric-Based Integrated Energy Devices for Wearable Activity Monitors," *Advanced Materials,* vol. 26, no. 36, pp. 6329-6334, 2014.

[164]   Y. Liang *et al.*, "Self-powered wearable graphene fiber for information expression," *Nano Energy,* vol. 32, pp. 329-335, 2017/02/01/ 2017.

[165]   J. Liang, K. Tong, and Q. Pei, "A Water-Based Silver-Nanowire Screen-Print Ink for the Fabrication of Stretchable Conductors and Wearable Thin-Film Transistors," *Advanced Materials,* vol. 28, no. 28, pp. 5986-5996, 2016.

[166]   Y. Huang *et al.*, "Nanostructured Polypyrrole as a flexible electrode material of supercapacitor," *Nano Energy,* vol. 22, pp. 422-438, 2016/04/01/ 2016.

[167]   H. Zou *et al.*, "Quantifying the triboelectric series," *Nature Communications,* vol. 10, no. 1, p. 1427, Mar 29 2019.

[168]   S. Wang *et al.*, "Maximum surface charge density for triboelectric nanogenerators achieved by ionized-air injection: methodology and theoretical understanding," *Adv Mater,* vol. 26, no. 39, pp. 6720-8, Oct 22 2014.

[169]   G.-G. Cheng *et al.*, "Effect of argon plasma treatment on the output performance of triboelectric nanogenerator," *Applied Surface Science,* vol. 412, pp. 350-356, 2017/08/01/ 2017.

[170]   B. Zhang *et al.*, "Self-Powered Acceleration Sensor Based on Liquid Metal Triboelectric Nanogenerator for Vibration Monitoring," *ACS Nano,* vol. 11, no. 7, pp. 7440-7446, Jul 25 2017.

[171]   Y. Yang *et al.*, "Liquid-Metal-Based Super-Stretchable and Structure-Designable Triboelectric Nanogenerator for Wearable Electronics," *ACS Nano,* vol. 12, no. 2, pp. 2027-2034, Feb 27 2018.

[172] L. E. Helseth and X. D. Guo, "Hydrophobic polymer covered by a grating electrode for converting the mechanical energy of water droplets into electrical energy," *Smart Materials and Structures,* vol. 25, no. 4, 2016.

[173] X. Liang *et al.*, "Triboelectric nanogenerator networks integrated with power management module for water wave energy harvesting," *Advanced Functional Materials,* vol. 29, no. 41, 2019.

[174] A. Wei *et al.*, "Triboelectric Nanogenerator Driven Self-Powered Photoelectrochemical Water Splitting Based on Hematite Photoanodes," *ACS Nano,* vol. 12, no. 8, pp. 8625-8632, Aug 28 2018.

[175] Z. Li *et al.*, "Triboelectrification-Enabled Self-Powered Detection and Removal of Heavy Metal Ions in Wastewater," *Adv Mater,* vol. 28, no. 15, pp. 2983-91, Apr 20 2016.

[176] S. Lee, J. Chung, D. Y. Kim, J. Y. Jung, S. H. Lee, and S. Lee, "Cylindrical water triboelectric nanogenerator via controlling geometrical shape of anodized aluminum for enhanced electrostatic induction," *ACS Appl Mater Interfaces,* vol. 8, no. 38, pp. 25014-8, Sep 28 2016.

[177] Y. Xu *et al.*, "A One-Dimensional Fluidic Nanogenerator with a High Power Conversion Efficiency," *Angew Chem Int Ed Engl,* vol. 56, no. 42, pp. 12940-12945, Oct 9 2017.

[178] Q. Liang, X. Yan, X. Liao, and Y. Zhang, "Integrated multi-unit transparent triboelectric nanogenerator harvesting rain power for driving electronics," *Nano Energy,* vol. 25, pp. 18-25, 2016.

[179] S.-B. Jeon, D. Kim, G.-W. Yoon, J.-B. Yoon, and Y.-K. Choi, "Self-cleaning hybrid energy harvester to generate power from raindrop and sunlight," *Nano Energy,* vol. 12, pp. 636-645, 2015.

[180] L. Zheng *et al.*, "Silicon-based hybrid cell for harvesting solar energy and raindrop electrostatic energy," *Nano Energy,* vol. 9, pp. 291-300, 2014.

[181] R. K. Cheedarala, M. Shahriar, J. H. Ahn, J. Y. Hwang, and K. K. Ahn, "Harvesting liquid stream energy from unsteady peristaltic flow induced pulsatile Flow-TENG (PF-TENG) using slipping polymeric surface inside elastomeric tubing," *Nano Energy,* vol. 65, 2019.

[182] Z.-H. L. Gang Cheng, Zu-liang Du, and Zhong Lin Wang, "Simultaneously Harvesting Electrostatic and Mechanical Energies from Flowing Water by a Hybridized Triboelectric Nanogenerator," *ACS Nano,* vol. 8, no. 2, pp. 1932-1939, 2014.

[183] L. E. Helseth, "A water droplet-powered sensor based on charge transfer to a flow-through front surface electrode," *Nano Energy,* vol. 73, 2020.

[184] J. Nie *et al.*, "Probing Contact-Electrification-Induced Electron and Ion Transfers at a Liquid-Solid Interface," *Adv Mater,* vol. 32, no. 2, p. e1905696, Jan 2020.

[185] X. Li *et al.*, "Performance and power management of droplets-based electricity generators," *Nano Energy,* vol. 92, 2022.

[186] K. R. Wijewardhana, T.-Z. Shen, E. N. Jayaweera, A. Shahzad, and J.-K. Song, "Hybrid nanogenerator and enhancement of water–solid contact electrification using triboelectric charge supplier," *Nano Energy,* vol. 52, pp. 402-407, 2018.

[187] J. Dong *et al.*, "A high voltage direct current droplet-based electricity generator inspired by thunderbolts," *Nano Energy,* vol. 90, 2021.

[188] W. Xu *et al.*, "A droplet-based electricity generator with high instantaneous power density," *Nature,* vol. 578, no. 7795, pp. 392-396, Feb 2020.

[189] Y. Yan *et al.*, "Direct Current Electricity Generation from Dynamic Polarized Water–Semiconductor Interface," *The Journal of Physical Chemistry C,* vol. 125, no. 26, pp. 14180-14187, 2021.

[190] D. L. Vu, C. D. Le, and K. K. Ahn, "Functionalized graphene oxide/polyvinylidene fluoride composite membrane acting as a triboelectric layer for hydropower energy harvesting," *International Journal of Energy Research,* pp. 9549- 9559, 2022.

[191] D. L. Vu and K. K. Ahn, "High-Performance Liquid-Solid Triboelectric Nanogenerator Based on Polyvinylidene Fluoride and Magnetic Nanoparticle Composites Film," presented at the 2021 24th International Conference on Mechatronics Technology (ICMT), 2021.

[192] D. L. Vu, C. D. Le, C. P. Vo, and K. K. Ahn, "Surface polarity tuning through epitaxial growth on polyvinylidene fluoride membranes for enhanced performance of liquid-solid triboelectric nanogenerator," *Composites Part B: Engineering,* vol. 223, p. 109135, 2021.

[193] S. S. Kwak *et al.*, "Triboelectrification-Induced Large Electric Power Generation from a Single Moving Droplet on Graphene/Polytetrafluoroethylene," *ACS Nano,* vol. 10, no. 8, pp. 7297-302, Aug 23 2016.

[194] S. X. Yang Dong, Chi Zhang, Liqiang Zhang, Daoai Wang,, N. L. Yuanyuan Xie, Yange Feng, Nannan Wang, Min Feng, Xiaolong Zhang,, and Z. L. W. Feng Zhou, "Gas-liquid two-phase flow-based triboelectric nanogenerator with ultrahigh output power," *Science advances,* vol. 8, 2022.

[195] H. Phan *et al.*, "Aerodynamic and aeroelastic flutters driven triboelectric nanogenerators for harvesting broadband airflow energy," *Nano Energy,* vol. 33, pp. 476-484, 2017.

[196] S. W. Yannan Xie, Long Lin, Qingshen Jing, Zong-Hong Lin, Simiao Niu, Zhengyun Wu, and Zhong Lin Wang, "Rotary Triboelectric Nanogenerator Based on a Hybridized Mechanism for Harvesting Wind Energy," *ACS Nano,* vol. 7, no. 8, pp. 7119-7125, 2013.

[197] X. Ren *et al.*, "Wind energy harvester based on coaxial rotatory freestanding triboelectric nanogenerators for self-powered water splitting," *Nano Energy,* vol. 50, pp. 562-570, 2018.

[198] J. Y. Jun Chen, Zhaoling Li, Xing Fan, Yunlong Zi, Qingshen Jing, Hengyu Guo, Zhen Wen, and S. N. Ken C. Pradel, and Zhong Lin Wang, "Networks of Triboelectric Nanogenerators for Harvesting Water Wave Energy: A Potential Approach toward Blue Energy," *ACS Nano,* vol. 9, no. 3, pp. 3324-3331, 2015.

[199] A. Ahmed *et al.*, "Integrated Triboelectric Nanogenerators in the Era of the Internet of Things," *Adv Sci (Weinh),* vol. 6, no. 24, p. 1802230, Dec 2019.

[200] X. Li *et al.*, "Self-Powered Triboelectric Nanosensor for Microfluidics and Cavity-Confined Solution Chemistry," *ACS Nano,* vol. 9, no. 11, pp. 11056-63, Nov 24 2015.

[201] H. Zhang *et al.*, "Triboelectric nanogenerator as self-powered active sensors for detecting liquid/gaseous water/ethanol," *Nano Energy,* vol. 2, no. 5, pp. 693-701, 2013.

[202] D. Choi, Y.-H. Tsao, C.-M. Chiu, D. Yoo, Z.-H. Lin, and D. S. Kim, "A smart pipet tip: Triboelectricity and thermoelectricity assisted in situ evaluation of electrolyte concentration," *Nano Energy,* vol. 38, pp. 419-427, 2017.

[203] G. Cai, Y. Liang, Z. Liu, and W. Liu, "Design and optimization of bio-inspired wave-like channel for a PEM fuel cell applying genetic algorithm," *Energy,* vol. 192, 2020.

[204] A. Muetze and J. G. Vining, "Ocean Wave Energy Conversion - A Survey," in *Conference Record of the 2006 IEEE Industry Applications Conference Forty-First IAS Annual Meeting*, 2006, vol. 3, pp. 1410-1417.

[205] R. Sabzehgar and M. Moallem, "A review of ocean wave energy conversion systems," in *2009 IEEE Electrical Power & Energy Conference (EPEC)*, 2009, pp. 1-6.

[206] C. Chang, V. H. Tran, J. Wang, Y.-K. Fuh, and L. Lin, "Direct-write piezoelectric polymeric nanogenerator with high energy conversion efficiency," *Nano Letters,* vol. 10, no. 2, pp. 726-731, 2010/02/10 2010.

[207] C. Zhang, W. Tang, C. Han, F. Fan, and Z. L. Wang, "Theoretical comparison, equivalent transformation, and conjunction operations of electromagnetic induction generator and triboelectric nanogenerator for harvesting mechanical energy," *Advanced Materials,* vol. 26, no. 22, pp. 3580-3591, 2014.

[208] X. Wang, J. Song, J. Liu, and Z. L. Wang, "Direct-current nanogenerator driven by ultrasonic waves," *Science,* vol. 316, no. 5821, pp. 102-105, 2007.

[209] D. Jiang *et al.*, "Water-solid triboelectric nanogenerators: An alternative means for harvesting hydropower," *Renewable and Sustainable Energy Reviews,* vol. 115, 2019.

[210] M. Wang *et al.*, "Single-electrode triboelectric nanogenerators based on sponge-like porous PTFE thin films for mechanical energy harvesting and self-powered electronics," *Journal of Materials Chemistry A,* vol. 5, no. 24, pp. 12252-12257, 2017.

[211] P. Bai *et al.*, "Integrated multilayered triboelectric nanogenerator for harvesting biomechanical energy from human motions," *ACS Nano,* vol. 7, no. 4, pp. 3713-3719, 2013/04/23 2013.

[212] Z. L. Wang, J. Chen, and L. Lin, "Progress in triboelectric nanogenerators as a new energy technology and self-powered sensors," *Energy & Environmental Science,* vol. 8, no. 8, pp. 2250-2282, 2015.

[213] G. Zhu *et al.*, "Toward large-scale energy harvesting by a nanoparticle-enhanced triboelectric nanogenerator," *Nano Lett,* vol. 13, no. 2, pp. 847-53, Feb 13 2013.

[214] V. Nguyen and R. Yang, "Effect of humidity and pressure on the triboelectric nanogenerator," *Nano Energy,* vol. 2, no. 5, pp. 604-608, 2013.

[215] M. Karimi, S. Seddighi, and R. Mohammadpour, "Nanostructured versus flat compact electrode for triboelectric nanogenerators at high humidity," *Sci Rep,* vol. 11, no. 1, p. 16191, Aug 10 2021.

[216] J. Shen, Z. Li, J. Yu, and B. Ding, "Humidity-resisting triboelectric nanogenerator for high performance biomechanical energy harvesting," *Nano Energy,* vol. 40, pp. 282-288, 2017.

[217] S. Kamel and A. K. T, "Recent Advances in Cellulose-Based Biosensors for Medical Diagnosis," *Biosensors (Basel),* vol. 10, no. 6, Jun 17 2020.

[218] J. Zhou *et al.*, "Cellulose for Sustainable Triboelectric Nanogenerators," *Advanced Energy and Sustainability Research,* 2021.

[219] Y. Song, Z. Shi, G.-H. Hu, C. Xiong, A. Isogai, and Q. Yang, "Recent advances in cellulose-based piezoelectric and triboelectric nanogenerators for energy harvesting: a review," *Journal of Materials Chemistry A,* vol. 9, no. 4, pp. 1910-1937, 2021.

[220] J. Luo *et al.*, "Flexible and durable wood-based triboelectric nanogenerators for self-powered sensing in athletic big data analytics," *Nat Commun,* vol. 10, no. 1, p. 5147, Nov 26 2019.

[221] S. Parandeh, M. Kharaziha, and F. Karimzadeh, "An eco-friendly triboelectric hybrid nanogenerators based on graphene oxide incorporated polycaprolactone fibers and cellulose paper," *Nano Energy,* vol. 59, pp. 412-421, 2019.

[222] K. Shi, M. Ren, and I. Zhitomirsky, "Activated Carbon-Coated Carbon Nanotubes for Energy Storage in Supercapacitors and Capacitive Water Purification," *ACS Sustainable Chemistry & Engineering,* vol. 2, no. 5, pp. 1289-1298, 2014.

[223] S. Chen, J. Jiang, F. Xu, and S. Gong, "Crepe cellulose paper and nitrocellulose membrane-based triboelectric nanogenerators for energy harvesting and self-powered human-machine interaction," *Nano Energy,* vol. 61, pp. 69-77, 2019.

[224] Z. Bai *et al.*, "Highly flexible, porous electroactive biocomposite as attractive tribopositive material for advancing high-performance triboelectric nanogenerator," *Nano Energy,* vol. 75, 2020.

[225] M. A. Hubbe, A. Ayoub, J. S. Daystar, R. A. Venditti, and J. J. Pawlak, "Enhanced Absorbent Products Incorporating Cellulose and Its Derivatives: A Review," *BioResources,* vol. 8, no. 4, 2013.

[226] H. Peng *et al.*, "Preparation of Superhydrophobic Magnetic Cellulose Sponge for Removing Oil from Water," *Industrial & Engineering Chemistry Research,* vol. 55, no. 3, pp. 832-838, 2016.

[227] D. Reishofer *et al.*, "Humidity Response of Cellulose Thin Films," *Biomacromolecules,* vol. 23, no. 3, pp. 1148-1157, Mar 14 2022.

[228] A. Chami Khazraji and S. Robert, "Interaction Effects between Cellulose and Water in Nanocrystalline and Amorphous Regions: A Novel Approach Using Molecular Modeling," *Journal of Nanomaterials,* vol. 2013, pp. 1-10, 2013.

[229] N. Wang *et al.*, "New Hydrogen Bonding Enhanced Polyvinyl Alcohol Based Self-Charged Medical Mask with Superior Charge Retention and Moisture Resistance Performances," *Advanced Functional Materials,* vol. 31, no. 14, 2021.

[230] L. Kelvin, "V. Contact electricity of metals," *The London, Edinburgh, and Dublin Philosophical Magazine and Journal of Science,* vol. 46, no. 278, pp. 82-120, 1898/07/01 1898.

[231] T. Kenzhekhanov, D. Abduvali, G. Kalimuldina, and D. Adair, "Investigating the feasibility of energy harvesting using material work functions," *Materials Today: Proceedings,* vol. 49, pp. 2501-2505, 2022.

[232] A. Varpula, S. J. Laakso, T. Havia, J. Kyynarainen, and M. Prunnila, "Harvesting vibrational energy using material work functions," *Sci Rep,* vol. 4, p. 6799, Oct 28 2014.

[233] S. H. Atefe Derakhshani, Nader Nezafati, Mahmoud Azami, "Comparative analysis of gelatin and hydroxyethyl cellulose scaffolds crosslinked by silane coupling agent," *Journal of Tissue and Materials,* vol. 3, no. 3, pp. 1-10, 2020.

[234] C. Demitri *et al.*, "Preparation and characterization of cellulose-based foams via microwave curing," *Interface Focus,* vol. 4, no. 1, p. 20130053, Feb 6 2014.

[235] Y. Zhou, W. Deng, J. Xu, and J. Chen, "Engineering Materials at the Nanoscale for Triboelectric Nanogenerators," *Cell Reports Physical Science,* vol. 1, no. 8, 2020.

[236] S. Mandal *et al.*, "Protein-Based Flexible Moisture-Induced Energy-Harvesting Devices As Self-Biased Electronic Sensors," *ACS Applied Electronic Materials,* vol. 2, no. 3, pp. 780-789, 2020.

[237] S. Y. Oh *et al.*, "Crystalline structure analysis of cellulose treated with sodium hydroxide and carbon dioxide by means of X-ray diffraction and FTIR spectroscopy," *Carbohydr Res,* vol. 340, no. 15, pp. 2376-91, Oct 31 2005.

[238] W. Chen, H. He, H. Zhu, M. Cheng, Y. Li, and S. Wang, "Thermo-Responsive Cellulose-Based Material with Switchable Wettability for Controllable Oil/Water Separation," *Polymers (Basel),* vol. 10, no. 6, May 28 2018.

[239] S. Zhang *et al.*, "Hydrophobic Cellulose Acetate Aerogels for Thermal Insulation," *Gels,* vol. 8, no. 10, Oct 19 2022.

[240] A. M. Raspolli Galletti *et al.*, "Midinfrared FT-IR as a Tool for Monitoring Herbaceous Biomass Composition and Its Conversion to Furfural," *Journal of Spectroscopy,* vol. 2015, pp. 1-12, 2015.

[241] S. Y. Oh, D. I. Yoo, Y. Shin, and G. Seo, "FTIR analysis of cellulose treated with sodium hydroxide and carbon dioxide," *Carbohydr Res,* vol. 340, no. 3, pp. 417-28, Feb 28 2005.

[242] S. Mugesh, T. P. Kumar, and M. Murugan, "An unprecedented bacterial cellulosic material for defluoridation of water," *RSC Advances,* vol. 6, no. 106, pp. 104839-104846, 2016.

[243] A. D. French, "Idealized powder diffraction patterns for cellulose polymorphs," *Cellulose,* vol. 21, no. 2, pp. 885-896, 2013.

[244] J. Gong, J. Li, J. Xu, Z. Xiang, and L. Mo, "Research on cellulose nanocrystals produced from cellulose sources with various polymorphs," *RSC Advances,* vol. 7, no. 53, pp. 33486-33493, 2017.

[245] T. Kawano, S. Iikubo, and Y. Andou, "The Relationship between Crystal Structure and Mechanical Performance for Fabrication of Regenerated Cellulose Film through Coagulation Conditions," *Polymers (Basel),* vol. 13, no. 24, Dec 18 2021.

[246] C. Solares-Bockmon *et al.*, "Generalized dynamic junction theory to resolve the mechanism of direct current generation in liquid-solid interfaces," *Nano Energy,* vol. 99, 2022.

[247] Y.-S. Lee, S. Jeon, D. Kim, D.-M. Lee, D. Kim, and S.-W. Kim, "High performance direct current-generating triboelectric nanogenerators based on tribovoltaic p-n junction with ChCl-passivated CsFAMA perovskite," *Nano Energy,* vol. 106, 2023.

[248] Y. Zhang, Y. Liu, and Z. L. Wang, "Fundamental theory of piezotronics," *Adv Mater,* vol. 23, no. 27, pp. 3004-13, Jul 19 2011.

[249] Y. Park, V. Choong, Y. Gao, B. R. Hsieh, and C. W. Tang, "Work function of indium tin oxide transparent conductor measured by photoelectron spectroscopy," *Applied Physics Letters,* vol. 68, no. 19, pp. 2699-2701, 1996.

[250] A. Capasso, L. Salamandra, A. Di Carlo, J. M. Bell, and N. Motta, "Low-temperature synthesis of carbon nanotubes on indium tin oxide electrodes for organic solar cells," *Beilstein J Nanotechnol,* vol. 3, pp. 524-32, 2012.

[251] M. Pusty and P. M. Shirage, "Gold nanoparticle-cellulose/PDMS nanocomposite: a flexible dielectric material for harvesting mechanical energy," *RSC Adv,* vol. 10, no. 17, pp. 10097-10112, Mar 6 2020.

[252] P. Sahatiya, S. Kannan, and S. Badhulika, "Few layer MoS2 and in situ poled PVDF nanofibers on low cost paper substrate as high performance piezo-triboelectric hybrid nanogenerator: Energy harvesting from handwriting and human touch," *Applied Materials Today,* vol. 13, pp. 91-99, 2018.

[253] B. Toroń, P. Szperlich, M. Nowak, D. Stróż, and T. Rzychoń, "Novel piezoelectric paper based on SbSI nanowires," *Cellulose,* vol. 25, no. 1, pp. 7-15, 2017.

[254] Q. Zheng, H. Zhang, H. Mi, Z. Cai, Z. Ma, and S. Gong, "High-performance flexible piezoelectric nanogenerators consisting of porous cellulose nanofibril (CNF)/poly(dimethylsiloxane) (PDMS) aerogel films," *Nano Energy,* vol. 26, pp. 504-512, 2016.

[255] M. M. Alam and D. Mandal, "Native Cellulose Microfiber-Based Hybrid Piezoelectric Generator for Mechanical Energy Harvesting Utility," *ACS Appl Mater Interfaces,* vol. 8, no. 3, pp. 1555-8, Jan 27 2016.

[256] G. C. Yoon *et al.*, "High-performance hybrid cell based on an organic photovoltaic device and a direct current piezoelectric nanogenerator," *Nano Energy,* vol. 12, pp. 547-555, 2015.

[257] Y. Yang, H. Zhang, and Z. L. Wang, "Direct-Current Triboelectric Generator," *Advanced Functional Materials,* vol. 24, no. 24, pp. 3745-3750, 2014.

[258] K. H. Kim *et al.*, "Piezoelectric two-dimensional nanosheets/anionic layer heterojunction for efficient direct current power generation," *Sci Rep,* vol. 3, p. 2017, 2013.

[259] K. L. Brijesh Kumar, Hyun-Kyu Park, Seung Jin Chae, YoungHee Lee, Sang-WooKim, "Controlled growth of semiconducting nanowire, nanowall, and hybrid nanostructures on graphene for piezoelectric nanogenerators," *Acs Nano,* vol. 5, no. 5, pp. 4197-4204, 2011.

[260] J. S. Xudong Wang, Jin Liu, Zhong Lin Wang, " Direct-current nanogenerator driven by ultrasonic waves," *Science,* no. 316, pp. 102-105, 2007.

[261] D. W. Kim, J. H. Lee, J. K. Kim, and U. Jeong, "Material aspects of triboelectric energy generation and sensors," *NPG Asia Materials,* vol. 12, no. 1, 2020.

[262] T. Zhang, Z. Wen, Y. Liu, Z. Zhang, Y. Xie, and X. Sun, "Hybridized Nanogenerators for Multifunctional Self-Powered Sensing: Principles, Prototypes, and Perspectives," *iScience,* vol. 23, no. 12, p. 101813, Dec 18 2020.

[263] D. Jiang *et al.*, "Advances in triboelectric nanogenerator technology—applications in self-powered sensors, Internet of things, biomedicine, and blue energy," *Advanced Composites and Hybrid Materials,* vol. 6, no. 2, 2023.

[264] H. Shao, J. Fang, H. Wang, L. Dai, and T. Lin, "Polymer-Metal Schottky Contact with Direct-Current Outputs," *Adv Mater,* vol. 28, no. 7, pp. 1461-6, Feb 17 2016.

[265] H. Yang *et al.*, "A full-packaged rolling triboelectric-electromagnetic hybrid nanogenerator for energy harvesting and building up self-powered wireless systems," *Nano Energy,* vol. 56, pp. 300-306, 2019.

[266] Z. Lin *et al.*, "Triboelectric Nanogenerator Enabled Body Sensor Network for Self-Powered Human Heart-Rate Monitoring," *ACS Nano,* vol. 11, no. 9, pp. 8830-8837, Sep 26 2017.

[267] D. Kim, S.-J. Park, S.-B. Jeon, M.-L. Seol, and Y.-K. Choi, "A Triboelectric Sponge Fabricated from a Cube Sugar Template by 3D Soft Lithography for Superhydrophobicity and Elasticity," *Advanced Electronic Materials,* vol. 2, no. 4, 2016.

[268] F. R. Fan, L. Lin, G. Zhu, W. Wu, R. Zhang, and Z. L. Wang, "Transparent triboelectric nanogenerators and self-powered pressure sensors based on micropatterned plastic films," *Nano Lett,* vol. 12, no. 6, pp. 3109-14, Jun 13 2012.

[269] K. Xia, Z. Zhu, H. Zhang, and Z. Xu, "A triboelectric nanogenerator as self-powered temperature sensor based on PVDF and PTFE," *Applied Physics A,* vol. 124, no. 8, 2018.

[270] S.-B. Jeon, M.-L. Seol, D. Kim, S.-J. Park, and Y.-K. Choi, "Self-Powered Ion Concentration Sensor with Triboelectricity from Liquid-Solid Contact Electrification," *Advanced Electronic Materials,* vol. 2, no. 5, 2016.

[271] C. Chen *et al.*, "Self-powered on-line ion concentration monitor in water transportation driven by triboelectric nanogenerator," *Nano Energy,* vol. 62, pp. 442-448, 2019.

[272] D. Wang, D. Zhang, Y. Yang, Q. Mi, J. Zhang, and L. Yu, "Multifunctional Latex/Polytetrafluoroethylene-Based Triboelectric Nanogenerator for Self-Powered Organ-like MXene/Metal-Organic Framework-Derived CuO Nanohybrid Ammonia Sensor," *ACS Nano,* vol. 15, no. 2, pp. 2911-2919, Feb 23 2021.

[273] H.-T. Deng *et al.*, "Super-stretchable multi-sensing triboelectric nanogenerator based on liquid conductive composite," *Nano Energy,* vol. 83, 2021.

[274] Z. Wu, B. Zhang, H. Zou, Z. Lin, G. Liu, and Z. L. Wang, "Multifunctional Sensor Based on Translational-Rotary Triboelectric Nanogenerator," *Advanced Energy Materials,* vol. 9, no. 33, 2019.

[275] J. Zhou *et al.*, "Cellulose for Sustainable Triboelectric Nanogenerators," *Advanced Energy and Sustainability Research,* vol. 3, no. 5, 2021.

[276] I. H. Sahputra, A. Alexiadis, and M. J. Adams, "Effects of Moisture on the Mechanical Properties of Microcrystalline Cellulose and the Mobility of the Water Molecules as Studied by the Hybrid Molecular Mechanics-Molecular Dynamics Simulation Method," *Journal of Polymer Science Part B: Polymer Physics,* vol. 57, no. 8, pp. 454-464, 2019.

[277] G. Banik and I. Brückle, "Principles of Water Absorption and Desorption in Cellulosic Materials," *Restaurator,* vol. 31, no. 3-4, 2010.

[278] S. Gao, L. H. Yang, Y. Gan, and Q. Chen, "The Influence of Sliding Speed on the Friction Behavior of Silica Surface," *ACS Omega,* vol. 6, no. 4, pp. 3384-3389, Feb 2 2021.

[279] Z. Zhao, D. Liu, Y. Li, Z. L. Wang, and J. Wang, "Direct-current triboelectric nanogenerator based on electrostatic breakdown effect," *Nano Energy,* vol. 102, 2022.

[280] J. Kaur and R. Kant, "Theory of Work Function and Potential of Zero Charge for Metal Nanostructured and Rough Electrodes," *The Journal of Physical Chemistry C,* vol. 121, no. 24, pp. 13059-13069, 2017.

[281] M. Stössel, J. Staudigel, F. Steuber, J. Simmerer, and A. Winnacker, "Impact of the cathode metal work function on the performance of vacuum-deposited organic light emitting-devices," *Applied Physics A: Materials Science & Processing,* vol. 68, no. 4, pp. 387-390, 1999.

[282] R. Rajput and R. Vaid, "Flash memory devices with metal floating gate/metal nanocrystals as the charge storage layer: A status review," *Facta universitatis - series: Electronics and Energetics,* vol. 33, no. 2, pp. 155-167, 2020.

[283]   J. Chung, H. Cho, H. Yong, D. Heo, Y. S. Rim, and S. Lee, "Versatile surface for solid-solid/liquid-solid triboelectric nanogenerator based on fluorocarbon liquid infused surfaces," *Sci Technol Adv Mater,* vol. 21, no. 1, pp. 139-146, 2020.